Alma Mater Studiorum - Università di Bologna

Facoltà di Scienze Matematiche Fisiche e Naturali
Dottorato di Ricerca in Fisica, XX Ciclo

PhD Thesis

Astroparticle Physics with Nuclear Track Detectors

Dott. Eduardo Medinaceli V.

Advisors:
Prof. Giorgio Giacomelli
Dott. Stefano Cecchini
Dott.ssa. Laura Patrizii
Dott. Tommaso Chiarusi

PhD Coordinator:
Prof. Fabio Ortolani

FIS/01

Bologna, Italy, March 2008

Contents

Introduction

This thesis is mainly about

1. the search for Intermediate Mass Magnetic Monopoles with the SLIM experiment at the Chacaltaya High Altitude Laboratory (5230 m , Bolivia) and

2. the measurement of the elemental abundance of the primary cosmic rays with the CAKE experiment on board of a stratospheric balloon.

Both experiments were based on the use of plastic Nuclear Track Detectors (NTDs), mainly the CR39. NTDs can record the passage of ionizing particles; by using some chemical reagents such passage can be make visible at optical microscopes.

In the first chapter I briefly discuss our present knowledge of the primary cosmic ray charge spectrum and its implications on the understanding on their origin, acceleration and propagation to the Earth.

In the second chapter I examine the characteristics of the different massive particles of possible cosmological origin, proposed as dark matter candidates, and which can be searched for in the cosmic radiation impinging on the Earth.

I will then briefly present the principle of Solid State Nuclear Track detection describing the mechanism of track formation and geometry and the system for the data collection.

Chapters 4 and 5 are dedicated to the analysis of the data of the SLIM experiment and to the work I have done for the study of the background induced by the neutron flux at the experimental site through Monte Carlo simulations. The code I have developed is described in detail and compared to one of the few existing for such purpose.

Finally I present the results obtained by the CAKE experiment and in particular the computations tools I have implemented for increasing the efficiency of the automatic track recognition and measurements

Chapter 1

Cosmic Rays

1.1 Introduction

Cosmic rays (CRs) arriving on Earth can give information about different types of processes that happen in the Universe. By studying their composition and energy spectrum, information about their origin and propagation can be obtained. Cosmic radiation was discovered by V. Hess in 1912 studying the ionisation rate of gases contained in closed vessels; with a balloon experiment he observed that the ionisation rate was several times the one measured at the sea level, and in 1927 this ionisation was attributed to the presence of a penetrating radiation of extraterrestrial origin. In the same year it was also discovered the terrestrial geomagnetic effect, as a consequence of the fact that the ionisation produced by CRs depends on the latitude, and it was so established that CRs are electrically charged.

Primary CRs are 92% protons, 6% helium nuclei and 1% heavy nuclei. Electrons are present at the level of 1%, gamma rays at the level of 0.1%, other types of particles are present in small percentages, *e.g.* positrons and anti-protons at the level of 10^{-4} [1]. The "all particle" energy spectrum of CRs (figure 1.1), shows that the flux of particles decrease rapidly with increasing energy; the spectrum covers many orders of magnitude. At low energies ($\leq 1 GeV$) the spectrum is composed of CRs of solar origin, associated to violent processes in the Sun.

The total energy density of CRs with $E > 1\ GeV$ is roughly 1 MeV/m^3 dominated by the low energies. Primary CRs interact in the atmosphere at $\sim$ 20 km of altitude, generating secondaries cosmic rays *e.g.* e^+ and $\mu^\pm$ (both discovered in 1937 by Anderson), mesons π, $\pi^\pm$ (discovered in 1947 by Powell).

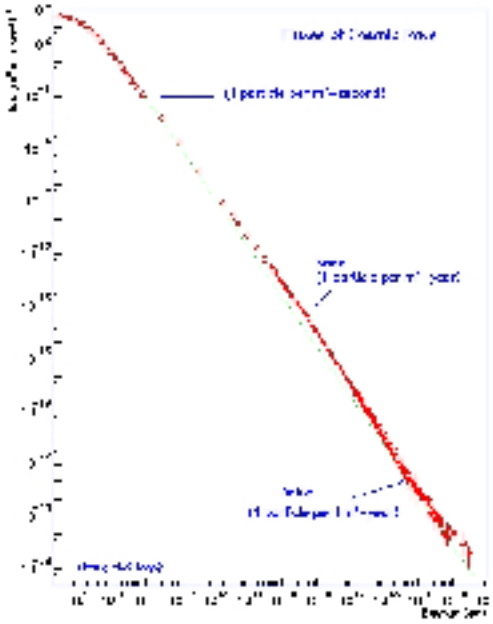

Figure 1.1: "All particle" energy spectrum of cosmic rays. The energy range covers more than 10 orders of magnitude, and the flux decreases rapidly (some fluxe value are indicated).

1.2 Energy Spectrum of CRs

Several features have been identified or proposed for this spectrum. The first of these features is a softening of the spectrum at an energy of about 3×10^{15} eV where the flux bends *down* (the *knee*). When later on, another downturn at higher energy (4×10^{17} eV) was observed, it was naturally called the *second knee*. This point is the lower end of the energy range of the so called Ultra High Energy Cosmic Rays (UHECR). About one order of magnitude higher at $\sim 10^{18}$ eV, the spectrum becomes less steep for at least two decades of energy. This is called the *ankle*, because the bending is in the opposite sense than the one seen at the knee. Finally at about 6×10^{19} eV a cutoff (Greisen 1966, Zatsepin & Kuz'min 1966) is expected, due to energy losses of CR by photopion production of protons on the cosmic microwave background radiation [4].

The spectrum is described by a power law $\Phi(E) = kE^{\gamma}$, whith a spectral index $\gamma = -2.7$ up to the knee ($\sim 3 \times 10^{15}$ eV), then up to the ankle ($\sim 10^{18}$ eV) $\gamma = -3.0$. At higher energies $\gamma = -2.7$.

Figure 1.2 shows the differential "all particle" CR spectrum multiplied by $E^{2.7}$. In the figure are also shown the energies of different accelerators; LHC will reach an energy $\sim 10^{17}$ eV.

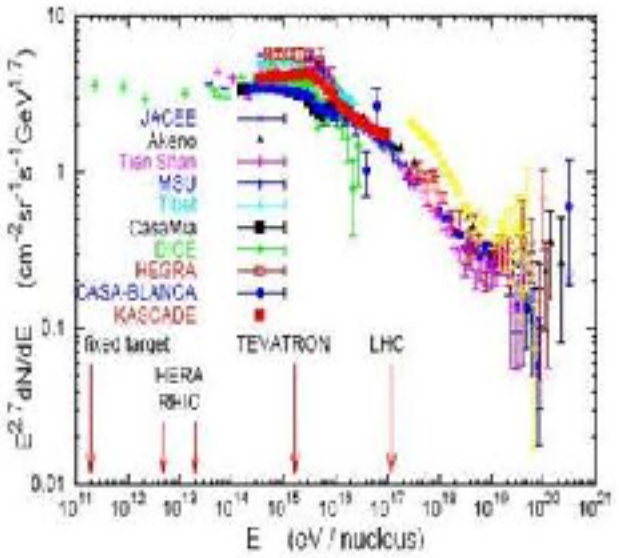

Figure 1.2: Summary of experimental measurements of the high energy cosmic ray spectrum [6].

The energy spectra for individual elements are obtained directly with satellite and balloon-born experiments at the top of the atmosphere up to energies of several 10^{13} eV, as the balloon experiment JACEEE (in figure 1.2). At higher energies large detection areas and long exposure times are required; the measurements at these energies come from ground based experiments, as KASCADE [8] (figure 1.2). At ultra high energy $\sim 10^{18}$ eV and larger, experiments detect extensive air showers (EAS) generated by interactions of UHECR with nuclei in the atmosphere. Recent results from AGASA, Fly's Eye, HiRes (I & II) and Auger seem to confirm the existence of the GZK cutoff at $\sim 10^{20}$ eV [4].

1.3 Composition of Cosmic Ray nuclei

The relative abundances of cosmic rays are compared with abundances of elements in the solar system in figure 1.3. The symbols in the figure have the following meanings: solid circles represent the cosmic ray abundances, while the white boxes represent the Solar system abundances relative to Silicon ($Z = 14$). Both solar system and cosmic ray abundances show the "odd-even" effect, even Z nuclei being more abundant. There are, however, to apparent differences between the two compositions.

First, nuclei whith $Z > 1$ are much more abundant relative to protons in cosmic rays that they are in solar system materials. This is not clearly understood. It may be that hydrogen is relatively hard to ionize in the injection and acceleration

process, or it could reflect a genuine difference in composition at the source.

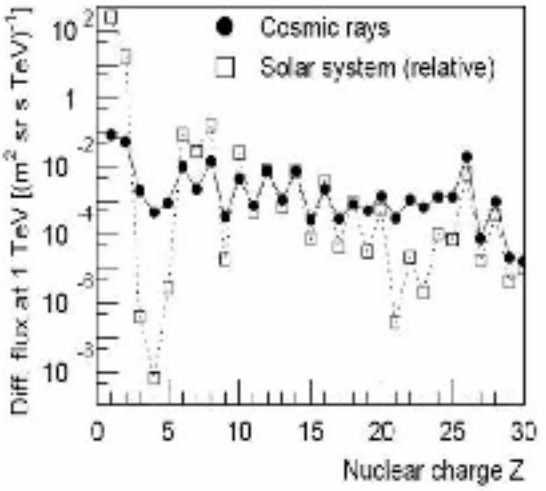

Figure 1.3: The Cosmic Ray elemental abundances measured at Earth (represented with back dots), compared to the Solar system abundances (represented withwhite boxes), all relative to Silicon.

The second difference is better understood and it is an inportant tool for understanding propagation and confinement of cosmic rays in the Galaxy. The two groups of elements Li, Be, B and Sc, Ti, V, Cr are many orders of magnitude more abundant in the cosmic radiation than in solar system materials. These elements are essentially absent as end products of stellar nucleosynthesis. They are nevertheless present in the cosmic radiation as aspallation products of the abundant nuclei of carbon and oxygen (Li, Be, B) and of iron (Sc, Ti, V, Cr, Mn). They are produced by collisions of cosmic rays in the interstellar medium (ISM). From a knowledge of the cross sections for spallation, one can indirectly infer the amount of matter traversed by cosmic rays between production and observation. For the bulk of the cosmic rays the mean amount of matter traversed is of order $X = 5 \div 10$ g/cm^2. The density ρ_N in the disk of the galaxy is of order one proton per cm^3, so this thickness of material correspond to a distance of $l = X/(m_p \rho_N) = 3 \times 10^{24}$ cm $\sim$1000 kpc. (Since the Cosmic Rays may spend some time in the diffuse galactic halo, this is a lower limit to the distance travelled). In any case, $l >> d \sim 0.1$ kpc, where d is the half-thickness of the disk of the galaxy. This implies that cosmic ray confinement is a diffusive process in which the particle rattle around for a long time before escaping into intergalactic space [5].

1.3.1 Stellar Nucleosynthesis

The brightest stars are the most interesting for nucleosynthesis. In evolutionary models for some star evolution, a convective core is present in their central regions. The mass of the core is dominated by the products of the nuclear reactions. The most efficient nuclear process for Sun-like stars is the hydrogen burning p-p cycle, where Helium is produced according to the following chain

$$p + p \rightarrow d + e^{+} + \nu, \quad d + p \rightarrow {}^{3}He + \gamma, \quad {}^{3}He + {}^{3}He \rightarrow {}^{4}He + 2p \qquad (1.1)$$

Reactions 1.1, may be thought of as the weak decay of the proton in a field of a second proton; the nuclear interaction sets a particular energy binding that makes this possible.

The internal temperature of Stars which are more massive than the Sun, can such be higher to initiate the CNO (Carbon, Nitrogen and Oxygen) cycle. High temperature means greather kinetic energies to the ionized particles present in the core of the Stars. Thus, the Coulombian potential barrier of nuclei can be broken more easily, and the nuclear fussion becomes more efficient for heavier elements.

The CNO cycle includes the following reactions:

$$\begin{aligned} &{}^{12}C + p \rightarrow {}^{13}N + \gamma, \quad {}^{13}N \rightarrow {}^{13}C + e^{+} + \nu, \quad {}^{13}C + p \rightarrow {}^{14}N + \gamma, \\ &{}^{14}N + p \rightarrow {}^{15}O + \gamma \quad {}^{15}O \rightarrow {}^{15}N + e^{+} + \nu, \quad {}^{15}N + p \rightarrow {}^{12}C + \alpha, \\ &{}^{15}N + p \rightarrow {}^{16}O + \gamma \end{aligned} \qquad (1.2)$$

Carbon and nitrogen isotopes act as catalysts, and tend towards a steady-stable abundance pattern, which is called the *equilibrium CNO abundance* [14]. The energy production rate ϵ, for the CNO cycle has the form $\epsilon(T) \sim T^{4}$ [12]. Both the pp-cycle and CNO-cycle determine the so-called *H-burning* phase.

In very massive stars, additional processes can occur leading to the production of heavier nuclei. Because of the hydrostatic inequilibrium, the core of a massive star becomes smaller until the temperature is high enough that the *He-burning* phase can take place and reactions with heavier elements can now occur.

The chemical composition of the nuclear reaction products depends significantly on the ratio Z/N of the number of protons to that of neutrons in one nucleus. For light nuclei with Z$\leq$26, the highest stability is generally reached by the so-called α isotope (when the number of protons and neutrons are equal). It means that the abundances of the yields will be the highest for nuclei with $\frac{Z}{N} \sim 1$ (figure 1.5). Also because of the binding energies, nuclei with even atomic number are most stable, and their abundance are higher with respect to those with odd atomic number. The even-odd effect is a general one, which occurs, right for the same reason, to heavier nuclei. Generally it is assumed that the even to odd nuclei ratio is about

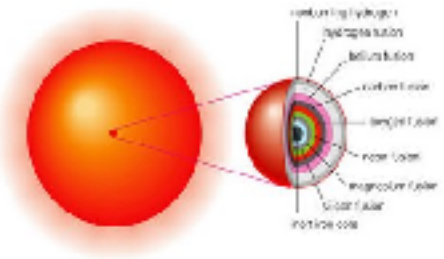

Figure 1.4: Shell structure of a star, containing a central nucleus of heavy elements, and lighter elements in the outer layers.

4. At the final stages of the evolution of massive stars, an "onion" structure is expected: a central nucleus of heavy elements (Fe, ...) and external layers of Silicon, Carbon, Oxygen, Helium and Hydrogen, as sketched in figure 1.4. The formation of elements heavier than iron is discussed in the next section.

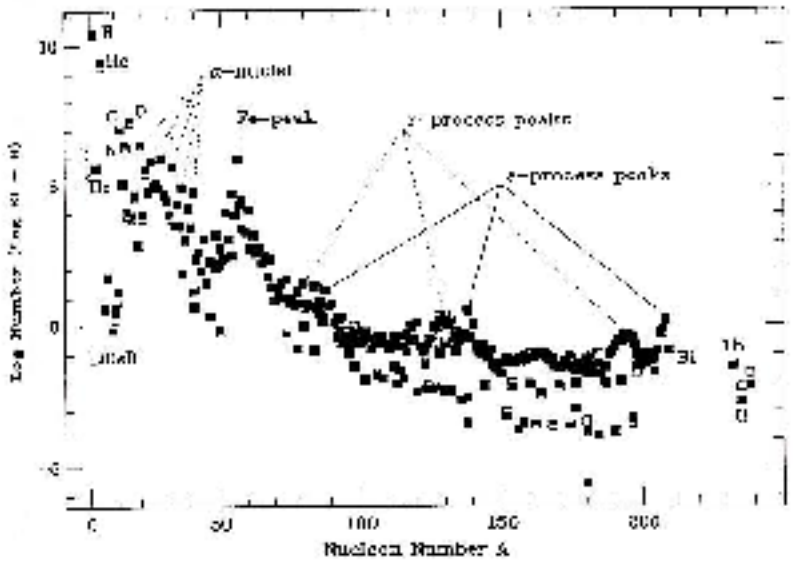

Figure 1.5: Abundance features of elements produced in the star nucleosynthesis. The solid squares are data from the 1989 compilation of Anders and Grevesse, while the open squares are due to Cameron [14]. The stable group of elements called the α-nuclei are indicated, as the sharp peak of iron. Some elements formed by the two different neutron capture process (r-process and s-process) are also indicated.

1.3.2 Neutron Capture Process

Nuclear fusion is efficient up to the production of ^{56}Fe nuclei, since it has the highest binding energy in nature, and the enviromental conditions of any star is capable to induce the breaking of its Coulombian barrier. The production of elements whith A>56 is due to the so-called neutron capture. When a neutron is captured by a nucleus (of mass number A and charge Z), different isotopes can result from the reaction depending on the isotope.

If the neutron has enough time to decay, the process is called *s-process*, otherwise it is called *r-process*. In both processes when a neutron is captured by a nucleus with A nucleons and charge Z the following reaction occurs

$$n + (A, Z) \rightarrow (A + 1, Z) + \gamma \tag{1.3}$$

If the modified isotope is close to the β-decay stability line, one more neutron can decay increasing the charge of the original nucleus

$$(A + 1, Z) \rightarrow (A + 1, Z + 1) + e^{-} + \bar{\nu} \tag{1.4}$$

The main difference between s- and r-processes is the mean time τ_n spent to capture one neutron with respect to the β-decaying time τ_β of the formed radioactive nucleus. If $\tau_n > \tau_\beta$ s-process occurs, generating the so-called s nuclei, whereas r nuclei are produced if $\tau_n < \tau_\beta$, in r-processes.

The s-process imposes certain features on the spectrum of heavy elements abundances. For neutron numbers N = 28, 50, 82, 126, neutron capture cross-section is much smaller than for neighboring nuclei. That means that when "magic numbers" are reached, it become significatly less likely for nuclei to capture more neutrons. These numbers are quantum mechanical effect of closed shells. β-decay half-lives far from the line of stability are of the order of seconds, so the r-process must be very rapid.

1.4 Injection of Cosmic Rays into the ISM

If the ratio of the Galactic Cosmic Rays GCRs to the solar system abundance is plotted versus the first ionization potential (FIP) of each element [1], a definite pattern (so-called FIP effect), is evident, as shown in figure 1.6. In the plot there is a large group of low-FIP elements about 30 times more abundant, relative to H. At a FIP of the order 10 eV there is a rather sharp change; at larger FIP the ratio is about 3.

[1]The first ionization potential measures how easy it is to remove one elctron from the out-most electron shell in the ground state of a neutral atom.

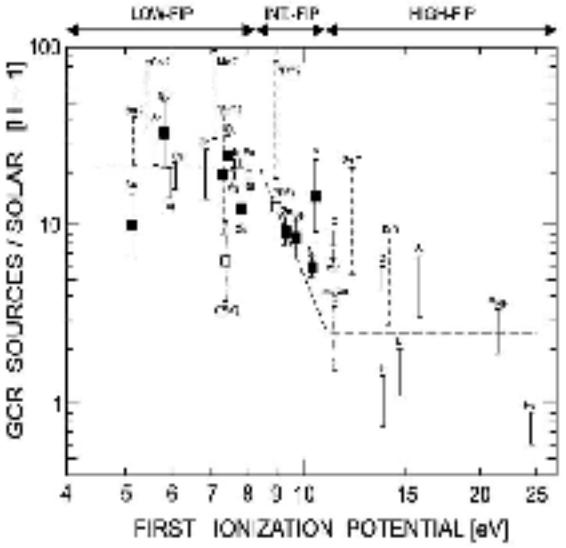

Figure 1.6: The GCRS to Solar relative abundance ratios plotted vs. first ionization potential (FIP) Abundances are normalized to Hydrogen. Solid squares denote those elements which can be used to distinguish between FIP and volatility.

There exists a relationship between the FIP of the various elements and their "volatility", which is measured by the *condensation temperature*[2]. Low-FIP ("refractive") elements are much more abundant than volatile (high FIP) ones. A few elements do not follow the correlation FIP/volatility, in principle, allow a distinction to be made between a FIP effect and a volatility effect in the GCRS composition.

An important question to answer is wether (or not) the CRs have the most powerful acceleration not too far from their injections. The measurement of the isotopic composition of some CR elements can help to provide information about the elapsing time between injection and acceleration. If the abundances of radioactive to stable elements ratio is small, one can state that the original radioactive particle spent enough time after the injection in the acceleration phase so to decay into a stable daughter. If the radioactive to stable ratio keeps more or less constant with respect to what it is believed the original element fractional in sources, it can be saidthat the radioactive particles are efficiently accelerated in the neighborhood of their injection sites (i.e. before they have time to decay), boosting their lifetime enough to arrive in the vicinity of Earth. The actinides as well as some for β-decay isotopes (^{10}Be, ^{14}C, ^{26}Al, ^{36}Cl, ^{54}Mn) could give important information concerning

[2]The condensation temperature is the temperature at which 50% of the dominant solid compound formed by each element has condensed out of the gas phase.

the elasing time, other than serve for computing the duration of the propagation of CRs in the galaxy.

1.5 Propagation Models

The high isotropy and the relatively large number of secondary nuclei present in CRs indicate effective mixing and long travel time for high-energy particles in the galaxy. Semi-empirical models are used to explain the nature of the propagation; the most common framework is the so-called diffusion model.

Leaky box model for our galaxy

The "leaky box" model (Cowsik et al., 1968; Gloeckler and Jokipii 1969), can be considerated as a simplified version of the diffusion model [2]. It describes an equilibrium model, in which the CR sources, and the primary and secondary CR particles are homogeneusly distributed in a confident volume (the box, *i.e.* the Galaxy) and constant in time with no gradient of CR density into any direction. Thus the transport of CRs is not controlled by a real diffusion, but by a hypothetic leakage process at the imaginary boundaries of the box. Their power and space-time distribution is described by the functions

$$\frac{\partial N_i}{\partial t} + \frac{N_i}{T_{CR,l}} + \frac{\partial}{\partial \epsilon_k}(b_i N_i) + \bar{n} v \sigma_i N_i + \frac{1}{\tau_i} N_i = \bar{q}_i + \sum_{j<i} \bar{n} v \sigma_{ij} N_j + \sum \frac{1}{\tau_{ij}} N_j \quad (1.5)$$

where the subscript i characterises the type of nucleon. ϵ_k is the energy per nucleon, v is the velocity of the nucleus; σ_i is the inelastic scattering cross section of a nucleus of type i on nuclei of the ISM; σ_{ij} is the production cross section of nuclei i from heavier nuclei j; τ_i is the lifetime of a nucleus of type i with respect to radioactive decay; $T_{CR,l}$ is a parameter with dimensions of time which characterises the escape from the galaxy, and several quantities are averaged over the volume of the galaxy, like the power of the sources $\bar{q}_i$, the density of the ISM $\bar{n}$, and the rate of loss of energy $\bar{b}_i$. The density of CR in the leaky-box model does not depend on the coordinates. So the leaky-box model can be obtained as a limiting case of the diffusion model, provided that there is a little leakage of particles from the system and strong reflection of the particles at the boundaries of the galaxy [16].

1.6 Geomagnetic Cut-off

The terrestrial magnetic field acts like a barrier to the solar wind. At a distance $\sim$15 Earth radii from the Earth, a shock wave is present due to a the interaction between the terrestrial, and the solar magnetic field; it acts as a natural spectrometer,

which deviates in the backward direction particles according to their rigidity. The rigidity is the p/Z_{eff}, where Z_{eff} is the effective charge of an incompletely ionized ion, and p is the particle momentum. Particles with high rigidity have larger radius of curvature in a magnetic field, thus they can escape more easily; the geomagnetic cut-off is the minimum rigidity for a particle in order to penetrate the Earth magnetosphere (geomagnetic cut-off)[17].

Using the dipolar approximation for the terrestrial magnetic field, the geomagnetic cut-off for positively charged particles is give by:

$$R_{cut-off} = \frac{60}{r^2}\frac{(1-\sqrt{1-\cos\gamma\cos^3\alpha})^2}{(\cos\gamma\cos\alpha)^2} \qquad [GV] \tag{1.6}$$

where, r is the radial distance from the center of the dipole, measured in earth radii, λ is the latitude in dipole coordinate system, and α is the angle between the trajectory of the particle with respect to the magnetic west. Figure 1.7 shows the world map of the geomagnetic cut-off [18].

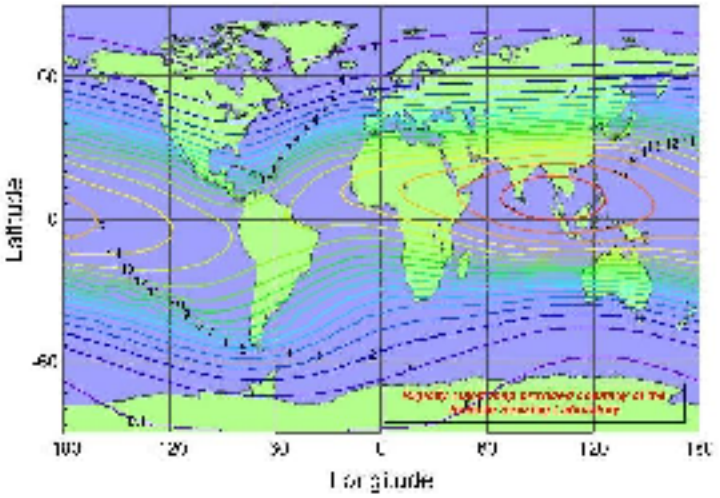

Figure 1.7: World map of the rigidity cut-off values in units of GV [18].

Chapter 2

Rare Heavy Particles

2.1 Introduction

Rare exotic massive particles could be present in the Cosmic Radiation (CR).

Magnetic Monopoles (MMs) might have been produced in the early Universe at the phase transitions corresponding to the breaking of GUT group into subgroups, one of wich is $U(1)$.

Strange Quark Matter (SQM) "nuggets" may arise from various scenarios; they could be formed in highly energetic nuclear collisions associated with the formation of quark-gluon plasma; they might be of cosmological origin, as remnants of the cosmic QCD phase transition, or could be originated in collisions of strange stars [22].

Q-balls are hypothetical aggregates of supersymmetric particles that can be part of the CR arriving on Earth.

Several searches for such particles were made, they still are an item in accelerator-produced particles [26], and in astroparticle physics experiments [27]-[29].

2.2 Magnetic Monopoles

In field theories charges are related with the coupling constants, and their intensity determines the intensity of the coupling (interaction) with the field. The magnetic monopole is an hypothetical particle carrier of the magnetic charge as the electron is the carrier of the electric charge. In electromagnetic interactions, a symmetry between the electric and magnetic field, for the exchange ($\vec{E} \rightarrow \vec{B}$ & $\vec{B} \rightarrow -\vec{E}$) fields exists. In 1931 P.A.M. Dirac [30], derived the following relation between the electric charge e and the magnetic charge g

equation , in order to explain the quantization of the elementary electric charge

e, he could only find an equation which was quantcizing the product $e.g$:

$$eg = n\hbar c/2 \tag{2.1}$$

where n is a positive integer; From (2.1) the unit magnetic charge g_D is $g_D = \hbar c/2e = 68.5e$. The introduction of the magnetic charge would lead to a formal symmetrization of the Maxwell equations, but not numerical by since the unit magnetic charge is much larger than the unit electric charge.

Schwinger (1969) called *dyon* the system formed by the pair e, g.

Electric charge is naturally quantized in Grand Unified Theories (GUT) of the electroweak and strong interactions; they imply the existence of super heavy Magnetic Monopole (MM) called *GUT monopoles*, with calculable properties. 't Hooft and Polyakov (1970) have shown that MMs would appear as stable topological point-like solutions in the early Universe at the phase transition corresponding to the breaking of the GUT group into subgroups, one of which is $U(1)_Y$ [32].

For example one could have the following transitions:

$$SU(5) \underset{10^{-35}s}{\overset{10^{15}\ GeV}{\longrightarrow}} SU(3)_C \times [SU(2)_L \times U(1)_Y] \underset{10^{-9}s}{\overset{10^{2}\ GeV}{\longrightarrow}} SU(3)_C \times U(1)_{EM} \tag{2.2}$$

The MM mass is related to the mass of the X, Y carriers of the unified interaction, $m_M \geq m_X/G$, where G is the dimensionless unified coupling constant at energies $E \simeq m_X$. If $m_X \simeq 10^{14} - 10^{15}$ GeV and $G \simeq 0.025$, $m_M > 10^{16} - 10^{17}$ GeV.

In the standard cosmology the GUT phase transition $SU(5) \longrightarrow U(1)_Y$ would lead to too many poles (*the monopole problem*). A rapid expansion of the early Universe (*inflation*) proposed by Alan H. Guth [33] would defer the GUT phase transition; in the simplest version of inflation the number of generated MMs would be very small. However if there was a reheating phase up to large enough temperatures one would have MMs produced in high energy collisions, like $e^+e^- \rightarrow M\bar{M}$.

The qualitative description of the structure of a GUT MM consists in a very small core, an electroweak region, a confinement region, a fermion–anti fermion condensate (which may contain 4–fermion baryon–number–violating terms); for $r \geq$ few fm a GUT pole behaves as a point particle generating a field $B = g/r^2$ (figure 2.1) [34].

Direct searches for GUT MMs were performed above ground and underground using many different types of detectors. The highest sensitivity to GUT MMs in the CR was reached by the MACRO underground experiment [36]. MACRO

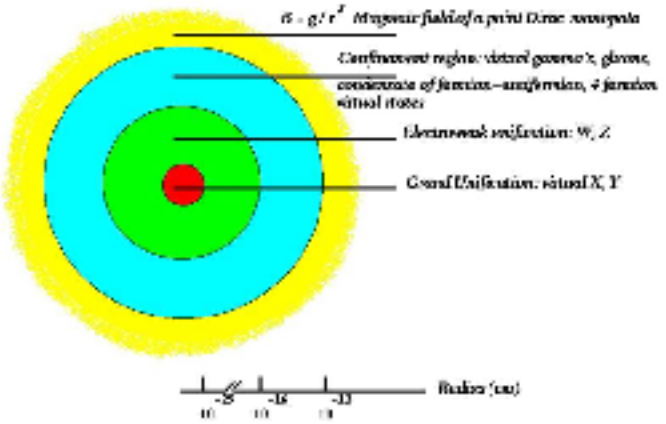

Figure 2.1: Possible structure of a GUT MM, with a core dimention of $\sim 10^{-29}$ cm; for $r > fm$ it behaves as a point particle generating a magnetic field $B = g/r^2$ [34].

performed a search with liquid scintillators, limited streamer tubes and NTDs with an acceptance $\sim$ 10,000 m^{2}sr for an isotropic flux of MMs. The 90% CL flux limits, established for $g = g_D$, are at the level of 1.4×10^{-16} cm^{-2} s^{-1} sr^{-1} for $\beta > 4 \times 10^{-5}$ [37].

2.3 Intermediate Mass Magnetic Monopoles

Magnetic monopoles with masses of $10^5 - 10^{12}$ GeV, (Intermediate Mass Magnetic Monopoles IMMs), are predicted by theories with an intermediate mass scale [38]. They would appear as topological point defects in the Early Universe at a later times than the GUT phase transition.

It was suggested that IMMs could be generated, if the GUT group yields the $U(1)$ group that describes the electromagnetic interaction in the Standard Model in the following two steps [35]

$$SO(10) \xrightarrow[10^{-35}\text{s}]{10^{15}\ GeV} SU(4) \times SU(2) \times SU(2) \xrightarrow[10^{-23}\text{s}]{10^{9}\ GeV} SU(3) \times SU(2) \times U(1) \tag{2.3}$$

A possible structure of the IMM is illustrated in figure 2.2. The various regions correspond to the intermediate mass scale core of $R \simeq 10^{-25} cm$; the electroweak scale shell; then the shell containing the condensate fermion-anti fermion pairs, similar to the GUT case, but which does not contain any term violating baryon number conservation; a confinement shell region; and the outests region, corresponding to

a the magnetic field of a point Dirac monopole [34].

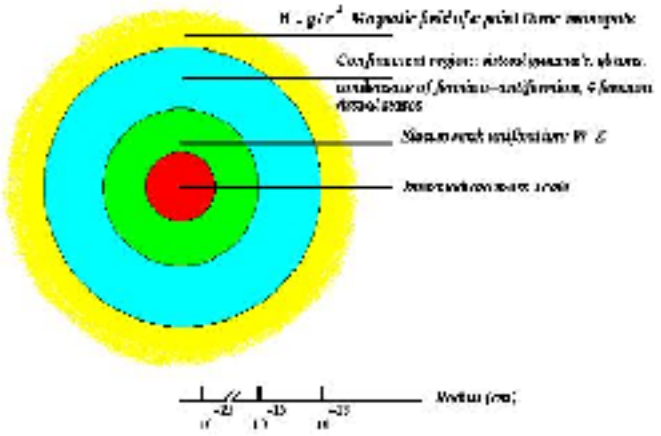

Figure 2.2: Possible structure of an IMM. The inner region ($r \simeq 10^{-25} cm$) corresponds to the intermediate mass scales; inside this region one should find the intermediate mass bosons responsible for the symmetry breaking. The outer regions are the condensate region, the confinement region, and the magnetic field of a point Dirac monopole [34].

IMMs may be accelerated to high γ in the galactic magnetic field. The energy W acquired in a coherent region of the galactic magnetic field B is [39]

$$W = n g_D B_l = n\ 20.5\ keV/Gcm \tag{2.4}$$

In a coherent galactic length $l \simeq 1$ kpc, with $B \simeq 3\mu G$, $W \simeq 1.8 \times 10^{11}$ GeV. Thus one may look for $\beta \geq 0.1$ IMMs [35].

2.4 Strange Quark Matter

Strange Quark Matter (SQM) which should consist of aggregates of up (u), down (d) and strange (s) quarks in almost equal proportions; has been proposed as the fundamental state of nuclear matter [47]

In quark matter it can happen that quarks u and d, forced to occupy high energy states, transform into an s quark, by means of the weak interaction. The weak interactions occur until the Fermi energy of all flavors is the same. At the density level of nuclear matter the Fermi energy is $\sim$ 300 MeV; other quark flavors (c, b, and t) do not appear because their masses are large compared to 300 MeV. It is possible that SQM with non zero mass of the quark s ($m_s \neq 0$) has an energy per baryon smaller that 938 MeV, and be more stable than nuclear matter [46]. In

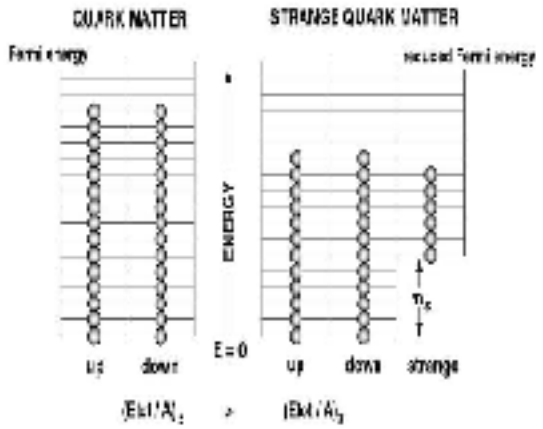

Figure 2.3: Diagram of the energy levels for ordinary quark matter and for SQM. By introducing the s quark the total Fermi energy of the system is decreased [46].

figure 2.3 it is sketched a possible energy level diagram compared to ordinary nuclear matter. SQM should have a constant density $\rho_N = M_N/V_N \simeq 3.5 \times 10^{14}$ g cm^{-3}, slightly larger than that of atomic nuclei (10^{14} g cm^{-3}), and it should be stable for all baryon numbers in the range between ordinary heavy nuclei and neutron stars ($A \sim 10^{57}$) [44]. SQM could have been produced shortly after the Big Bang; they could also appear in violent astrophysical processes, such as neutron star collisions; and it could be a component of Cold Dark Matter.

In SQM the number of s quarks should be lower than the number of u or d quarks; globally SQM should have a relatively small positive integer charged core. The overall neutrality of SQM is ensured by an electron cloud which surrounds it, forming a sort of atom. The number of electrons is given by $N_e \simeq (N_d - N_s)/3$, where N_d and N_s are the number of quarks d, and s respectively, assuming $N_d = N_u$ [49]. A qualitative picture of SQM structure is shown in figure 2.4 [34], where the full line circle represent the core and the dashed line the overall size. Electrons are represented by dots. A classification of SQM depending on their mass and baryon number varies depending on the authors. In this thesis SQM aggregates are classificated into "nuclearites" and "strangelets". The word "*nuclearite*" was introduced to indicate large lumps of SQM which could be present in the CR [47, 48]. *Nuclearites* are neutral objects with some or all the electrons inside the core, see figure 2.4. Nuclearite should have galactic velocities, $\beta \sim 10^{-3}$, and for masses larger that 0.1 g could traverse the Earth [35]. Strangelets with masses up to the multi-TeV region could be ionized and could be accelerated to relativistic velocities by the same astrophysical mechanisms as for ordinary nuclei of the primary Cosmic Rays [50].

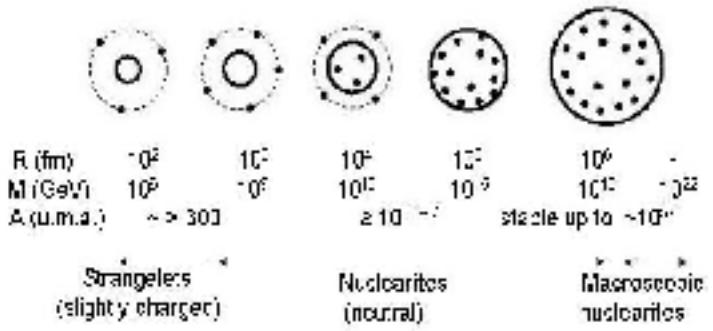

Figure 2.4: Sketch of the strange quark matter structure: the quark bag core (radius R_N, indicated with a solid line) and of the core+electron system; the black points are electrons (the border of the core+electron cloud for small nuclearite masses is indicated by dashed lines). A classification for the SQM according to their mass and radius is shown. In this thesis we indicated as: *Strangelets* with masses $< 10^9$ GeV, which have electrons outside the core. *Nuclearites* with masses $10^9 < m < 10^{17}$ GeV, have some or all the electrons inside the core. *Macroscopic Nuclearites* with $m > 10^{17}$ GeV, have all the electrons inside the core.

According to the ratio Z/A, strangelets can be classified in two types; "ordinary" or "CFL" strangelets. The first type (ordinary) has the following relationship between Z and A [51]

$$\begin{aligned} Z &\simeq 0.1\left(\frac{m_s}{150MeV}\right)^2 A; \qquad A < 10^3 \\ Z &\simeq 8\left(\frac{m_s}{150MeV}\right)^2 A^{1/3}; \qquad A > 10^3 \end{aligned} \tag{2.5}$$

with m_s is the mass of the strange quark. In figure 2.5 the two relations are shown by blue and black curves.

Madsen [52] assumed that quarks with different color and flavor quantum numbers form Cooper pairs inside the SQM, (so-called "color flavor locked" CFL phase), increasing the stability of the strangelets, because of the very large binding energy. The charge to mass relation of CFL strangelets may be

$$Z \simeq 0.3\left(\frac{m_s}{150MeV}\right)^2 A^{2/3} \tag{2.6}$$

where m_s is the mass of the strange quark. Figure 2.5 shows the charge to barion number function, shown by a red curve.

2.4.1 Models of Strangelet Propagation in the Atmosphere

Two main scenarios are discussed here, one proposed by G.Wilk et al. [56], and the other proposed by S. Banerjee et al. [57].

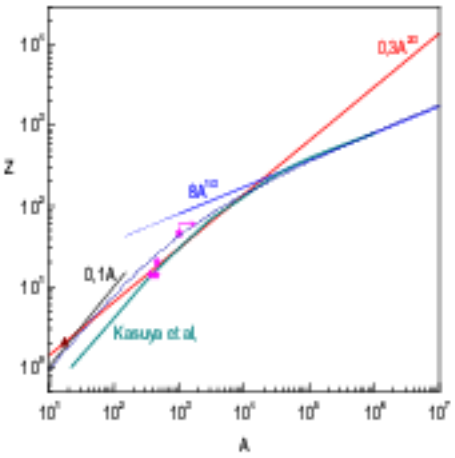

Figure 2.5: Possible electric charge number *vs.* baryon number relation as explained in the text. Possible candidates events are also shown, [54].

In [56] it was assumed that in penetrating the atmosphere strangelet's size and mass are reduced through successive interactions with the atomic air nuclei. This scenario is based on the spectator-participant picture. Two interaction models are considered: quark-quark (called *standard*), and collective (called *tube-like*). At each interaction the strangelet mass is reduced by about the mass of a nitrogen nucleus (in the standard model), or by more (in the tube-like model), while the spectator quarks form a lighter strangelet that continues its flight with essentially the same velocity.

The mean interaction length of a strangelet of mass number A in the atmosphere is given by

$$\lambda_{S-air} = \frac{A_{air} m_S}{\pi(1.12 A_{air}^{1/3} + r_0 A^{1/3})} \tag{2.7}$$

where r_0 is the scaling factor of the strangelet radius $R = r_0 A^{1/3}$.

A critical mass is reached around $A_{crit} \simeq 300 - 400$, when neutrons would start to evaporate from strangelets; for $A \leq 300$ SQM would became unstable and decay into normal matter [50]. The mean atmospheric depth h penetrated by the strangelet before reaching its critical stability mass is given by

$$h = \sum_{k=0}^{N} \lambda_k \tag{2.8}$$

$N = \frac{A_0 - A_{crit}}{A_{air}}$ is the mean number of interactions. In figure 2.6 (A) it is shown the decrease of the strangelet's size with the atmospheric depth h, for two different initial masses; the critical mass values are indicated by circles.

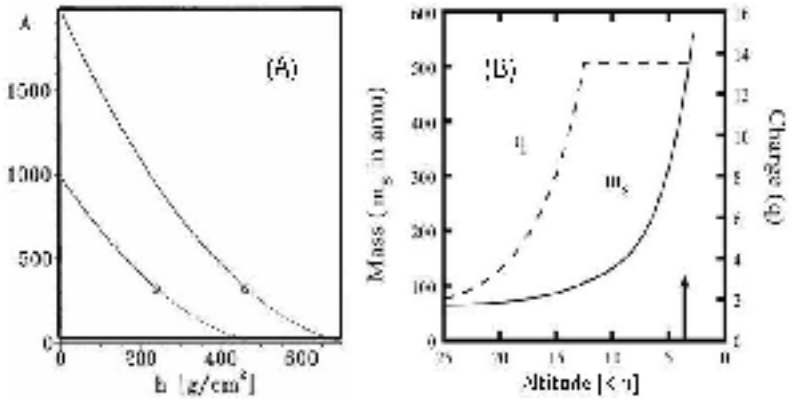

Figure 2.6: Propagation models: (A) *First model:* prediction of the decrease of the baryon number A of a strangelet *vs.* the atmospheric depth h traversed for two different initial sizes: A_0 =1000 and A_0 =2000 (dotted lines correspond to $A < A_{crit}$) [56]. (B) *Second model:* Strangelet mass and charge increasing with decreasing altitude [57].

A second model of propagation of strangelets in the atmosphere, proposed by [57], assumes that small strangelets arriving at the top of the atmosphere would pick-up nuclear matter during interactions with air nuclei, accreting neutrons and protons. After each interaction, the strangelet mass would increase by about the atomic mass of nitrogen, with a corresponding reduction of velocity. This mechanism also imply an increase of the electric charge of the strangelet, thus an increase of the Coulomb barrier. Figure 2.6 (B) shows the predictied increase of the strangelet mass, for a given initial mass, with decreasing altitude (increasing atmospheric depth). In the same picture the increment of the charge is indicated by a dashed curve.

2.5 Q-balls

Q-balls should be aggregates of squarks $\tilde{q}$, sleptons $\tilde{l}$ and Higgs fields [59]. The scalar condensate inside a Q-ball core has a global baryon number Q (and may be also a lepton number). We assume that the Q numbers of quarks and squarks are equal to 1/3 ($Q_q = Q_{\tilde{q}} = 1/3$) or 2/3 ($Q_q = Q_{\tilde{q}} = 2/3$). Protons, neutrons and may be electrons could be absorbed in the condensate.

The Q-ball mass M_Q, core size R_Q and global quantum number Q are related

by the following relations [62]

$$M_Q = \frac{4\pi\sqrt{2}}{3} M_s Q^{3/4} \simeq 5924 M_s(TeV) Q^{3/4}(GeV) \tag{2.9}$$

$$R_Q = \frac{1}{\sqrt{2}} M_s^{-1} Q^{1/4} \simeq 1.4 \times 10^{-17} M_s^{-1}(GeV)^{-1} Q^{1/4}(cm) \tag{2.10}$$

where the parameter M_s is the energy scale of the SUSY breaking symmetry.

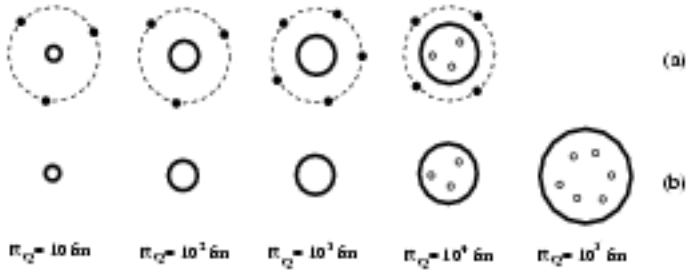

Figure 2.7: Sketch of the Q-ball structure: (a) SECS; (b), SENS. The black points represent electrons, and the empty dots s-electrons (supersymmetric partner of the electron).

There could exist neutral and charged Q-balls. Supersymmetric Electrically Neutral Solitons (SENS) are generally more massive and may catalyze proton decay. SENS may obtain a positive electric charge when absorbing a proton in their interactions with matter yielding SECS (Supersymmetric Electrically Charged Solitons), which have a core electric charge, have generally lower masses and the Coulomb barrier could prevent the capture of nuclei. SECS have only integer charges because they are color singlets. In figure 2.7 [34] is shown a sketch of SECS and SENS. A SENS which enters the Earth atmosphere could absorb a nitrogen nucleus and would thus become a SECS with charge $z = 7$. Other nuclear absorptions may be prevented by Coulomb repulsion. If the Q-ball can absorb electrons at the same rate as protons, the positive charge of the absorbed nucleus may be neutralized by the charge of absorbed electrons. If, instead, the absorption of electrons is slow or impossible, the Q-ball carries a positive electric charge after the capture of the first nucleus in the atmosphere.

2.6 Cosmological and Astrophysical Bounds to Fluxes of Rare Massive Particles

Theories do not predict the abundances of MMs. Bounds have been derived based on astrophisical plus cosmolocal considerations.

Galactic magnetic fields of $\sim 3\mu G$, are probably due to the non-uniform rotation of the galaxy, which generates a field with a time-scale of the order of the rotation period of the galaxy $\sim 10^8\ yr$. An upper bound to the MM flux Φ is obtained by requiring that the kinetic energy gained per unit time by MMs be less than the magnetic energy in the galaxy generated by the dynamo effect. The value obtained of $\Phi < 10^{-15}\, cm^{-2}s^{-1}sr^{-1}$ [64], is called the "Parker bound"; the bound is indicated by a red dashed line in figure 2.8. Taking into account the almost chaotic nature of the galactic magnetic field, with domains of $\sim 1\ kpc$, the limit becomes mass dependent [65]. An "extended Parker bound" was obtained by requiring survival and growth of a galactic seed field [66], yielding $\Phi \leq 10^{-16}(m_{MM}/10^{17}GeV)\ cm^{-2}s^{-1}sr^{-1}$.

Magnetic monopole, are considered possible components of the galactic cold dark matter. Assuming a local dark matter energy density of $\rho \sim 0.3$ GeV$/cm^3$ and that MMs, nuclearites and/or Q-balls could be part of it and have typical velocities of $\beta \simeq 10^{-3}$, an upper limit on their flux is obtained in [67]. By the same considerations that can be applied to Nuclearites and Q-balls.

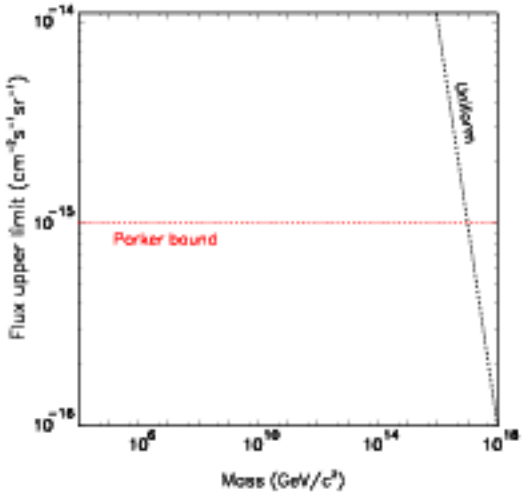

Figure 2.8: *Parker bound:* cosmological upper bound limit to the MM flux. *Uniform:* Flux upper limits for nuclearites and for Q-balls vs. their masses, assuming that they have $\beta = 10^{-3}$ and that each of them saturates the local dark matter density. If the abundance of each of them is 10^{-3} of the cold dark matter, the limits are 10^{-3} smaller [34].

In figure 2.8 the Parker bound and the galactic bound are shown for MMs versus their masses.

Chapter 3

Solid State Nuclear Track Detectors

Heavily ionizing particles passing through some materials like mica, glasses, various mineral crystals and plastics [1], produce damaged regions. In crystlas this consists of atomic displacements, manifesting themselves as interstitials and vacancies, and surrounded by a region of considerable lattice strain. In plastics the radiation damage produces changes in the molecular structure, *i.e.* broken molecular chain, free radicals, etc. The narrow trails of damage are called *"latent tracks"* and have typical sizes at the order of $\sim$ 10 nm. Certain chemical reagents ("etchants") dissolve these damaged regions with at a higher rate than the undamaged material and this etched track may be enlarged until it is visible under an optical microscope.

The two types of Nuclear Track Detectors (NTDs) used in this thesis are CR39 and Makrofol. The chemical composition of CR39 is $(C_{12}H_{18}O_7)_n$ it is a thermoset plastic. Thermosets polymer are materials that cure, through the addition of energy, to a stronger form. The CR39 density is $\rho_{CR39} = 1.32\ g/cm^3$, and the ratio of the atomic weight and the atomic number is $A/Z = 1.877$. CR39 is a trade marked product of PPG Industries[2], originally developed by Columbia Chemical Co Inc. The CR39 used in the experiments discussed in this thesis was produced by the Intercast Co.[3]. A special batch of CR39, containing 1% of dioctyl phthalate (DOP) into the polymer, was also used. The optical and etching properties of CR39 can be improved by incorporating such additives [68].

Makrofol and Lexan with chemical composition $(C_{16}H_{14}O_3)_n$ or bisphenol-A polycarbonate are polycarbonate resin thermoplastics. A thermoplastic melts to a

[1] Plastic is the general term for a wide range of synthetic or semi synthetic polymerization products. Polymerization is a process of bonding monomers, or "single units" together through a variety of reaction mechanisms to form longer molecular chains named polymers.

[2] http://www.ppg.org

[3] www.intercast.it

liquid when heated and freezes to a brittle, very glassy state when cooled sufficiently. The Makrofol/Lexan density is $\rho_{makrofol} = 1.29\ g/cm^3$, and the ratio $A/Z = 1.896$. Lexan is a registered trademark for General Electric Co., and Lexan is produced by Bayer AG Co.

The molecular structure for each detector is represented in figure 3.

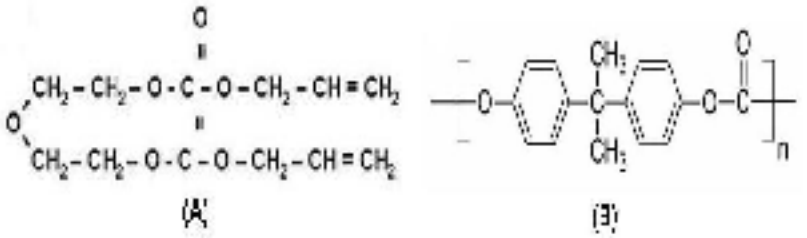

Figure 3.1: (A) Chemical structure of CR39, (B) chemical structure of Makrofol/Lexan.

3.1 Track Formation and Geometry

The main processes that charged particles undergo in a medium are

i. Ionization and excitation. The electrostatic force between the particles and the electrons surrounding the target nuclei can strip these electrons from their orbits, or excite the electrons to less tightly bound states.

ii. Bremsstrahlung. The deceleration of the incident particles produce emission of electromagnetic radiation. This process is important for light particles, such as electrons, and large energies.

iii. Electrostatic forces can act directly between the moving ion and the target nuclei themselves, and can result in the ejection of target atoms from lattice sites or out of molecular chains.

The initially generated primary products (*i.e.* ions; excited atoms and molecules; free electrons) rapidly undergo secondary reactions (dissociation of some excited molecules, etc.), until thermodynamic equilibrium is reached. This is followed by a *chemical* stage, in which ions and free radicals react with each other and with other atoms and molecules to yield the final products of the irradiation.

3.1.1 Restricted Energy Loss

In NTDs the energy lost by an incident particle causing a called *latent track*, is the Restricted Energy Loss (REL). In CR39, when the incoming particle has a velocity $\beta c < 10^{-2}c$ the REL is equal to the total energy loss in the medium [69]. For particles with velocities $\beta c > 10^{-2}c$, the REL is a fraction of the electronic

energy loss, leading to δ-rays with energies lower than E_{max}, with $E_{max} = 200$ eV for CR39, and 350 for Makrofol/Lexan [70]. The REL expression is obtained from the *Bethe-Bloch* expression for energy loss of electrically charged particles, by introducing an energy cutoff [71]

$$-\frac{dE}{dx}\Big|_{T<T_{cut}} = K\frac{Z}{A}\frac{z_i^2}{\beta^2}\left[\ln\left(\frac{2m_e\gamma^2c^2\beta^2T_{upper}}{I^2}\right) - \frac{\beta^2}{2}\left(1+\frac{T_{upper}}{T_{max}}\right) - \frac{\delta}{2} - 2\frac{C}{Z}\right] \quad (3.1)$$

where $K = 4\pi N_A r_e^2 m_e c^2 = 0.307075\ MeVcm^2/g$, r_e and m_e the classical electron radius and mass. N_A is the Avogadro's number; and Z/A is the ratio between the atomic number and the atomic weight of the absorbing material (*e.g.* $Z/A\Big|_{CR39} = 0.53$). z_i is the charge of the incident particle, and $\beta = v/c$ its velocity. I is the mean excitation potential, a main parameter in the Bethe-Block formula, and is essentially the average orbital frequency $\bar{\nu}$ from Bohr's formula times Planck's constant, $h\bar{\nu}$. In practice this is a very difficult quantity to calculate, instead values of I for several materials have been deduced from actual measurements of dE/dx and a semi-empirical formula for I *vs* Z was deduced [72]. One such formula is

$$\begin{aligned} \frac{I}{Z} &= 12 + \frac{7}{Z}eV \qquad Z < 13 \\ \frac{I}{Z} &= 9.76 + 58.8Z^{-1.19}eV \qquad Z \geq 13 \end{aligned} \quad (3.2)$$

e.g. for CR39 the mean excitation potetial is $I_{CR39} = 70\ eV$. T_{max} is the maximum energy transfer in a single collision (maximum possible electron recoil kinetic energy), and for an incident particle of mass M, kinematics gives

$$T_{max} = \frac{2m_ec^2\beta^2\gamma^2}{1 + 2\gamma m_e/M + (m_e/M)^2} \quad (3.3)$$

in the low energy approximation, $T_{max} \sim 2m_ec^2\beta^2\gamma^2$. The limit energy loss in a single collision is given by the value T_{cut} ($T_{cut} < T_{max}$), and T_{upper} is the lesser of T_{cut} and T_{max}, *e.g.* $T_{cut} = 200$ eV for CR39, and $T_{cut} = 300$ eV for Lexan.

Figure 3.2 is an example plot, showing the case of the energy loss of $\pi^{\pm}$ in copper $Z = 26$ for a $T_{cut} = 0.5$ MeV, and $I = 322$ eV.

The *density effect* arises from the fact that the electric field of the particles also tends to polarize the atoms along its paths. This effect becomes more important at higher energies of the incident particle, and depends on the density of the material, since the induced polarization will be greater in condensed materials. Values for δ are given by [73]

$$\delta = \begin{cases} 0 & X < X_0 \\ 4.6052X + d + a(X_1 - X)^m & X_0 < X < X_1 \\ 4.6052X + d & X > X_1 \end{cases} \quad (3.4)$$

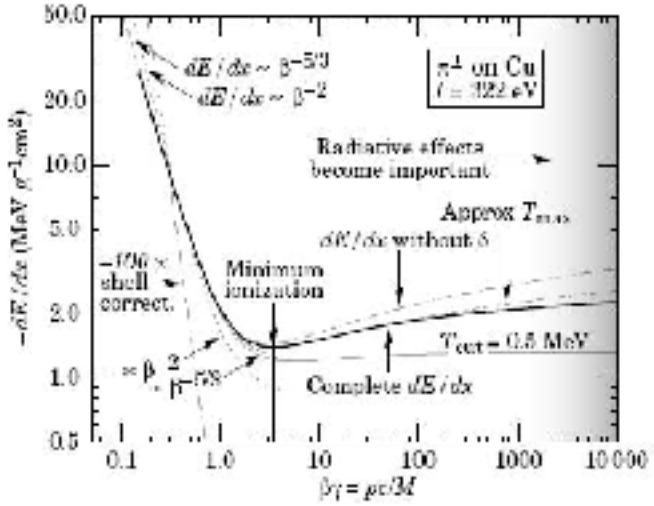

Figure 3.2: Energy loss rate of charged pions in copper, evaluated for a cut-off at $T_{cut} = 0.5$ MeV. The function without the density effect is also plotted with a dashed line, as is the shell correction at low velocities enhanced by a factor 100. Two low-energy approximations ($\sim \beta^{-2}$, $\beta^{-5/3}$) are also plotted [71].

where $X = \log_{10}(\beta\gamma)$, and X_0, X_1, d, a, and m depend on the absorbing material. *e.g.* table 3.1 show constant values for the parameters X_0 , X_1, and m for NTD's [70].

material	I(eV)	X_0	X_1	m
CR39	70	0.2	2.0	3.0
CR39 DOP	70	0.2	2.0	2. 0
Lexan	100	0.2	0.3	0.3

Table 3.1: Constants for the density effect correction for some NTD's.

The parameters d and a are defined as

$$d = -\left(2\ln\left(\frac{I}{\hbar\omega_p}\right) + 1\right), \qquad a = \frac{d+4.6052X_0}{(X_1 - X_0)^m} \tag{3.5}$$

with

$$\omega_p = \sqrt{\frac{N_e r^2}{\pi m_e}} \tag{3.6}$$

here $N_e = N_A \rho Z/A$ is the electron density. At low energy the density effect is negligible. In figure 3.2 is shown the contribution of δ to dE/dx, for the $\pi^{\pm}$ in Cu

case.

The *shell* correction accounts for effects which arise when the velocity of the incident particle is comparable or smaller than the orbital velocity of the bound electrons. At this velocity the assumption that the electron is stationary with respect to the incident particle is no longer valid. The correction is small and is given by the empirical formula, valid for $\eta \geq 0.1$:

$$\begin{aligned} C(I,\eta) = &(0.422377\eta^{-2} + 0.0304043\eta^{-4} - 0.00038106\eta^{-6}) \times 10^{-6} I^2 \\ &+ (3.850190\eta^{-2} - 0.1667989\eta^{-4} + 0.00157955\eta^{-6}) \times 10^{-9} I^3 \end{aligned} \tag{3.7}$$

where $\eta = \beta\gamma$ and I is the mean excitation potential in eV. In plot 3.2 is shown the effect of the shell correction enhanced 100 times, for the example of $\pi^{\pm}$ on Cu.

The REL formula (3.1) smoothly joins the standart Bethe-Block formula function for $T_{cut} > T_{max}$.

3.1.2 Chemical Etching and the Reduced Etch Rate

When a particle passes through a NTD, it causes a damage called *latent track* (LT). The Latent Track can be made visible to an optical microscope by chemically etching the detector. The etchants are highly basic or acid solutions, *e.g.* aqueous solutions of NaOH or KOH of different concentrations and temperatures, usually are in the range $40 \div 70^{\circ}$C.

Etching takes place via rapid dissolution of the disordered region of the LT which exists in a state of higher free energy than the undamaged bulk material. Along the LT the material is removed at a velocity v_T, and a velocity v_B from the bulk material, the removed material. v_B depends only on the etching solution *i.e.* its concentration and temperature. v_T depends on the chemical etching conditions, and also on the energy loss of the incident particles.

The *reduced etch rate* p is defined as $p = \frac{v_T}{v_B}$, and if $v_T > v_B$ (p>1) etch-pit cones are formed. In figure 3.3 (A-B) are shown steps of formation for a particle inpinging normally on the detector. Figure 3.3 (C) shows a photograph of etch-pit cones, observed at a tilted angle. Made it to show the cones formed on the two sides of the detector.

For a particle drecreasing its kinetic energy, the REL changes and this determine that v_T also changes along the LT. In this case the opening angle of the etch-pit cone becomes smaller. For a particle stoping inside the detector, if the chemical etching continues beyond the track range, the cone end develops into a spherical shape (*end of range* tracks).

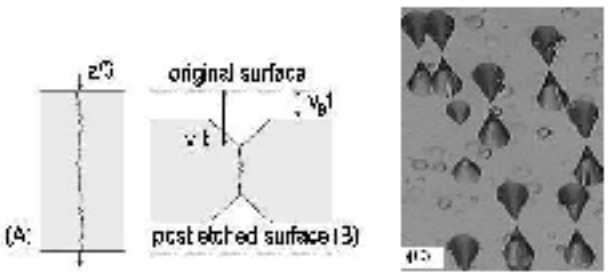

Figure 3.3: (A) Scheme of the latent track left by the passage of an ionizing particle through a NTD. (B) Formation of etch-pit cones.(C) Micro photograph of etch-pits, from an ^{26+}Fe beam of 0.414 AGeV. The photograph was taken with an tilted angle (around 45°), to show both the upper and lower cones.

3.1.3 Track Geometry of Etch-pit Cones

The most easily measurable parameters of an etched track are the etched-cone length L_e, and the major and minor semi axes a, b of the etch-pit opening, figure (3.4). In general the projection of the track on the detector's surface (cone base) is elliptical. If the incidence is perpendicular to the detector surface the cone bases are circular. The *reduced etch rate* p can be determined by using the following relation

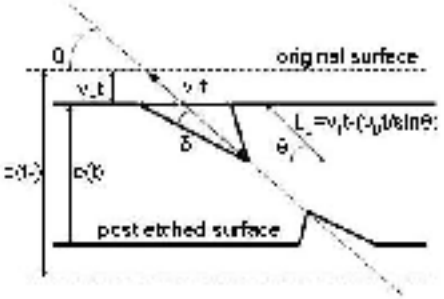

Figure 3.4: Track formation geometry. The scheme represents the case of an inclined track, impinging the detector surface at an angle θ. $e(t_0)$ is the original detector thickness, and $e(t)$ is the thickness after an etching time t. The removed bulk material is $v_B t$, and along the latent track it is equal to $v_T t$. The etch-pit cone high L_e is equal to $v_T t - (v_B t/\sin\theta)$. The angle δ is the opening angle of the etch-pit cone.

$$p = \sqrt{1 + \frac{4A^2}{(1-B^2)^2}} \tag{3.8}$$

with $A = \frac{a}{2v_B t_{etch}}$ and $B = \frac{b}{2v_B t_{etch}}$, where t_{etch} is the etching time. v_B is obtained by measuring the variation of the thickness of the detector, before and after the

etching, refearing to figure 3.4,

$$v_B = \frac{1}{2}\frac{e(t_0) - e(t)}{(t - t_0)} \tag{3.9}$$

where t_0 is the initial time, and t is the etching time; $e(t_0)$ is the initial thickness (before the etching) and $e(t)$ is the post etch thickness. The incident angle with respect to the detector surface can also be determined:

$$\theta = \sin^{-1}\left(\frac{1}{p}\frac{1+B^2}{1-B^2}\right) \tag{3.10}$$

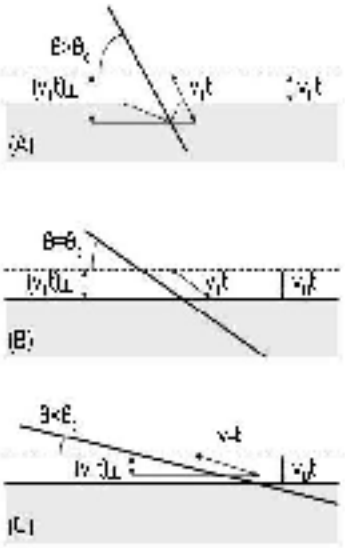

Figure 3.5: (A) If the impinging angle θ is greather than the critical angle, the particle is registered by the detector sheet. (B) The limit case of detection is for $\theta = \theta_c$. (C) When the impinging angle is smaller than the critical angle, the track is not recorded, and the bulk material is consumed faster than the material along the latent track.

3.1.4 NTD Detection Limit Angle

If the component of the track etch velocity normal to the surface $v_{T\perp}$ (or the material removed along this path) is equal to the bulk velocity v_B (or the bulk material removed), the tip of the etch cone never keeps ahead of the advancing surface, so the etch-pit can not form. The angle θ_c, defined by

$$\sin\theta_c = \frac{1}{p} = \frac{v_B}{v_T} \tag{3.11}$$

is the critical (or limit) angle of detection and represents the minimum angle with respect to the detector surface for a particle to be detected, provided it is above the detector threshold. Figure 3.5 shows the different cases when the impinging angle is greater than θ_c, so the track is visible. When $\theta = \theta_c$ is the limit case of the track formation, and $\theta < \theta_c$ when the track is no longer recorded by the NTD. The limit angle for Fe $Z = 26$ ions, in CR39 with $v_B = 1.15$ μm/h is $\theta_c \sim 60°$, *i.e.* all Fe ions impinging on a CR39 detector foil are recorded for about $\theta > 60$.

3.2 Calibrations of the NTDs

In order to determine the detector response, that is a relation between the reduced etch rate p and REL, different stacks of NTD's were exposed to ion beams of fixed energy perdifferent charges and energy, at the CERN-SPS, BNL (USA), HIMAC (Japan).

The stacks composition used in our calibrations are formed by piled up sheets of NTD, placed before and after the target (figure 3.6). Targets were of different materials, Al, Cu, polythylene, etc. about 1 cm thick.

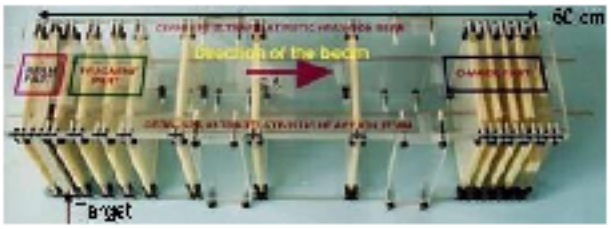

Figure 3.6: Stack used for calibration of CR39 exposed to 1GeV/nucleon iron beam at CERN.

Ion beam particles are recorded by the detector layers before the target.When the beam interact with the target, fragments are produced, and all the products of the interaction are recorded in the sheets piled up after the target.

After the exposure, detectors are chemically etched, with a set of chemical conditions from which the detector response depend strongly (because of the dependence of the bulk velocity on these parameters). In this way tracks are enhanced and are ready to be measured with optical microscopes.

The incident beams used for calibration usually are normally impinging to the detector surface, so the cone bases of the etch-pits cones are circular with diameter

D. In this case p, can be evaluated using[4]

$$p = \frac{1 + (\frac{D}{2v_B t_{etch}})^2}{1 - (\frac{D}{2v_B t_{etch}})^2} \tag{3.12}$$

The area distribution of the etch-pit cones (tracks) recorded in the detectors after the target, is a function of the charge of the fragments. To increase the resolution of the etch-pit area distribution (yilding also to a better resoltion in the charge assignement) tracks are measured over several sheets of the stack, and then their trajectories are reconstructed over the stack. For tracks passing through the stack their semi axis, and area are averaged. Figure 3.7 shows the area distribution averaged over 4 sheets of CR39 exposed to the CERN Pb^{82+} beam of 158 A GeV.

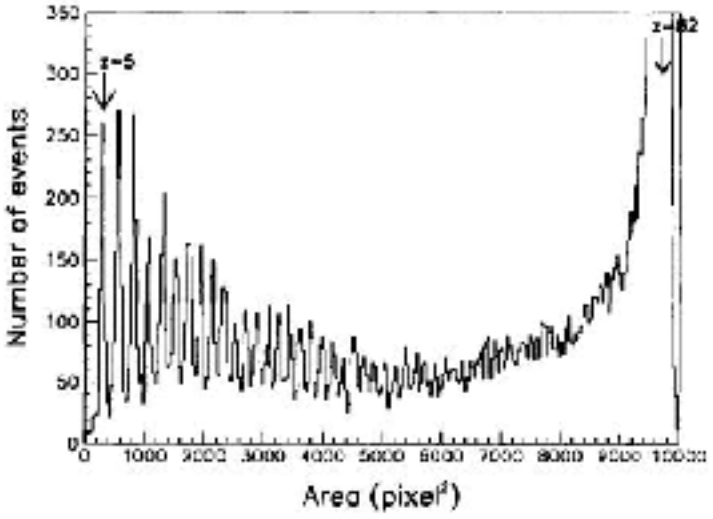

Figure 3.7: Surface etch-pit are distribution of the CR39 exposed to a Pb^{82+} beam of 158 A GeV; the CR39 was etched in NaOH 6N at 70° for 30 hours. The surface area were averaged over 4 sheets.

Figure 3.7 shows that the area increase with the increasing ion charge; thus nuclear fragments may be detected as a change in the area of the tracks. Using equation 3.1 the REL for each fragment can be computed.

The so called "calibration plot" is obtained, plotting the REL vs. p for each fragment.

For this thesis different "calibrations" where obtained, using different chemical etching conditions, different beam energies and different kind of ions. Each calibration will be described in detail in the chapters relative to each experiment, chapters 4 and 6.

[4]In general p is independent of the ions impinging angle. The independence was tested experimentally using tilted calibration beams, for details see [70].

3.3 The Data Acquisition System

The detectors used for calibration, and all the detector sheets of the CAKE experiment were measured with the SAMAICA automatic data acquisition system.

The SAMAICA (Scanning And Measuring with Automatic Image Contour Analysis) system is a product of ELBEK-Bildanalyse Gmbh, Germany. It is intended for automatic measurement of solid state track detector foils. Our configuration consists of the following hardware components (a short description on their working procedure is also given)

- a personal computer (PC)
- graphics adapter (VGA)
- a built in frame grabber (image analyser which reconstruct the image), based on two microprocessors, 32-bit MC 68020 (@ <33 MHz) and 32-bit MC 68881 (@ <50 MHz), interfaced with the PC by a serial RS232 terminal line.
- Zeiss Axiotron microscope with variable magnifying power (set of 4 objetives, lodged in a rotating slit). The objetives magnification are 5X (1608×1249 μm^2), 10X (796×623 μm^2), 20X (406×316 μm^2), 50X. The field of view (FOV) measured for each objetive is indicated in parenthesis.
- autofocus system †
- black/white Hamamatsu C3007 CCD camara with 744×576 pixel with resolution CCIR. The spectral responce ranged from $\lambda = 300$ nm and $\lambda = 1100$ nm with a maximum sensitivity of 100% at $\lambda = 550$ nm.
- monochrome SONY XC 77CE video camera, 2/3" CCA BW of 11×11 μm. 50 frame/second. Effective pixel elements 756×581, elements in video out 739×575. Cell size 11×11 μm^2, sensytive area 8.8×6.6 cm^2. The camera is syncronized with an external sync signal from the PC.
- display monitor
- XY-stage with 1mm spindle pitch. The plane is defined on a 20×30 cm^2 aluminium plate where the detector foils are lodged. The plate is equipped with an air-sucking channel (9×8 cm^2) used to fix the sheets. The positioning precision is limited due to errors of the spindle (< 10 μm), with a systematic error ($\pm$ 10 μm) which caused a constant deviation of the absolute position due to mechanics and statistical uncertainty due to repeated positioning movements [70].

- Märzhäuser stage controller with a spindle pitch of 2 mm. Is equipped with a joystick and a RS232 interface for remote control by the PC (40000 microsteps per revolution).

† The ELBEK contrast autofocus system uses the video signal from the camera to calculate the contrast on the image. This contrast value is available after every half image of the camera. Therefore the time between two contrast values is always 20 ms. To get the Z coordinate of the focus the system has to take the contrast values at different positions. Then the Z coordinate of the maximum contrast is expected to be the focus position. For this purpose the software of the autofocus first moves down the stage from the last position and then up with constant velocity through the old position to gather the contrast values. As the time between two contrast values is constant, the number of points depends on the number of steps below and above the old position and the speed of movement. The greather the interval for focus position search and the smaller the speed, the greather the number of points will be [74].

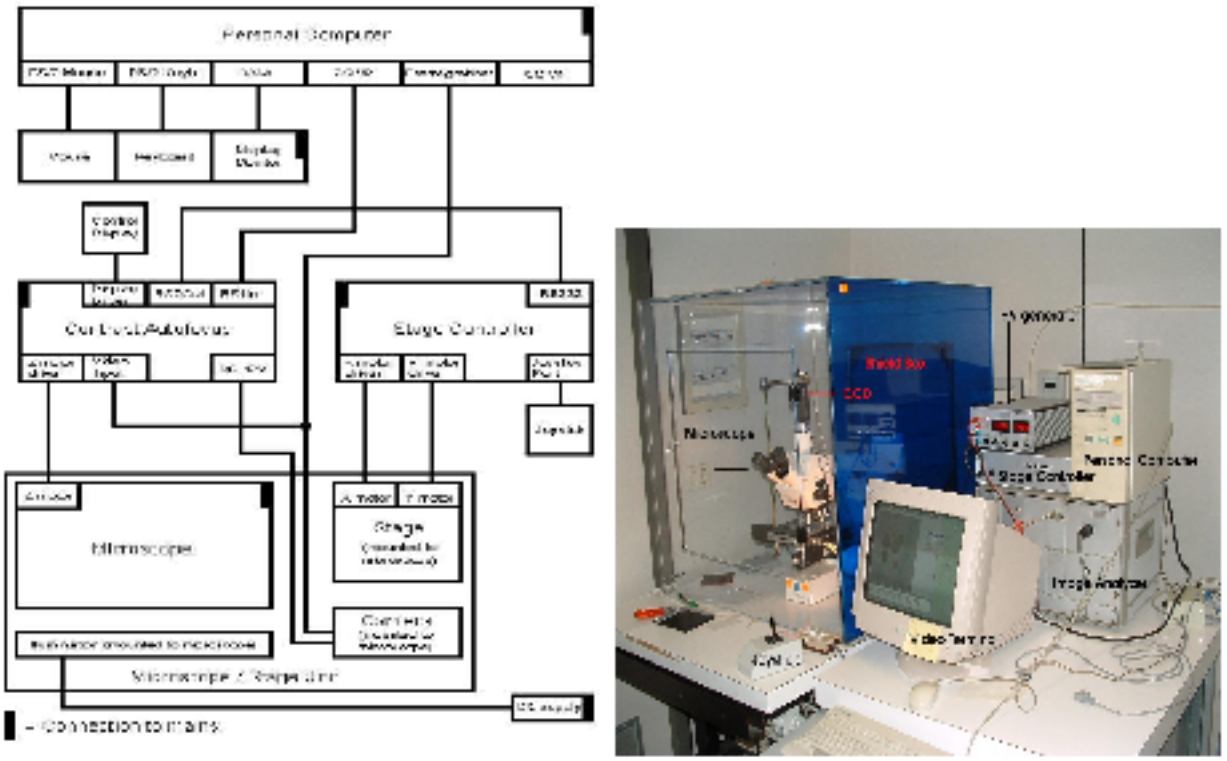

Figure 3.8: *Left:* Hardware configuration of the SAMAICA system. *Right:* Set up of the measuring system at the laboratory of the INFN Bologna.

The program SAMAICA has two main modules, the first is responsable for

the control purposes like file handling, stage movement and process control. The second module ICA (Image Contour Analysis) works on the images, and do the pattern recognition. To do this ICA has to extract elliptical objects and decompose overlapping objects in order to measured them separately. This procedure needs a parametrization of a lot of variables made by the user. These parameters are subdivided into: logic, contour, form, optimization, and cut parameters plus some special parameters used in the autofocus proceadure [5].

The ICA procedure search for objects in a pixel grid, and search for pixels with grey value lower than a limit fixed by the user in one variable, and with a contrast value greather or equal to another fixed value defined by the user (for the adjustment of this two parameters, one of the brightest object which are to be detected is taken as reference). Such pixels exist at the edge of focussed objects. The grey spectrum has to be well adjusted by the illumination and perhaps by the frame grabber reference parameters for the ADC. The lowest grey values should be close to 0 and range up to about 255 so that the 8 bit capacity of the digitizer is used but no underflow or overflow occurs [74]. The border between gray values lower and greather than the fixed value set in the parametrization, the edges of an object is found. The list of edge points is analyzed for convexity to detect overlapping or incomplete objects (this is made calculating the curvature). In the case of composed structure (overlapped objects), single contour is recomposed during another step of the image analysis, for further detaills see [74].

Evaluating the relative square deviation from a test circle, ICA classifies the contours into circullar and non-circular ones. This classification is done for stabilization of the fits of incomplete curves. If a well defined best fit ellipse exists (determinated by the elliptical deviation S2), then also a best fit circle will exist but not vice versa [74].

The data determinated for detected objects are:

- two center coordinates (u,v) in units of pixel lenght, measured respect to the center of the FOV
- semi minor axis (b) in units of pixel length
- ratio of semi minor to semi major axis (e)
- sine of the polar angle of the semi major axis (s)
- elliptical deviation (S2), zero if not fitted (s2)
- enclosed area (ea) in units of square pixel lenght

[5] In chapter 6 a detailled analysis of some of this parameter will be given

- central brightness grey value plus flags (f_cb).

These eight parameters are return by ICA for each detected object ans saved during automatic measurement together with image number.

Figure 3.9 shows the graphical display of SAMAICA during a scan session: the main square shows the microscope field of view (FOV); some of the displayed tracks are recognized by the system (their perimeter is marke with a green line) while others are neglected because of the scan parametrization.

The snapshot of the output display of the SAMAICA system (figure 3.9) shows the digitalized image of the detector, the auto focus parameters, the stage movement, and in the box at the bottom of the image are listed the variables read by the system.

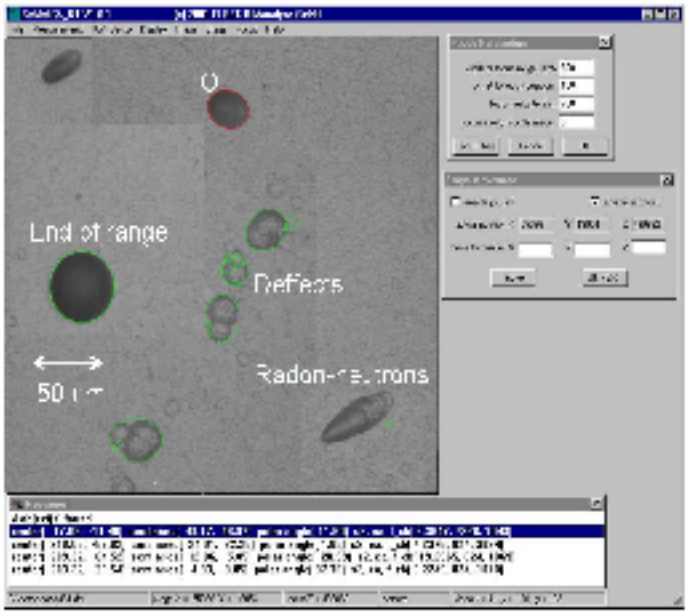

Figure 3.9: "Snapshot" of the SAMAICA display, showing some example signal detected by the system, *e.g* real Oxygen (O) tracks, a background track (radon or neutron track), and some defects (a chain of inhomogeneities, and a tracks of a particle that stops inside the bulk detector material, called end of range track).

3.3.1 Tracks Measured with SAMAICA

The Valid Track Candidates

The valid tracks have several typologies since CR have different charges and impinging angles. Tracks of highly charged ions are bigger than low charged ions, because

the REL release inside the detector is higher. Figure 3.10 shows micro-photographs of valid tracks candidates, each picture width correspond to 100 μm. The upper line micro-photographies corresponds to tracks on the top surface of the detector sheet; in the lower line are shown the "back-partner" tracks present on the bottom surface of the detector in correspondence to the each upper track; the images on the back were taken moving the microscope focus across the sheet. Tilted particles (with respect to the normal direction to the detector surface) impinging the detector with a higher zenithal angle form tracks with high ellipticity (ratio of the minor to major semi axes); tracks impinging the sheet vertically form circular tracks. Experimentally was found that the track brightness is a function of the zenith angle. Slightly inclined (almost circular) tracks are darker than elliptic tracks wich mirror back some of the microscope light impinging on the detector. In figure 3.10 are shown tracks passing through the detector with different impinging angles. More eliptic tracks appears lighter, than circular ones.

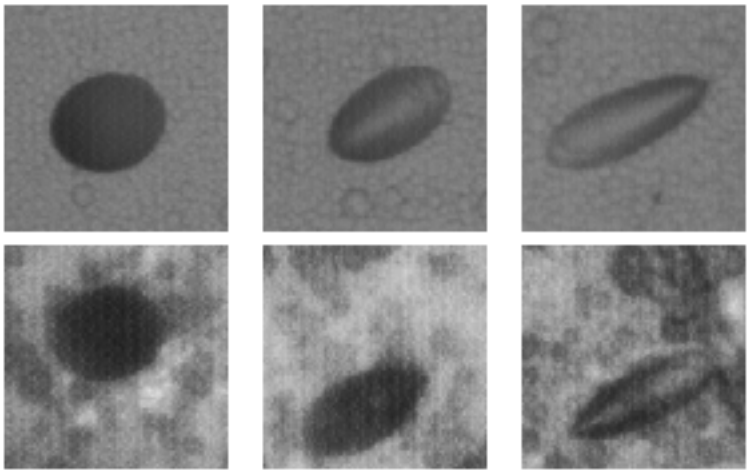

Figure 3.10: Different shapes of good tracks formed by CR ions. The top line show the pictures of the tracks on the front of the sheet; the corresponding lower line shows the pictures of the tracks seen on the back of the sheet. Each picture width correspond to 100 μm.

The background tracks

Sheet infomogeneities (such as scratches or bubbles) and tracks due to low energy particles (generally recoil protons, neutrons, and α-particles mostly from radom decay) contibutes to the background present on the detector sheets. Noise tracks are randomly distributed on th sheets surface. Figure 3.11 shows some example of noise introduced by the SAMAICA system when performs an automatic scan. On the left are shown detector defects miss-interpreted as tracks; at the center is

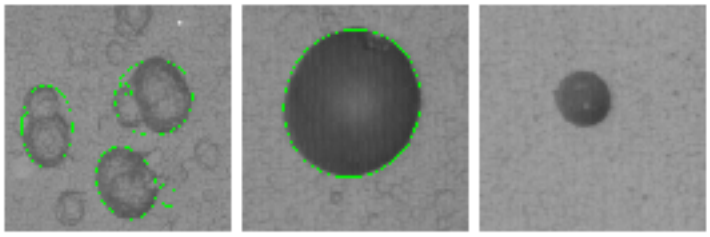

(a) (b) (c)

Figure 3.11: The main background tracks on CR39. (a) Bubbles from surface sheet defects. (b) Low energy particle track, mostly due to interactions of primariy neutrons with components of the material. (c) Track due to the pasage of a particle that release an increasing amount of energy inside the detector.

shown a micro-photography of track from a low energy particle, these kind of tracks correspond particles that slows down and stops inside the detector (these tracks are called End Of Range EOF tracks). In figure 3.11(a) the white spots slightly close to the center of the particle track indicate that the ion trajectory wer inclined, stopping after few microns inside the sheet.

Besides recognized good tracks and background there is an intermediate large category of tracks that looks like good tracks, but sometimes they do not cross the sheet. These kind of tracks are usually similar than real tracks, but with smaller dimensions; with a mean major axis smaller than about 30 μm [70]. Back-partners of such kind of tracks, when they exist, have different sizes with respect to the front-tracks, indicating that the particle release an increasing amount of energy inside the detector, figure 3.11(c) shows a micro-photography

Chapter 4

The SLIM Experiment

Figure 4.1: The Chacaltaya high altitude laboratory. The NTDs were placed on the roof of the buildings (at $\sim$ 4 m from the ground level), as shown in the photograph on the left corner of the composition. The geographical position of the lab. is 16°S 68°W, and is indicated on the right corner.

The SLIM experiment ("Search for LIght magnetic Monopoles") , was dedicated to the search for magnetic monopoles of intermediate masses (IMMs), aggregates of strange quark matter (strangelets, nuclearites) and supersymmetric dark matter candidates (Q-balls).

The layout was about 440 m^2 of nuclear track detectors, exposed for about 4 years at the *Laboratorio de Física Cósmica*[1], Chacaltaya, La Paz, Bolivia (16°S 68°W). The laboratory is located at an altitude of 5230 m a.s.l., at an atmospheric depth of to 540 g/cm^2.

[1] http://fcpn.umsa.bo/fcpn/app?service=page/Physics

The geomagnetic cut-off for cosmic rays at the detector latitude is $\sim 12.5\ GV$. Environmental conditions at the Chacaltaya lab are: atmospheric preassure ~ 0.5 atm; mean temperature $12°C$, oscillating from 0 to $30°C$; the radon concentration is $\sim 40 \div 50\ Bq/m^3$. The neutron flux in the range from few hundred keV to ~ 20 MeV is $1.8 \times 10^{-2}\ cm^{-2}s^{-1}$.

4.1 Accessible Regions for MMs and Nuclearites

The accessible regions in the plane mass *vs.* β_{min} for magnetic monopoles are plotted in figure 4.2 for poles of charge $g = g_D$, for detectors located at different altitudes. The velocity β_{min} is the minimun velocity at the top of the atmosphere that the particle has to have in order to reach at the detector. The curves correspond to detectors located at the underground LNGS[2], at a depth of 370 kg/cm^2, at an atmospheric depth of 540 g/cm^2, and at an altitude of 20 km.

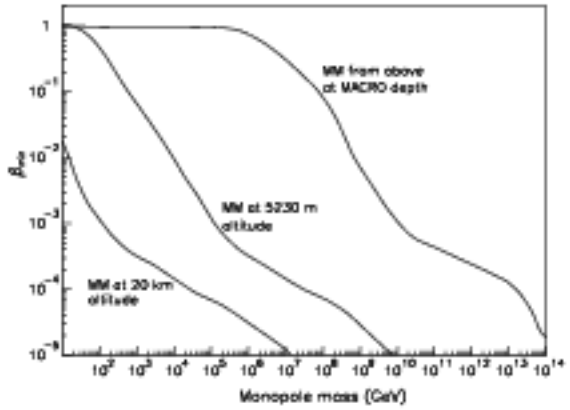

Figure 4.2: Accessible regions in the plane (mass, β) for monopoles with magnetic charge $g = g_D$ coming from above for experiments at altitudes of 20 km, at 5230 m a.s.l., and for an underground detector.

An important feature is that lighter monopoles can be detected at higher altitudes, that is the main motivation for deploying the SLIM experiment at the Chacaltaya altitude. For $\beta = 10^{-2}$ MMs as ligth as 10^5 GeV can be detected; the minimum mass for a MMs with the same velocity to reach the LNGS depth is $\sim 10^4$ times larger.

[2] www.lngs.infn.it

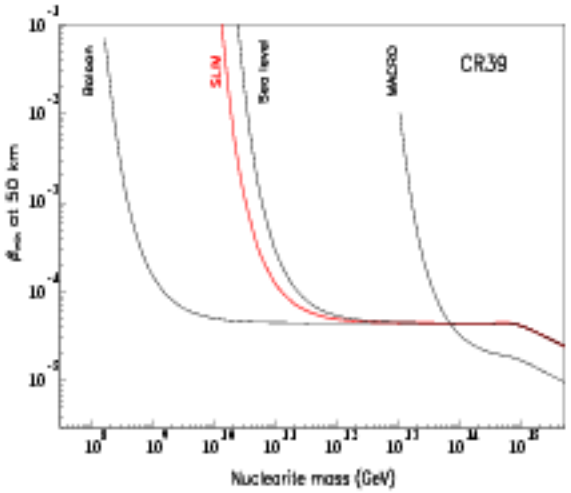

Figure 4.3: Nuclearite detection conditions in CR39 (solid curves) for experiments located at different locations [50].

Nuclearites of mass M entering the atmosphere with an initial velocity $v_0 << c$, after crossing a depth L will be slowed down to

$$v(L) = v_0 e^{-\frac{\sigma}{M}\int_0^L \rho dx} \tag{4.1}$$

where ρ is the air density, M is the mass of the nuclearite, and σ is the nuclearite-air cross section

$$\sigma = \begin{cases} \pi(3M/4\pi\rho_N)^{2/3} & \text{for} \quad M \geq 8.4 \times 10^{14} \quad GeV/c^2 \\ \pi \times 10^{-16}\, cm^2 & \text{for} \quad M < 8.4 \times 10^{14} \quad GeV/c^2 \end{cases} \tag{4.2}$$

with $\rho_N = 3.6 \times 10^{15}\, gcm^{-3}$. For $M = 8.4 \times 10^{14}$ GeV/c^2 the radius of the SQM is 10^{-8} cm.

Nuclearite detection conditions in CR39 and Makrofol, expressed as the minimum velocity at the top of the atmosphere (50 km) *vs.* nuclearite mass for different experimental locations are shown in figure 4.3. In this case, the constraint is that nuclearites have to have a minimun velocity at the detector level in order to produce a track. For $\beta = 10^{-2}$ nuclearites with masses $\sim 10^{10}$ GeV can be detected at the Chacaltaya lab; the minimum mass of nuclearites with the same velocity to reach the LNGS depth is $\sim 10^3$ times larger.

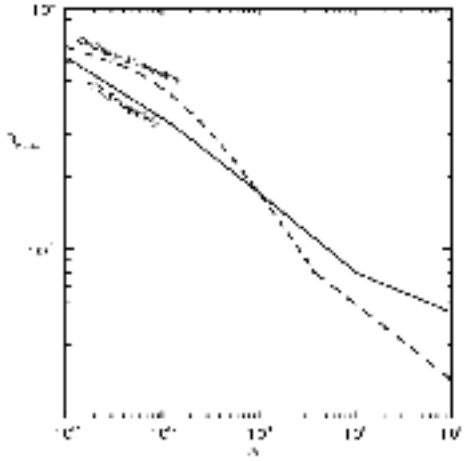

Figure 4.4: The minimum velocity for a strangelet at the top of the atmosphere, to be able to overcome the geomagnetic cut-off at the level of the SLIM detector. The red curve corresponds to CFL strangelets, and the blue curve to ordinary strangelets [58] (section 2.4)

For strangelets, assuming them to be electrically charged, one has to take into account the geomagnetic cut-off (sect. 1.6). The minimum velocity to overcome the effect of the geomagnetic field is

$$\beta_{min} = \sqrt{\frac{R^2}{R^2 + (\frac{A}{Ze})m_0c^2}} \tag{4.3}$$

where R is the maximun rigidity between $R_{cut-off}$ and R_{SM} due to the solar modulation, m_0c^2 is the nucleon mass.

For the particular case of strangelets (masses lower than $\sim 10^8$ GeV), using the charge-mass ratio for both strangelets types (ordinary and CFL), the minimun incident velocity at the top of the atmosphere to reach Chacaltaya is computed *vs.* strangelet mass (figure 4.4). Strangelets with baryon number smaller that $\sim 10^2$ have to have very high velocities in order to overcome the geomagnetic cut-off and reach the detector.

4.2 Energy Losses of MMs. Nuclearites. Strangelets and Q-balls

In the following the main features of MMs, nuclearites, strangelets and Q-balls energy losses relevant for their detection are described.

4.2.1 IMM Energy Losses

The interactions of IMMs with matter are related to the electromagnetic properties of the IMMs and are a consequence of the Dirac relation (section 2.2).

A "fast" IMM ($\beta > 10^{-2}$) with magnetic charge g_D and velocity $v = \beta c$ behaves like an equivalent electric charge $(ze)_{eq} = g_D\beta$ [39]; the energy losses of fast monopoles are thus large. There is the possibility that IMMs could be multiply charged, $g = 2g_D$, as in some SUSY theories, and $g = 3g_D$, as in some superstring models ($g_D = \hbar c/2e = 68.5\ e$ is the basic Dirac monopole charge) and the basic electric charge could be $1/3e$ [40].

The energy loss of "fast" IMMs can be calculated in the same way as for fast electrically charged particles, using the Bethe-Block formula. The energy loss of IMMs by ionization is

$$\left(\frac{dE}{dx}\right)_g = \left(\frac{ng_D\beta}{e}\right)^2 \left(\frac{dE}{dx}\right)_e \tag{4.4}$$

where $(\frac{dE}{dx})_e$ is the electric particle energy loss. For velocities in the range ($10^{-3} < \beta < 10^{-2}$), the MM energy loss is calculated by approximating the absorbing material of the detector with a degenerated gas of free electrons [41]. Ahlen and Kinoshita [42] developed a model considering the monopole interaction, for non conducting materials, obtaining

$$\frac{dE}{dx} = \frac{2\pi N_e g^2 e^2 \beta}{m_e c v_F}\left[\ln\frac{2m_e v_F \Lambda}{\hbar} - \frac{1}{2}\right] \tag{4.5}$$

where $v_F = \hbar/m_e(3\pi^2 N_e)^{1/3}$ is the Fermi velocity of the material, Λ is the mean free path. For non conductive materials Λ is equal to the Bohr's radius. In figure 4.5 (left) are shown the restricted energy losses for magnetic monopoles with different magnetic charges $g = g_D,\ 2g_D,\ 6g_D,\ 9g_D$.

4.2.2 Nuclearite Energy Losses

Large mass nuclearites can be treated as "meteorites"; elastic collisions with atoms and molecules of the traversed medium are their relevant energy loss mechanism.

$$\frac{dE}{dx} = -\sigma\rho v^2 \tag{4.6}$$

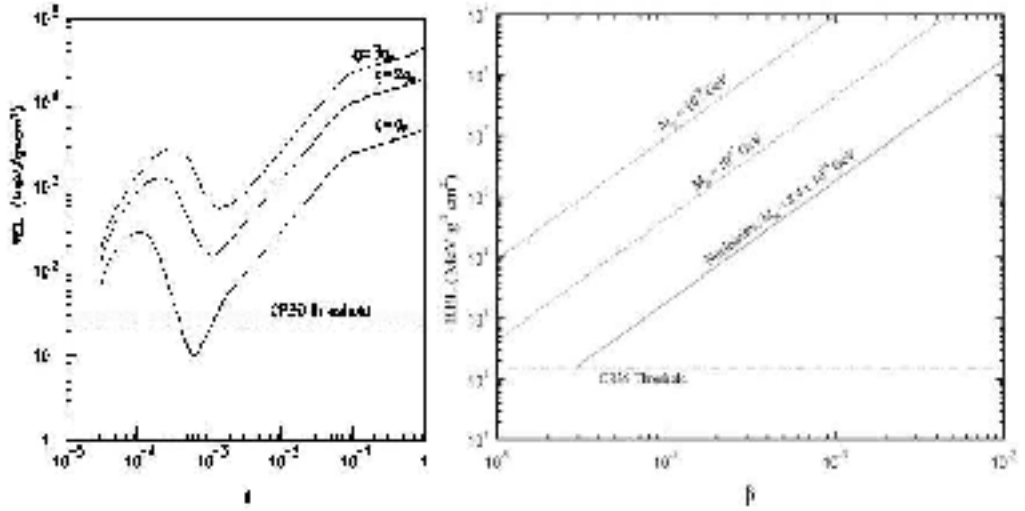

Figure 4.5: *Left:* Restricted energy losses *vs.* β, for MMs with different magnetic charges $g = g_D,\ 2g_D, \ldots$ [43]. *Right:* the Restricted Energy Loss of nuclearites of various masses in CR39 *vs.* their velocity. The threshold for CR39 in the SLIM experiment (strong etching) is also shown.

where ρ is the density of the medium, v is the nuclearite velocity, and σ is the cross section (equation (4.2)). Figure 4.5 (right) shows the energy loss for nuclearites of different masses.

4.2.3 Strangelet Energy Losses

The energy loss of low mass strangelets was computed as for any ordinary nucleus, taking into account the charge to mass relationship. At low velocities it was estimated from Ziegler's fit to the experimental data [55]. At higher energies the restricted energy loss of strangelets can be evaluated using the modified Bethe-Bloch formula. In figure 4.6 (*right*) it is shown the restricted energy losses of strangelets in CR39 of different electric charges.

4.2.4 Q-ball Energy Losses

The restricted energy loss of charged Q-balls, is similar to that of nuclearites and can be evaluated using the Bethe-Bloch formula, considering the contributions of ionization, and atomic recoil. In ref. [63] the calculations where made for SECS in CR39 nuclear track detector. Figure 4.6 (*right*) show the computed restricted energy loss for SECS with q = 1e and q = 13e plotted *vs.* β.

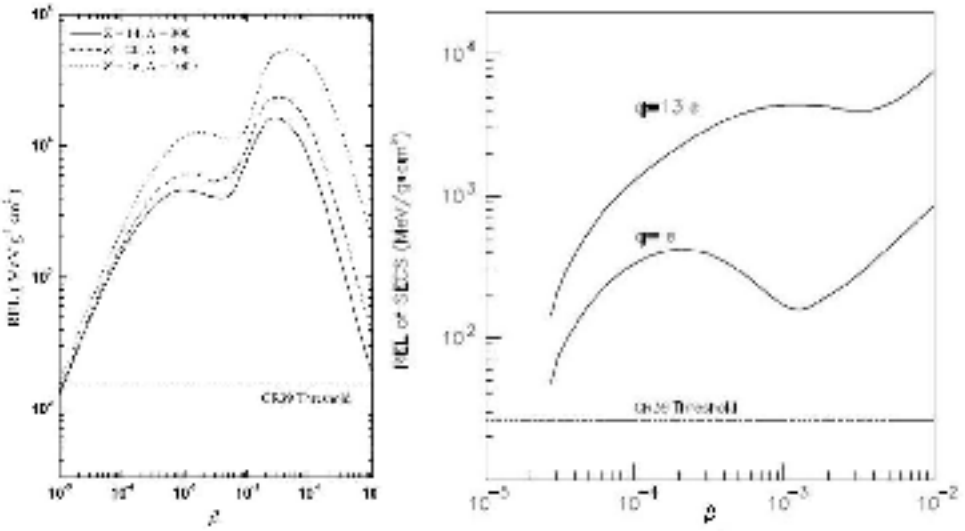

Figure 4.6: *Left:* Restricted Energy Loss *vs.* β for strangelets, in CR39. *Right:* Restricted Energy Losses of SECS with charges e and $13e$ *vs.* their velocity in CR39 [63].

4.3 The SLIM Experimental Layout

The total surface of SLIM was 440 m^2. The detector was organized in 7409 modules 24×24 cm^2 in size. The detectors used were CR39 foils with a mean thickness of 1450 μm, Makrofol foils with a mean thickness of 570 μm and Lexan of 450 μm thickness. Each module was made of three layers of CR39 (L1, L3 & L6), three layers of Makrofol (L2, L4 and L5), two protective sheets of Lexan (L0 & L7), and an aluminium absorver 1 mm thick used to stop or slow down nuclear recoils, the stack composition is sketched in figure 4.7. The stack was sealed in a mylar-aluminium bag 125 μm thick, filled with dry air at a preasure of 1 atm. The bag acts like a barrier to ambient radioactivity coming from ^{222}Rn. The thickness t of the components of the stack are: $t_{mylar-Al} = 0.032\ g/cm^2$, $t_{lexan} = 0.1096\ g/cm^2$, $t_{CR39} = 0.6019\ g/cm^2$, $t_{makrofol} = 0.2205\ g/cm^2$, and $t_{Al} = 0.27\ g/cm^2$. The total thickness of the stack is $t_{stack} = 1.23466\ g/cm^2$. The total height of one module was 8.37 mm, including

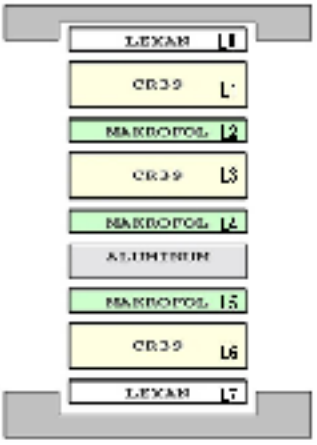

Figure 4.7: SLIM module composition.

the thickness of a film 50 μm thick that covers both sides of each detector foils. The film is removed just after the stack is opened, before the etching. A special batch of CR39 containing 0.1% of DOP additive was also used; the total surface covered with these detectors was $\sim$50 m^2.

4.4 Calibration of the Detectors

In order to calibrate the response of the SLIM NTDs, stacks of CR39 and Makrofol foils were exposed to beams of 158 A GeV of In^{49+} and Pb^{82+} ions at the CERN SPS and to 1AGeV Fe^{26+} ions at the BNL AGS.

In order to improve the quality of the surface of the detectors after etching, ethilic alcohol in different percentages was added to the chemical solution. Ethilic alcohol speeds up the rate of the removed bulk material, but it also increases the detection threshold.

Two etching conditions were used for the analysis of SLIM CR39: for the etching of the first CR39 layer, a condition called "strong" etching was applied. In the case of a candidate track the lower sheets of CR39 were etched using chemical conditions denoted as "soft etching". Was also used CR39 (DOP), was calibrated in both etching conditions.

In strong etching conditions, the bulk material is removed at a velocity $v_B = 7.8\ \mu m/h$. The thickness of the detectors is reduced from 1450 to 1000 μm. Using the soft etching conditions the velocity of the removed bulk material is lower ($v_B = 1.21\,\mu$)m/h. For soft etching the thresholds of CR39 is lower than for strong etching.

The chemical conditions used and the detection thresholds $(REL)_{min}$ and $(z/\beta)_{min}$ are listed in table 4.1.

	detector type	solution	Z/β	REL [MeVcm^2/g]
strong	CR39	8N KOH + 1.5% alcohol 70°C 30h	14	200
	CR39 DOP	8N KOH + 1.5 % alcohol 75°C 30h	19	240
	Makrofol	6N KOH + 20% alcohol 75°C 30h	50	2500
soft	CR39	6N NaOH + 1% alcohol 70°C 40h	7	50
	CR39 DOP	6N NaOH 70°C 40h	10	235

Table 4.1: Chemical etching condition used for the SLIM detectors; the threshold in z/β and restricted energy loss REL [Mevcm^2/g] are also indicated.

The "calibration plots" (in the plane REL *vs.* p) for CR39, obtained with both etching conditions are plotted in figure 4.8 for CR39 and CR39 (DOP).

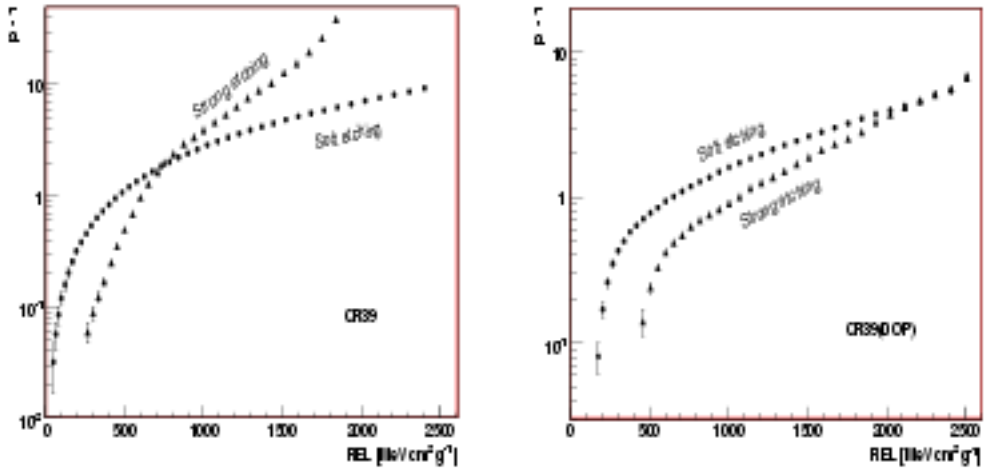

(a) Calibrations CR39 (b) Calibrations CR39 D.O.P.

Figure 4.8: Reduced etch rate $(p-1)$ *vs.* REL for strong and soft etching.

4.5 Analysis of the SLIM Nuclear Track Detectors

After the exposure 3 fiducial holes of 2 *mm* diameter, were drilled on each SLIM module with a position accuracy of 100 μm. The holes are used as reference points to align the detector folis.

Before etching the thickness of the layer is measured with 1 μm accuracy; detectors are etched in batches of 25 foils.

After the chemical etching, the L1 foil thickness is measured and the bulk velocity rate is computed.

4.5.1 Identification and Classification of the Etch-pit Tracks

Heavy particles like IMMs, nuclearites, strangelets and Q-balls are expected to leave in the detector module a constant REL. The post-etched track in L1 should correspond to "passing through-like" tracks of equal sizes in each detector foil when the same etching conditions are applied; the possible morphology of etch-pit tracks are sketched in figure 4.9.

"Fake tracks" can be originated by slowing down particles, nuclear recoils induced by cosmic ray neutrons, stopping particles inside the detector; surface inho-

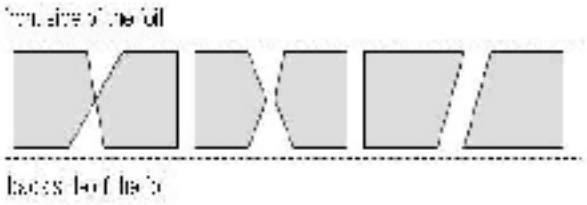

Figure 4.9: Possible morfology of different types of real tracks recorded in the detector.

mogeneities. Some fake tracks are sketched in figure 4.10.

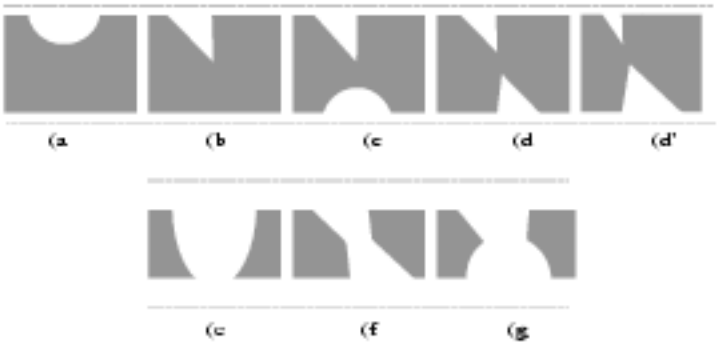

Figure 4.10: "Fake" etch-pit tracks that can be mis-identified as candidate tracks. Tracks (a), (b), and (e) are easy to discriminate; the other cases are more difficult to classify. In few cases the etching of additional layers may be required.

Candidate tracks were selected by comparing the size and the slopes of the etch-pits on the two sides (front and back). A first selection is made by requiring

$$\left|\frac{d_{front}}{d_{back}} - 1\right| \leq \Delta R \tag{4.7}$$

where ΔR is the overall uncertainty on the track dimensions; d_{front} and d_{back} are the track diameters on the front and back surfaces of the detector. L1 foils are observed using optical stereo microscopes at 8×magnification (0.8× objetive, and 10× eye piece). Any "particular" track detected in this first scan is further analyzed with an optical microscope at 200-400 × global magnification. In order to evaluate the p values and the incident angles θ for the front and back sides, the track minor and major axis are measured. A track is defined as a "candidate" if p and θ on the front and back sides are equal within 30%. For each candidate the azimuth

angle ε and position R refered to the fidual marks (drilled holes) are determined. The uncertainties $\Delta\theta$ and ΔR defines a "confidence" area ($< 0.5\text{cm}^2$) around the candidate expected position in the lower layers of the SLIM module, see figure 4.11.

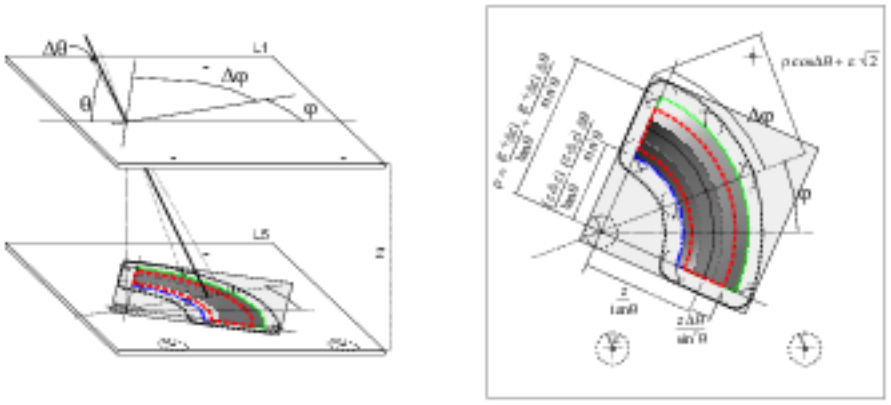

Figure 4.11: "Confidence" area in which a possible candidate track located on the top layer will be searched for in the lower layer of the same module.

The lowermost CR39 layer (etched in the "soft" conditions) was scanned using a high magnification microscope of 500× or 100× of global magnification in a squared region around the candidate expected position, which includes the "confidence" area. If a two-fold coincidence track was detected all geometrical parameters are measured; the middle CR39 layer would also be analyzed using the same proceadure.

4.6 Acceptance of the Detector

The acceptance of the SLIM detector to a isotropic flux of particles coming from above is given by

$$S\Omega = \pi S \int_0^{\delta_c} \cos\delta \sin\ \delta d\delta = \pi S\ (1 - \cos 2\delta_c) \tag{4.8}$$

where S is the surface of the detector and $\delta_c = 90 - \theta_c$, where θ_c is the "critical angle" of detection, defined in 3.1.4. By using the relation (3.11) and (4.8), the geometrical acceptance is

$$S\Omega = \pi S\ (1 - \cos^2\delta_c) = \pi S\ (1 - \frac{1}{p^2}) \tag{4.9}$$

In figure 4.12 is shown the global acceptance of the CR39 SLIM detector to MM with g_D (black), $2g_D$ (red), $3g_D$ (green), to Dyons (blue) as a function of β computed for the strong etching conditions

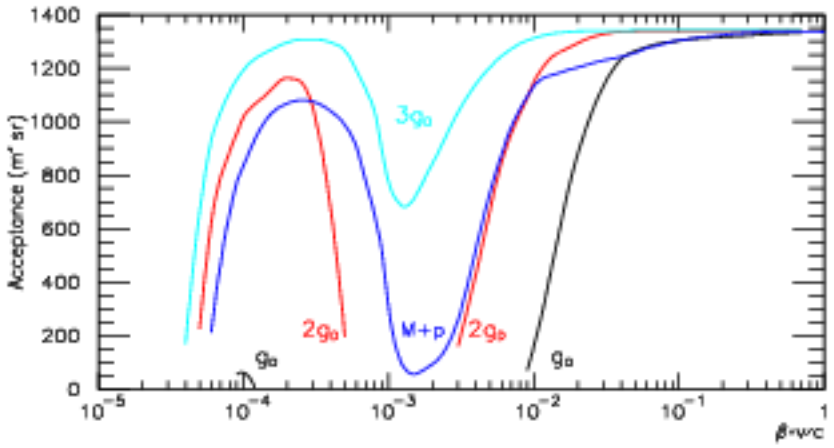

Figure 4.12: Acceptances of the SLIM detector (CR39) for magnetic monoples with charges g_D, $2g_D$, $3g_D$ and $M+p$ (dyons).

4.7 Upper Flux Limits

Since no candidates were found the 90% C.L. upper limits for downgoing particles was computed as

$$\phi = \frac{2.3}{(S\Omega)\epsilon\Delta t} \tag{4.10}$$

where Δt is the mean exposure time equal to 4.22 years, $S\Omega$ is the total acceptance ($S = 427\ \mathrm{m}^2$), ϵ is the scanning efficiency estimated $\sim$1.

The global 90% C.L. upper limits for the flux of downgoing IMMs and dyons with velocities $\beta > 4 \times 10^{-5}$ were computed, as shown in figure 4.13. The flux limit for $\beta > 0.03$ is [67]

$$\Phi \leq 1.3 \times 10^{-15}\ cm^{-2} sr^{-1} s^{-1}$$

The 90% C.L. upper flux limmits for downgoing nuclearites and Q-balls is at the same level, as for fast magnetic monopoles

$$\Phi \leq 1.3 \times 10^{-15}\ cm^{-2} sr^{-1} s^{-1}, \qquad \text{for } \beta > 10^{-4}$$

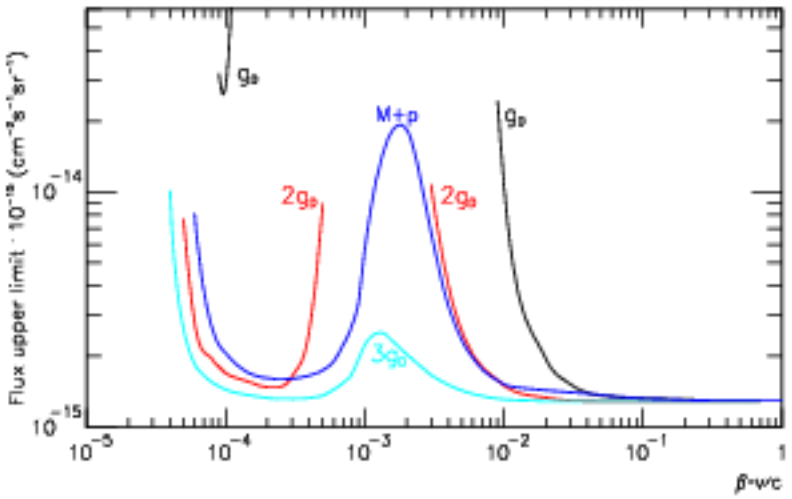

Figure 4.13: Final results of the SLIM experiment: upper flux limit for magnetic monopoles with charges g_D, $2g_D$, $3g_D$ and $M + p$.

Chapter 5

Study of the Neutron Induced Background in SLIM

5.1 Introduction

At the Chacaltaya altitude primary neutron in the CR can interact in NTDs. Charged secondaries particles can be detected if their energy loss is above the detector threshold. Such particles contribute to the background in searches for rare particles, as MMs, or nuclearites. In my study I have examined mainly the background generated by neutrons on the first layer of CR39 of the SLIM stacks using Monte Carlo (MC) simulations. Neutrons at the altitude of the SLIM location could have different origins; here we are focused on neutrons due to primary cosmic ray interactions with the atmosphere. The neutron spectrum at the SLIM site were measured by [75] with different systems which allows to reconstruct the neutron spectrum in the atmosphere in the range 100 keV to 400 GeV. The measured spectrum is shown in the double logarithmic plot in figure 5.1; as the intensity times the energy of the neutrons *vs.* their energy.

5.2 Neutron interactions

Because neutrons have no electric charge, they interact with nuclei via the strong force, and are usually detected via nuclear reaction products; because of the short range of the strong interaction these reactions are much rarer than electromagnetic ones. Neutrons must come within $\sim 10^{-13}$ cm of the nucleus before any interaction take place. The interactions undergo in a variety of nuclear processes depending on the energy [72]:

Elastic scattering from nuclei, i.e. $A(n,n)A$. This is the principal mechanism of energy loss for neutrons in the MeV region.

Inelastic scattering, e.g. $A(n,n')A^*$, $A(n,2n')B$, etc. In this reaction, the nucleus

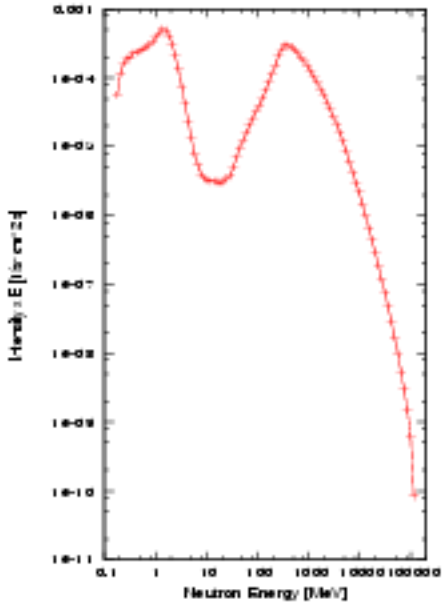

Figure 5.1: Wide range spectrometer: experimental neutron spectrum measured at Chacaltaya laboratory (5230 m a.s.l., 16°S 68°W), Zanini et al. [75].

is left in an excited state which may later decay by gamma-ray or some other form of radiative emission. In order for the inelastic reaction to occur, neutrons must have sufficient energy to excite the nucleus, usually on the order of 1 MeV or more. Below this energy threshold, only elastic scattering may occur.
Radiative neutron capture, *i.e.* $n + (Z, A) \rightarrow \gamma + (Z, A + 1)$. In general, the cross-section for neutron capture goes approximately as $\sim 1/v$ where v is the velocity of the neutron. Absorption is more likely, therefore, at low energies.
Other nuclear reactions, such as (n,p), (n,d), (n,α), (n,t), $(n,\alpha p)$, etc. in which the neutron is captured and charged particles are emitted. These generally occur in the eV to keV region.
Fission, *i.e.* (n, f), most likely at thermal energies.
High energy hadron shower production, which occurs only for neutrons of very high energy, $E > 100\ MeV$.

5.3 Monte Carlo Simulations

A dedicated C++ software was implemented to study the interaction of neutrons in CR39. The code is written in the framework of the Geant4 toolkit [79]. The version used here is Geant4.8.2 running in a Scientific Linux 4.1 platform. Geant is the name of a series of object oriented C++ simulation software designed to describe the passage of elementary particles through matter, using Monte Carlo (MC)

methods. The name is from "GEometry ANd Tracking". Geant4 includes facilities for handling geometry, tracking, detector response, run management, visualization and user interface. Geant4 runs using specific classes from the CLHEP library of high energy physics; in this thesis the version CLHEP 2.0.3.1 was used. Generated data were analyzed with the object-oriented data analysis framework ROOT (http://root.cern.ch/) .

5.4 Detector Construction

For the Monte Carlo simulation only the first layer of CR39 of the SLIM stack was considered (see figure 4.7). The CR39 polymer is defined in the simulation by its chemical formula, $(C_{12}H_{18}O_7)_n$, and other physical properties *e.g.* the density $\rho = 1.31\ g/cm^3$.

The detector geometry consists in a parallelogram of 1 cm $\times$ 1 cm, with a thickness of 1450 μm being this the mean thick value of the CR39 detectors used in SLIM. The detector is divided in an arbitrary number of slices each one of the same thickness; each slice is divided in an arbitrary number of vertical and horizontal sectors, defining tridimensional cells forming a grid. The subdivision is made in order to gain accuracy in the determination of the energy release by the different particles, both for primaries and secondaries passing through the detector, figure 5.4. Downstream the detector a slice of sensitive detector is added in order to record the passage of outgoing particles; this element is called the "outgoing sensor" (OS); the OS is plotted as a blue parallelogram in figure 5.4.

The CR39 sheet is surrounded by a parallelogram that represents the boundaries of the SLIM stack. All the array is surrounded by an external region called "the world" (represented in figure 5.4 by a gray box), which defines the boundaries of the simulation. The world is defined as a box of 3×3 cm^2, and 0.5 cm thick.

The absolute reference system is left handed, with the origin at the center of the detector, and the the Z axis perpendicular to the detector surface. Neutrons are assumed to move along Z.

Physical Processes

The processes implemented for the neutron interactions in CR39 and for secondary particles are listed in the appendix A.

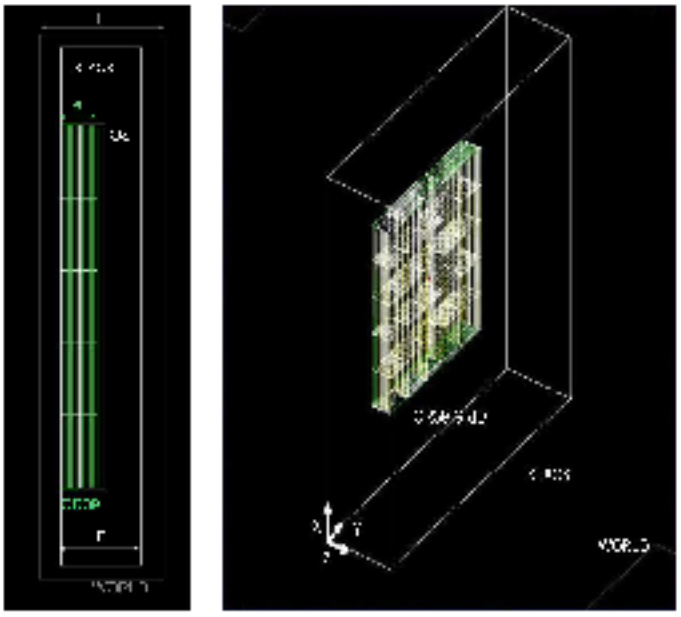

Figure 5.2: Detector geometry. ***Left:*** The detector material is CR39, with dimensions of 1 cm × 1 cm × a thickness of 1450 μm denoted by e in the figure. The detector is subdivided in an arbitrary number of slices which are divided in cells, represented in the figure by green boxes. The blue parallelogram after the CR39 sheet is the "outgoing sensor" OS, and is a piece of CR39 that records the passage of the outgoing particles. The white parallelogram represents the stack with thickness $E = 1$ cm, and is filled with air at 1 atm of pressure. The gray parallelogram surrounding the detector (world) limits the boundary of the simulation. The sketch plotted here is not on scale. The beam direction is perpendicular to the detector surface, along the Z axis. ***Right:*** 45° view of the geometry of the simulation, showing the detector, the stack, and the world. The system of reference is located at the center of the detector.

5.5 The Monte Carlo Software Architecture

The code is organized in a main program, mandatory classes, custom classes, and a class that manage the graphical visualization called VisManager(). The UML (Unified Modeling Language) scheme 5.3 sketches the structure of the software.

In Geant4, Run is the largest unit of simulation, implemented in the class RunAction. A run consists of a sequence of events. Within a run, the detector geometry, the set up of sensitive detectors, and the physics processes used in the simulation should be kept unchanged. A run is represented by a G4Run class object. In the Main(), are initialized several objects with which all the steps of the simulation are

made. The code make the simulation event per event. The mandatory classes are, a

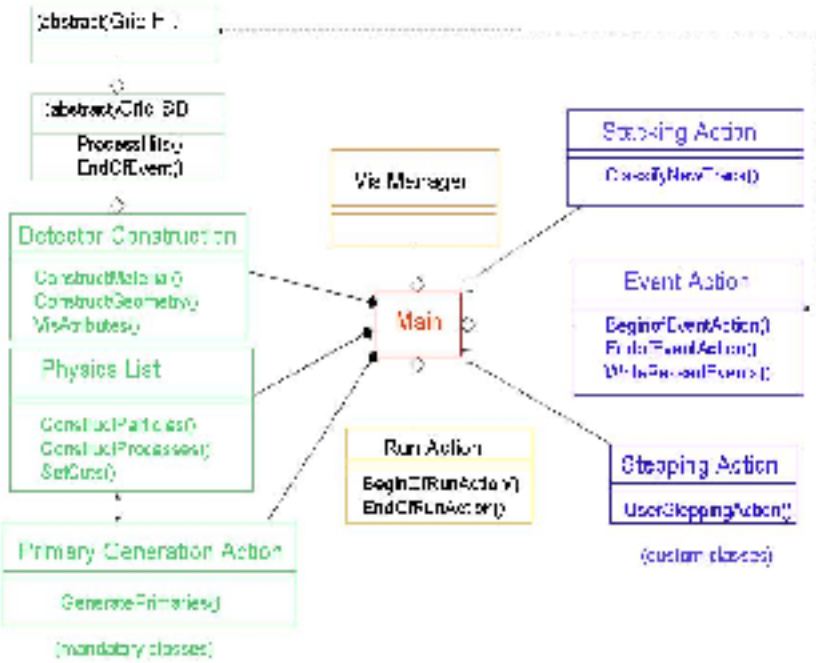

Figure 5.3: UML diagram of the software implemented for the Monte Carlo simulation. The mandatory classes which defines the "experimental layout" are written with green characters; the custum classess which manages the interactions are written with blue characters. The class visManager manages the visual interface of the simulation runs.

class where the material and the geometry of the detector are defined as explained in section 5.4 (in the diagram denote by DetectorConstruction); a class were are instantiated the channels that describe the interactions, as detailed in section 5.4 (in the diagram denoted by PhysicsList); finally a class that initializes the physical characteristics of the primary neutrons *e.g.* its energy, and momentum direction, its incident direction and position (in the diagram denoted by PrimaryGeneration-Action).

The custom classes are, EventAction() which objects are the primary units of a simulation run [78]. An object of this class contains all inputs and outputs of the simulated event; this class manage the interaction of primaries, determining the quantity of energy released on a cell of the detector grid for each interaction (called hit). Figure 5.4 shows the energy deposit inside a cell. The class StackingAction() manages the information of the secondaries produced in each hit. The SteppingAction() class plays an essential role in particle tracking. It performs message

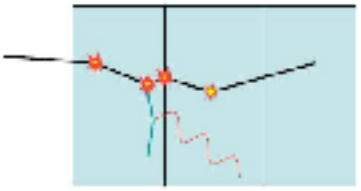

Figure 5.4: Energy deposition inside a cell. For each interaction the energy loss is evaluated; the total energy loss inside a cell is computed.

passing to objects in all categories related to particle transport, such as geometry and physics processes.

5.6 Output of the Monte Carlo Simulation

The graphic output of MC shows the experimental set up (*i.e.* the detector, the stack and the world), the primary neutron beam, the interaction points and the trajectories of the generated secondary particles. An example is shown in figures 5.5, for the interaction of 10 MeV neutrons in CR39. Particle trajectories are drawn with different colors according to their charge: red lines for negative particles, for positive particles a blue line, and neutral particles are represented by green lines.

Output data is recorded in 3 ROOT-files [1], one for the primaries; another for each type of secondary particles; and a third file contains the information about neutrons exiting the detector. For the primaries the energy deposited on each interaction, the coordinates where the interaction occurs, the components of its momentum, and the polar angle (angle between the z-axis and the direction of the particle) are saved. As well as the mean values per cell of the same variables.

For each type of secondary generated inside the CR39, the energy deposited on the detector, the coordinates where the particle was generated, the type of process by which it was generated, the momentum, and polar angle are saved.

By using the above the trajectories of the primaries and secondories can be reconstructed; as well as the interaction points. Figure 5.6 (left) shows interaction points of primary neutrons of 10 MeV interacting in CR39. In figure 5.6 (right) are plotted the coordinates where secondaries are generated. Blue dots indicates positively charged particles, red dots negative particles, and green dots correspond to neutral particles. The figure shows that most of the secondaries are generated along the beam direction.

[1] A ROOT file is like a UNIX file directory. It can contain directories and objects organized in unlimited number of levels. It also is stored in machine independent format http://root.cern.ch/root/doc/RootDoc.html

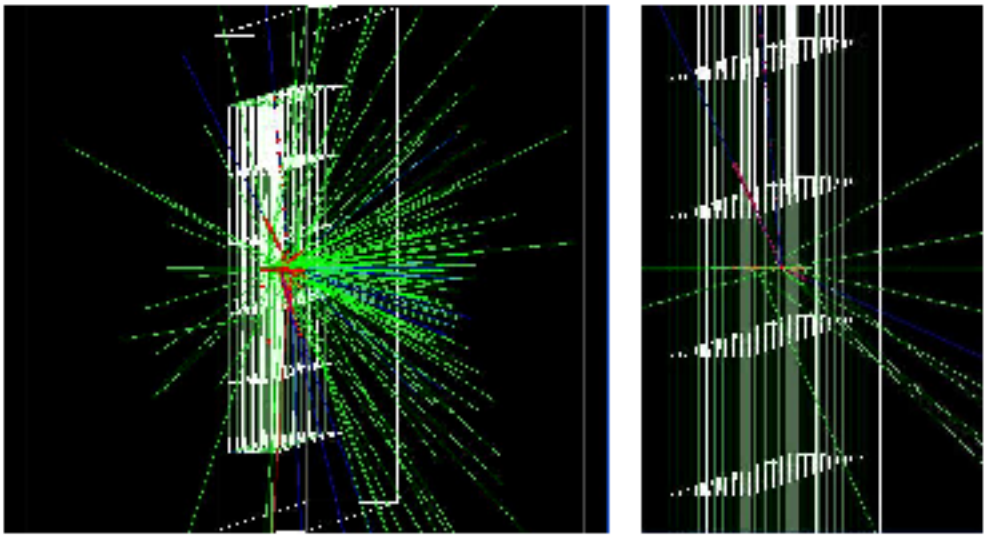

Figure 5.5: *Left:* Graphical output of the MC simulation. The lines represent particle trajectories: green lines represent neutral particles, red lines represent negatively charged particles, and with blue lines are plotted the trajectories of positive particles. The red dots represent interaction points *e.g.* decays, collisions, energy deposition, secondary production, etc. *Right:* Detailed view of the detector showing the trajectory splitting caused by different type of interactions.

Figure 5.7(a) shows the profile of primary interaction positions (left) and the radial distrubions with respect to the beam direction, for 10 MeV neutrons impinging perpendicularly to CR39.

5.7 Cross Checks of the SLIM Monte Carlo

The results obtained with the simulation I performed (SLIM Monte Carlo) are compared to those obtained by another MC pavkages commonly used in neutron physics, the MCNPX [2] (Monte Carlo N-Particle eXtended) which is a general-purpose MC radiation transport code.

The cross check consists on the simulation of neutron processes using fixed experimental conditions. The model consists in the simulation of the proton (p) with fixed energies interacting with a thick alluminium (Al) target, and tracking the secondary neutrons produced inside the target. The energy of the primary p ranges in the MeV region. The experimental set-up consists of a proton beam inpinging on a $3\times3\times3$ cm^3 Al target which is divided in cells, forming a tri-dimensional grid. The experimental layout is shown in figure 5.8. For the simulation 10^6 primary

[2] http://mcnpx.lanl.gov/

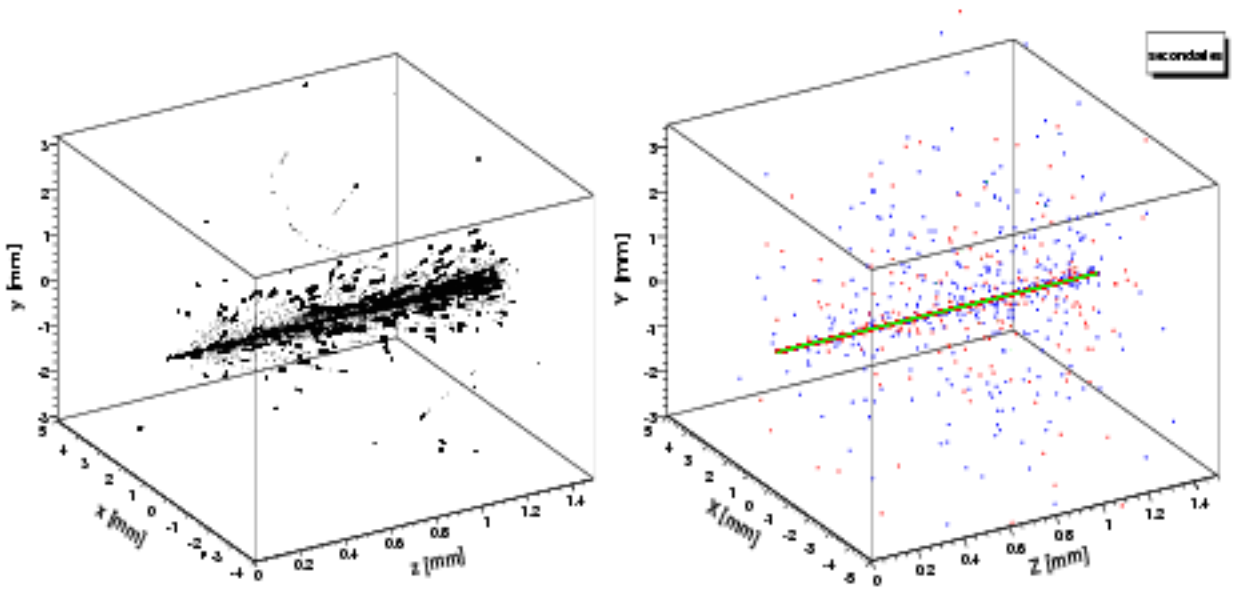

Figure 5.6: *Left:* Interaction points of 10 MeV primary neutrons inside a CR39 sheet. The incident neutron direction is along the z-axis; the trajectory spread is due to interactions inside the material *e.g.* elastic and inelastic scattering. *Right:* production points for secondaries: red dots are used for negative charged particles, blue dots for positively charged particles, and green for neutral particles.

protons with energy from 30 MeV to 150 MeV were considered. Out of all secondary neutrons only those in the forward direction are selected. The comparison with MCNPX is made by taking into account only neutrons produced in the (p,n) nuclear reactions. The relative abundances of neutrons (defined as the number of secondary neutrons over the total number of secondaries) with forward direction produced in (p,n) processes, obtained using the SLIM MC and the MCNPX are plotted in figure 5.9 (left). Differences are within the $\sim$20% up to energies of $\sim$90 MeV; at higher energies the relative abudances differ by $\sim$36%. The total energy release by neutrons leaving the target was also evaluated. The results are plotted in figure 5.9 right. The differences for energies from 30 up to 100 MeV are within $\sim$21%; at energies in the 100-150 MeV range the difference rises to $\sim$38%. The agreement is satisfactory up to energies of $\sim$80 MeV. MCNPX uses the neutron library LA150N which extend the range from 20-150 MeV, except for some ions which energy range goes up to 100 MeV. This library typically extends ENDF/B-VI data for the range 20-150 MeV.

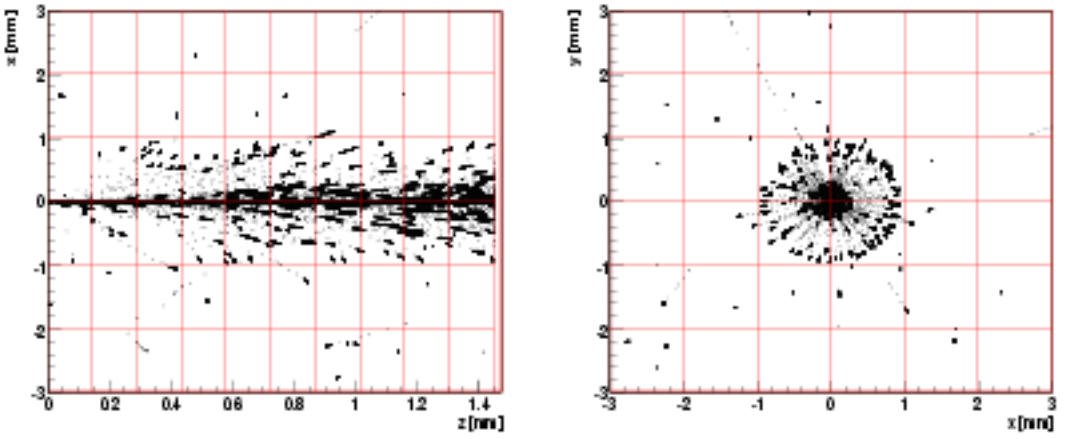

(a) Profile view of the sensitive detector along the beam axis (z-axis)

(b) Front view of the detector (x-y plane)

Figure 5.7: Example of the interaction of primary neutrons of 10 MeV in CR39. The balck marks represents the points were interacctions occurred; the subdivision of the detector is shown by red lines.

5.8 Simulations of Neutron Interaction in CR39

A CR39 sheet of 1 cm $\times$ 1 cm $\times$ 1450 μm was used as a target. For the simulations a primary neutron beam (10^5 neutrons) of definite energy was considered.

The energy of the neutrons is sampled from a wide range, in order to study all the possible mechanisms of secondary production; the energy is sampled in a wide range, taken the following values: 100 keV, 500 keV, 1MeV, 10 MeV, 5 MeV, 15 MeV, 20 MeV, 30 MeV, 50 MeV, 100 MeV, 1 GeV, 10 GeV.

The results are expressed as "relative abundances" defined as the ratio between the number of secondary particles of one type over the total number of secondary particles generated. The most abundant elements produced inside the CR39 are found to be protons, followed by isotopes ^{12}C and ^{16}O, figure 5.10, then γ-particles and secondary neutrons, figure 5.11.

In the interactions α-particles, electrons, and also Carbon isotopes (different of ^{12}C) denoted by C^*, Beryllium (Be^*) are produced. Isotopes of Boron, Nitrogen, Lithium, Oxygen (different to O^{16}), Hydrogen and Helium are also produced, but with relative abundances smaller than 1%. The same relative abundances are found for π particles (π^0, $\pi^{\pm}$), and positrons e^+.

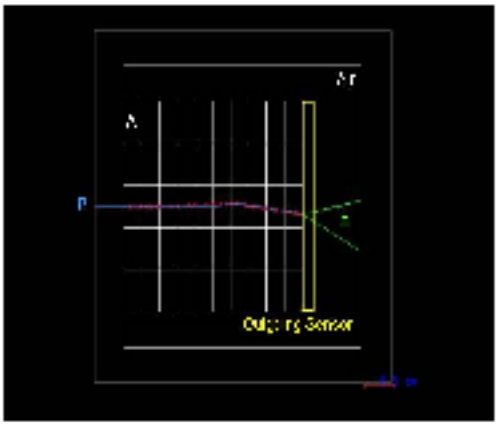

Figure 5.8: Layout of the simulation of a beam of protons of fixed energy interacting in a thick Al target of $3\times3\times3$ cm^3. The sensitive detector (Al box) is divided in a 3 dimensional grid represented by white boxes; the yellow parallellogram is the "outgoing sensor". The blue line indicates the direction of the incident proton beam; red dots represent interaction points and the green lines are the trajectories of neutrons generated inside the target.

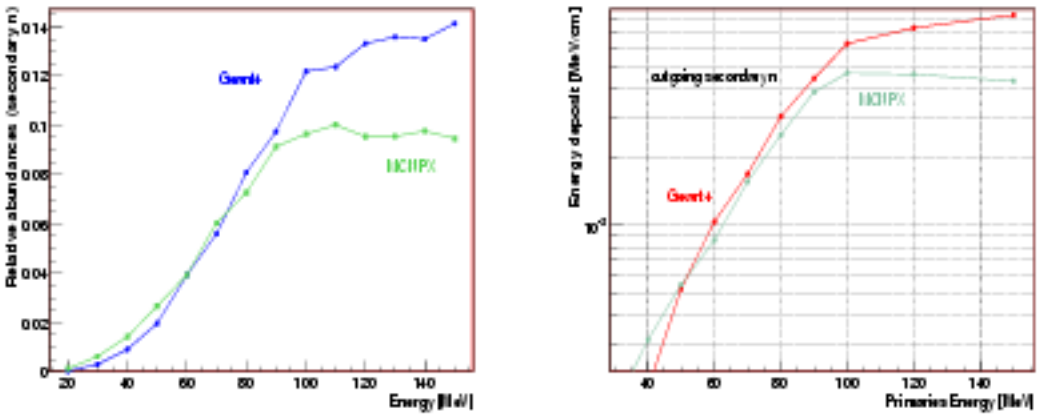

Figure 5.9: *Left:* Relative abundances of the secondary neutrons in the forward direction produced in the nuclear reaction (p,n) obtained with the SLIM MC (blue curve) and the MCNPX code (green line) respectively. *Right:* energy deposited by the secondary neutrons in the downstream surface by primary protons. In red the values obtained with SLIM MC, and in green are the results obtained with MCNPX.

In table 5.8 are listed the most abundant secondary particles; in the second column is indicated the minimum energy of primary neutrons for the cases when secondary particles to be produced.

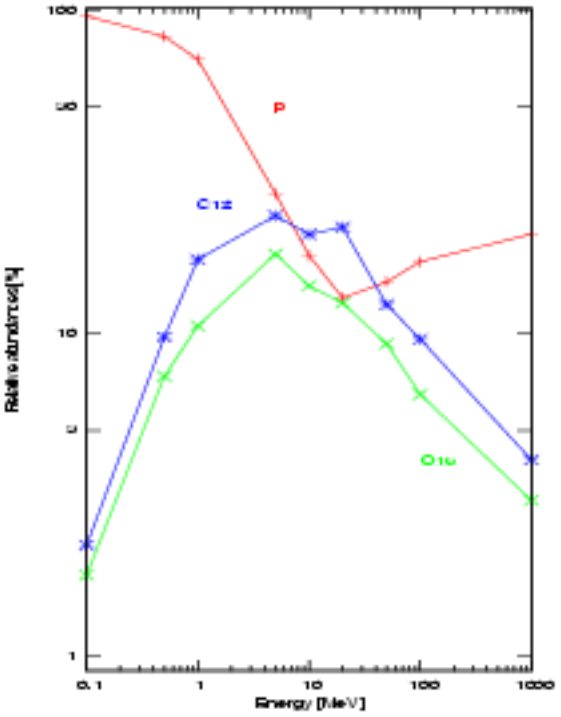

Figure 5.10: Relative abundances of the most abundant elements *i.e.* protons, and isotopes ^{12}C and ^{16}O produced inside CR39 plotted *vs.* the primary neutron energy.

A more detailled study for the production inside CR39 of secondary particles was made in the MeV region. Relative abundances are plotted in figure 5.12 for the energy range $1 \div 50$ MeV. From the results of the simulation for the production of secondary particles and from the total cross sections of neutrons, some comments can be made about the main nuclear reactions.

In CR39 neutrons undergo *elastic scattering* with the constituent elements of the detector (mostly H, C, O). The high H content, about the 50% in mass and the high cross section (15000 mb at 0.1 MeV and 1000 mb at 8 MeV) makes the reaction $H(n,n)$ the most significant one. By-product of this reaction are recoiling protons which contribute to the track density after etching [68]. This is confirmed by plots in figure 5.10.

Neutrons undergo also *elastic scattering* with carbon $C(n,n)$, and oxygen $O(n,n)$; ^{12}C, and ^{16}O isotopes are then produced [82]. Figure 5.10 shows that the relative abundances of ^{12}C, and ^{16}O increase up to $\sim 30\%$ for ^{12}C and $\sim 25\%$ for ^{16}O around $5 \div 20$ MeV, then both decrease (see figure 5.12(a)). Experimental measurements of abundances of neutrons inside CR39 made by [81] indicates that direct carbon and oxygen recoil tracks (from elastic collisions) are detectable if the energy

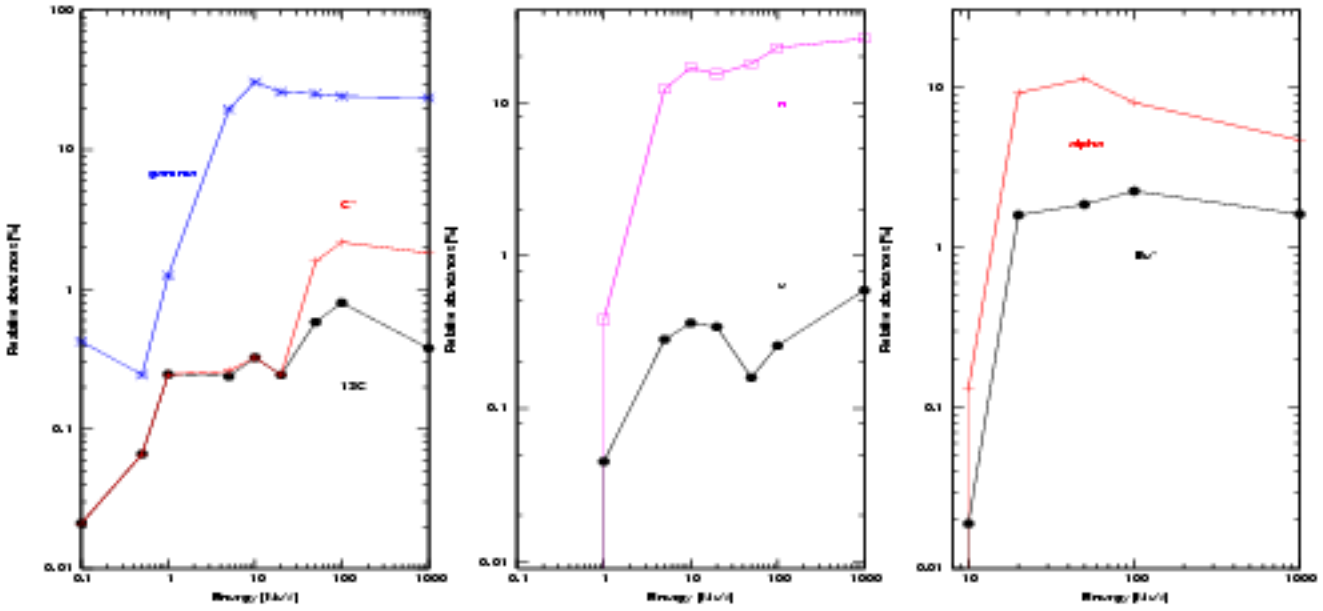

Figure 5.11: Relative abundances of γ particles, α particles, electrons, neutrons, and isotopes of carbon and beryllium produced in the interaction of neutrons with CR39 *vs* the primary neutron energy in the MeV region.

of the neutron is higher than 5 MeV, and that for energies larger than 20 MeV then abundances are depleted.

In figure 5.10 the abundances of the isotopes of C and O are plotted. Up to energies of $\sim$10 MeV protons are much more abundant than C and O nuclei; around $10 \div 20$ MeV the abundances are comparable, ^{12}C abundance is larger than p in the range $10 \div 40$ MeV.

Neutrons interact *via inelastic scattering* with carbon $C(n,n')C^*$ and oxygen $O(n,n')O^*$. In this reaction the nucleus is left in an excited state, and may later decay by gamma-ray (γ) or some other form of radiative emission. The inelastic reaction occurs only if neutrons have enough energy to excite the nucleus, usually at 1 MeV or higher. Below this threshold, only elastic scattering may occur [72]. In figure 5.11 left the relative abundances of γ-particles rapidly increases for energies larger than $\sim$ 1 MeV. Other by-products of this reactions are carbon and oxygen ions. Other types of inelastic scattering processes also occur. For example in the reactions $^{12}_{6}C(n,n')$, $^{16}_{8}O(n,n')$ secondary neutrons are produced inside CR39. This process has a threshold around 5 MeV [81]. Figure 5.11 (middle) shows the production of secondary neutrons obtained with the MC simulations, with a production threshold of 1 MeV; the relative abundances rise around 5 MeV, as shown in figure 5.12(b).

Element	Energy threshold
p	100 keV
C^{12}	100 keV
O^{16}	100 keV
γ	100 keV
C^*	100 keV
n	1 MeV
e	1 MeV
α	10 MeV
Be^*	10 MeV
e^+	10 MeV
N^*	20 MeV
B^*	20 MeV
H^*	20 MeV
H^2	20 MeV†
H^3	50 MeV†
He^*	50 MeV
Li^*	50 MeV
π	1 GeV

Table 5.1: Production threshold of the different species, the energy value correspond to the energy of the primary neutrons at which the secondary type starts to be produced. The value 100 keV is the minimum value used in the simulations and it is not neccesary the production threshold. † are Hydrogen isotopes, deuterium (H^2) and tritium (H^3).

Different alpha reactions (n,α) can occur in the MeV region where α-particles are produced; the main reactions are: $^{12}C(n,n3\alpha)$ called the three alpha-process having a cross section of $\sim$ 360 mb at 15 MeV [81]. MC results for α-particles are plotted in figure 5.11 (right), showing an energy production threshold at 10 MeV; around 20 MeV a fast increase of their abundance occurs, of the order of 10%. Another alpha reaction is $^{12}C(n,n'\alpha)^9Be$ by which both α particles and beryllium isotopes are produced, the cross section for this reaction is $\sim$ 50 mb above 8 MeV [81]. The relative abundances of the Be isotope, shown figure 5.11 (right) behave as for α-particles. The production energy threshold is 10 MeV; at 20 MeV an increase of $\sim$ 100% in the relative abundances can occur.

Carbon isotopes ^{13}C and α particles can be produced via the $^{16}O(n,\alpha)^{13}C$ reaction. The cross section for this process is $\sim$ 1000 mb around 10 MeV [81]. Figure

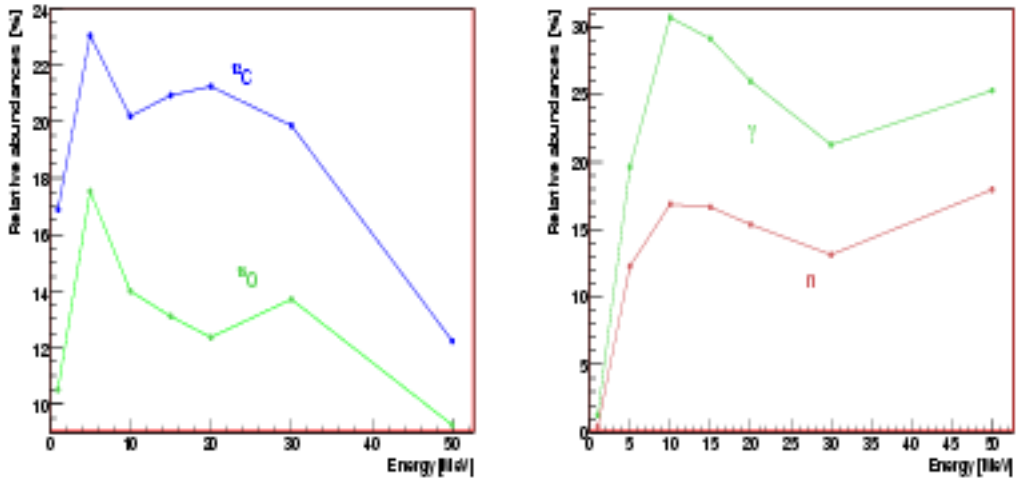

(a) Carbon and Oxygen isotopes.

(b) γ-particles and neutrons.

Figure 5.12: Relative abundances of the secondaries produced inside CR39 by the interaction of neutrons with energies in the MeV region (showing 1 to 50 MeV) *vs.* the neutron energy.

5.11 (left) show the abundances obtained for the isotopes of C; in particular ^{13}C is plotted with black dots and other isotopes of C (^{15}C, ^{14}C, ^{11}C, ^{10}C, ^{9}C) are indicated by red markers; the isotope ^{13}C is the most abundant carbon isotope (different to ^{12}C) up to energies around 20 MeV.

It has been reported that for neutron energy $E > 100$ MeV hadron shower production occurs [72]. MC simulations in this region show that π^0, $\pi^{\pm}$ are produced with a production energy threshold around 1 GeV; their relative abundances is at the order of 8%.

5.9 The application of the simulation to SLIM modules

Three SLIM modules were exposed at 3 different locations at Chacaltay in order to evaluate the level of tracks induced in the CR39 by cosmic neutron. The exposure elpased 16 months. After exposure the CR39 foils were etched, and all etch-pits were counted.
A first attempt to interpret the experimental observations was made by simulating

Process	secondary produced
elastic scattering	
$H(n,n)$	p
$C(n,n)$	^{12}C
$O(n,n)$	^{16}O
inelastic scattering	
$C(n,n')C^*$	n, γ, ^{12}C
$O(n,n')O^*$	n, γ, ^{16}O
alpha reactions	
$^{12}C(n,n3\alpha)$	α
$^{12}C(n,n'\alpha)^9Be$	^9Be
$^{16}O(n,\alpha)^{13}C$	α, ^{13}C
hadron production	π

Table 5.2: Main reactions involved in the interaction of neutrons with CR39. Most abundant secondary elements by-products of the main reactions cited.

the interaction of the neutron flux in a CR39 sheet of 1450 μm. Since after etching the thickness is $\sim$ 1000 μm, generated tracks are considered only if their production point is 225 μm above the after etching detector surface.

Two main parameters has to be defined in order to simulate the incident neutron flux, first the number of incident neutrons corresponding to the exposure time, and their energies. The simulation implemented don not considered the contribution of the back-scattered neutrons; so only downgoing neutrons are considered. Both parameters are calculated from the neutron energy spectrum measured at the SLIM site, plotted in figure 5.1. The spectrum plotted as the intensity I times the energy E *vs.* neutron energy *i.e* $E\frac{dN}{dE}$ *vs.* E (on the x-axis is ln E).

The number of neutrons per unit of energy can be written as

$$\frac{dN}{dE} = \frac{dN}{d\log_{10}E}\,\frac{1}{2.3E} \tag{5.1}$$

the factor 2.3 comes from the base change, *ln* to *log*. Eqn. 5.1 can be approx. by

$$\frac{dN}{dE} \approx \frac{\Delta N}{2.3E\;\Delta\log_{10}\;E} \qquad [cm^{-2}s^{-1}sr^{-1}MeV^{-1}] \tag{5.2}$$

$$E\frac{dN}{dE} \approx \frac{\Delta N}{2.3\;\Delta\log_{10}\;E} \qquad [cm^{-2}s^{-1}sr^{-1}] \tag{5.3}$$

The approximation made can be interpreted as a discretisation (binning) of the distribution; so a histogram of the $\log_{10}E$ weighted by $(E\frac{dN}{dE})/2.3$ was created

(plot in figure 5.13 left). That histogram was used to sample neutron energies in the SLIM MC simulation. Histogram 5.13 (right) shows a sample of 10^5 random values taken from the neutron spectrum histogram, that reproduce the experimental measurements of figure 5.1.

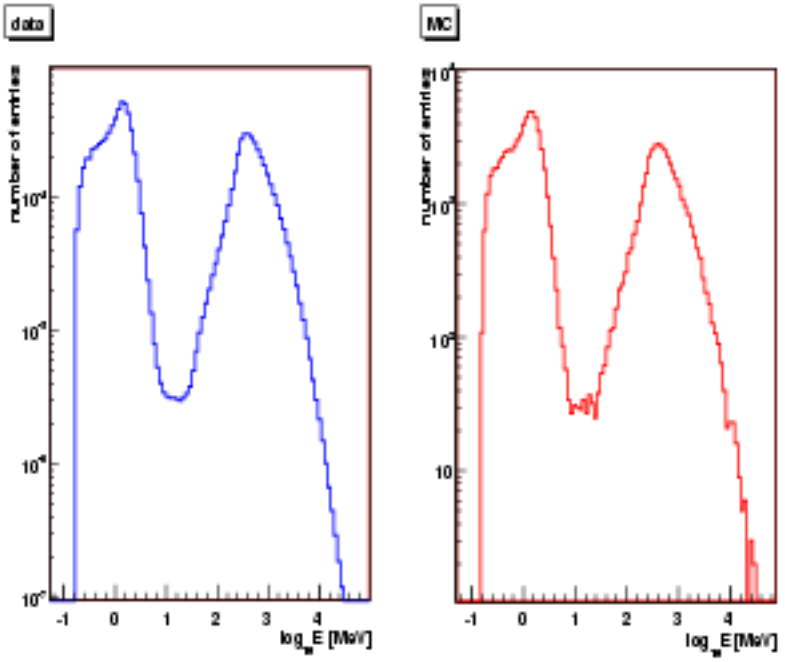

Figure 5.13: *Left:* Histogram of the neutrons energy at the SLIM detector site. *Right:* 10^5 random enegy values (taken from the distribution on the left) used for the neutrons generated in the MC simulation.

Let's now determine the number of incoming neutrons for a given exposure time. The flux measured experimentally in the energy interval E, $E+\mathrm{d}E$ is

$$\Phi = E\frac{\mathrm{d}n}{\mathrm{d}E} \tag{5.4}$$

so the number $\mathrm{d}n$ of neutrons is given by

$$\mathrm{d}n = \frac{\Phi}{E}\mathrm{d}E = \Phi\,\mathrm{d}(\log E) \tag{5.5}$$

The number of neutrons over an element of surface $\mathrm{d}S$, solid angle $\mathrm{d}\Omega$, and time interval $\mathrm{d}t$ is

$$\mathrm{d}n = \Phi\,\mathrm{d}(\log E)\,\mathrm{d}\Omega\cdot\mathrm{d}S\,\mathrm{d}t \tag{5.6}$$

$\mathrm{d}\Omega\mathrm{d}S$ is the detectors acceptance. For a surface S over a time Δt one has

$$N = \int_{\phi=0}^{\phi=2\pi}\mathrm{d}\phi\int_{\delta=0}^{\delta}\sin\delta\cos\delta\mathrm{d}\delta\int_S\mathrm{d}S\int\mathrm{d}t\int\mathrm{d}\log E \tag{5.7}$$

where ϕ is the acimuthal angle, δ is the zenith angle, ranging from 0 to δ_{critic} defined in 3.1.4. Because neutrons impinge upon the CR39 perpendicullary the the limit angle is not considered, finally

$$N = S\pi \int \Delta t \int \Phi \, \mathrm{d}(\log E) \tag{5.8}$$

The integral $\int \Phi \, \mathrm{d}(\log E)$ is evaluated numerically by integrating the energy spectrum, histogram 5.13 (right) over the interval 180 keV to $\sim$ 100 GeV which are the minimum and maximum values experimentally found. For an exposure time of 16 months, $N = 1120770$.

The MC simulation implemented makes a run for a single neutron; so to simulate the total number of neutrons, N runs were made, and the data generated for each run was storaged.

5.9.1 Simulation Results

Figure 5.14 (Right) show the distribution along Z of the number of interactions of primary neutrons inside the detector. Figure 5.14 (Left) shows the radial distribution (in the plane X-Y) of the number of interactions. Neutrons were originally generated with a momentum direction along the Z-axis. One observes no asimmetry for the interaction points along the detectors thickness, even if neutrons were generated with different energies. The plot on the right shows that the 92.6% of the interactions occur along the incident direction, in a circular region of radius $\sim$ 150 μm on the detector plane (XY); the number of interaction points then decreases linearly with the increasing radius.

The relative abundances of secondary particles are plotted in figure 5.15. The most abundant particles produced are protons, with a relative abundance of the 52.4%, then ^{12}C isotopes (12.5%), γ-particles (9.5%), secondary neutrons (9.3%), ^{16}O isotopes (8.5%), and α particles ($\sim$2%). The other species quoted on the plot contribute for less than $\sim$ 1%.

For the more abundant species, the generation mechanisms are listed in table 5.3.

The most important mechanism for neutrons interaction is the hadron elastic proces that is the elastic scattering of primary neutrons with the constituent elements of CR39 (H, C, O); protons and isotopes (^{12}C, ^{16}O) are mostly generated by this process. Inelastic scattering (Neutron Inelastic) is the second most frequent process that neutrons undergo; by-products of this mechanism are γ and α particles.

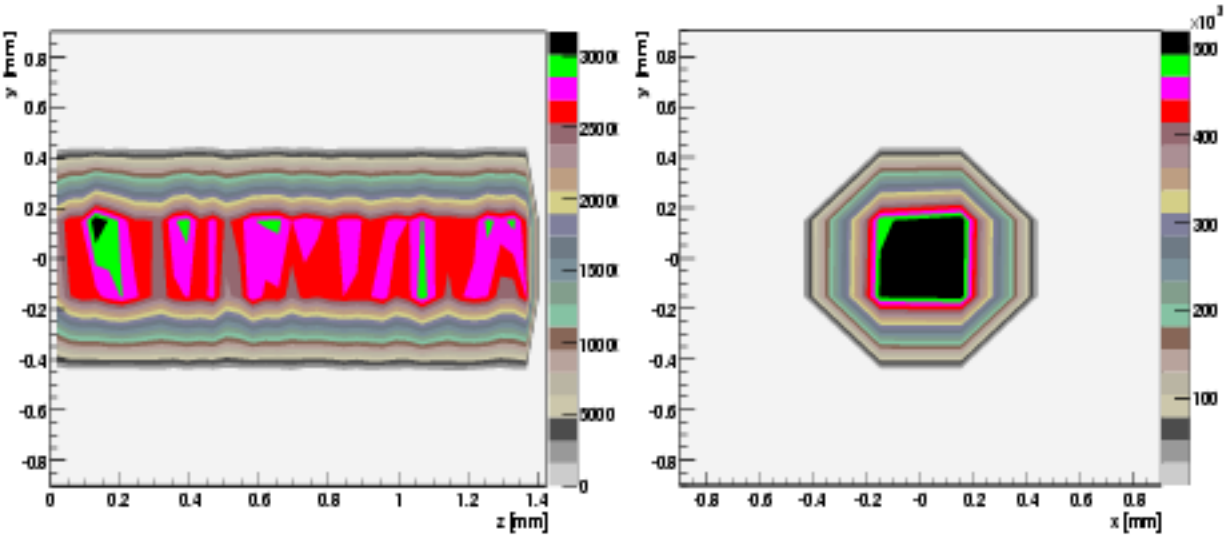

Figure 5.14: *Left:* Profile distribution, along the beam direction (Z-axis) of the numerical density of the interaction points of the primary neutrons. *Right:* Radial distribution, around the beam axis, of the numerical density of the primary interaction points.

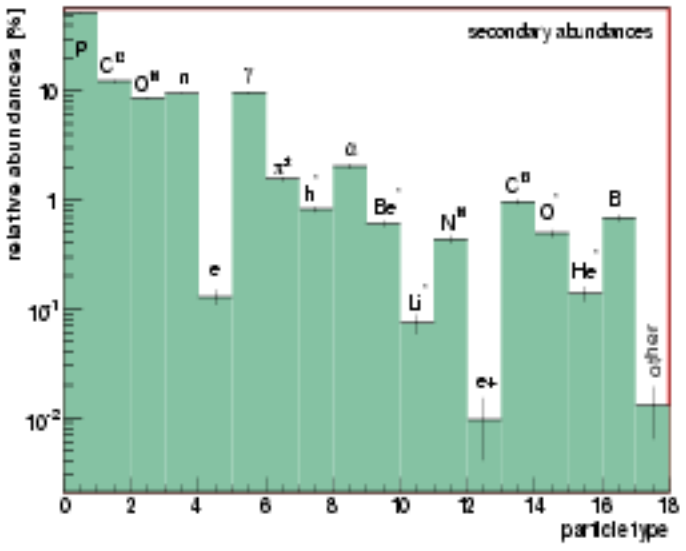

Figure 5.15: Secondary production inside CR39 (1000 μm, post etched thick). The relative abundances (ratio of the number of secondaries of one specie and the total number of secondaries.) are expressed in percentage. Statistical errors are indicated with bars.

Secondary	Process
p	Hadron Elastic (89%), Neutron Inelastic (11%), Proton Inelastic (0.1%)
^{12}C	Hadron Elastic (94%), Neutron Inelastic (5.9%), Other(0.1%)
γ	Neutron Inelastic (84%), Decay (14%), other (2%)
n	Neutron Inelastic (99.6%), Other (0.4%)
^{16}O	Hadron Elastic (95%), Neutron Inelastic (4.6%), Other (0.4%)
α	Neutron Inelastic (99.1%), Other (0.9%)

Table 5.3: Physical processes by which secondaries are generated inside CR39.

5.9.2 REL Distribution of Secondaries

The CR39 detection threshold is REL_{min} =50 MeVcm^{2}g^{-1} and 200 MeVcm^{2}g^{-1} for soft anf strong etching conditions respectively, as discused in section 4.4. Thresholds are included in the simulations by requiring that only particles with REL longer than threshold are detectable. Figure 5.16(a) is the REL distribution for secondary protons. In the figure are also the for soft and strong etching. The number of detectable particles is obtained by integrating the REL distribution from $REL > REL_{min}$.

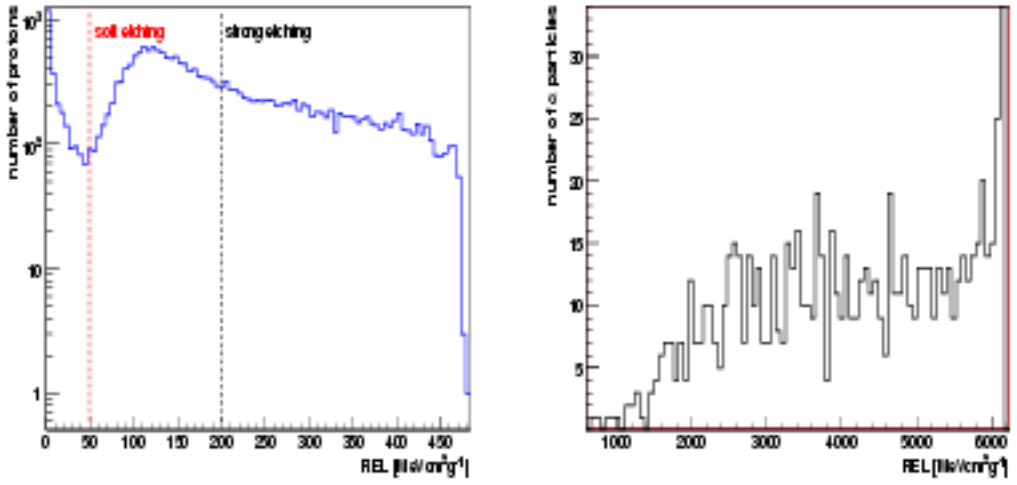

(a) Secondary protons, the dashed lines represent different detector thresholds.

(b) Secondary α-particles

Figure 5.16: Restricted energy loss distribution for particles generated inside the CR39 detector.

For ^{12}C and ^{16}O ions and for α-particles it was found that their REL is always

larger than REL_{min} for strong etching. That implies that all such particles are detectable under both etching conditions. The REL distribution of α-particles is shown in figure 5.16(b).

For protons the REL distribution is continuos in the range ~0-500 MeVcm^{2}g^{-1}; the number of detectable protons is very sensitive to the detector threshold; for REL_{min} =50 MeVcm^{2}g^{-1} the fraction of detectable protons is 89% of secondary protons; for REL_{min} =200 MeVcm^{2}g^{-1} the same fraction is 42%.

5.10 Experimental Measurements of SLIM Background Tracks.

Three SLIM-like modules were exposed in the same detector location in role to evaluate the background signal for cosmic neutrons. The exposure lasted 16 months. After retrival the CR39 top sheets were etched with soft etching conditions (REL_{min} =50 MeV cm^{2}g^{-1}). A scan was performed over an area of 30×30 mm^2, with a transmision microscope with global magnification 25× occular and 6.3× objective. The scan area was sub-divided in 30 zones along each axis (30×30 grid).

The spatial distribution of the tracks over one of the detectors is shown in figure 5.17. The mean track number is homogeneus over the three detector foils.

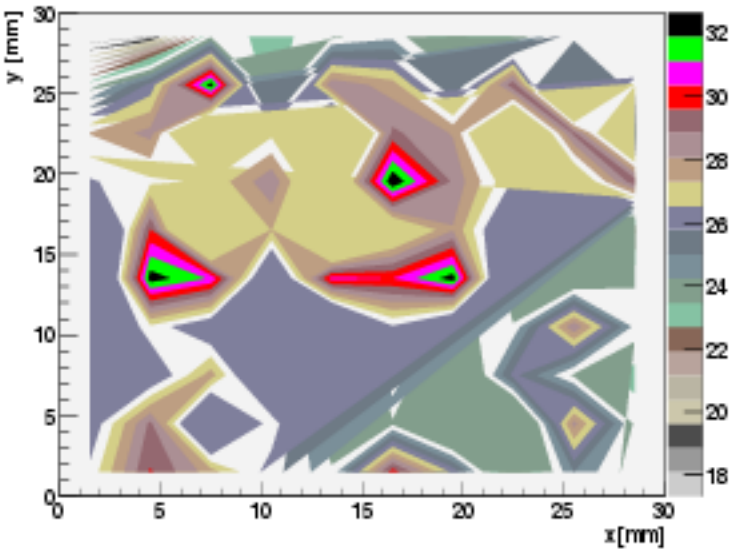

Figure 5.17: Mean numeric density of the background tracks measured in a CR39 sheet. The data is represented in a two-dimension histogram, with a bin width of 1 *mm*; the number of tracks is plotted with a color scale.

5.10.1 Track Morphology

In particullar neutron induced tracks morphology is strictly related with the point of interaction of the neutron with the detectors bulk material; yielding different positions of the latent tracks (LT) inside the detector. The shape of the post etch-pit cones for different locations of the LT before the etching are represented in figure 5.18 with dashed lines. In the figure the positions are denoted by the letters a, b, c and d, and the shapes of the post etch-pit cones are indicated with the relative prime letters a', b' c' and d'. According to [82] different shapes of the etch-pit cones

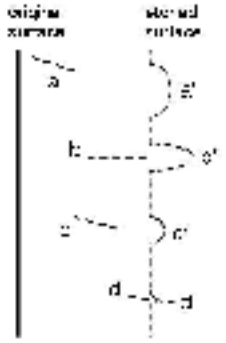

Figure 5.18: Latent tracks in CR39 (dashed lines) at different depths inside the bulk material (a, b, c & d). The post-etched surface is denoted by the dotted line, and the correspondent etch-pit cones are denoted by the prime letters a', b' c' and d' [82].

are expected; and the radius of the etch-pits, even for a certain specie of particle emitted in the same direction through a common interaction, should be distributed widely since it depends on the depth where the interaction takes place.

The next sample of photographs shows different kind of tracks found on the first CR39 layer of the SLIM stacks. All of the photographs are made with a 3.6× objective, a diaphragm of 3.5 and an illumination set at 3200 K. Figures 5.19(a) and 5.19(c) shows the tracks as seen on the top surface of the detector, and figures 5.19(b) and 5.19(d) shows the photographs of the tracks as seen on the bottom surface of the detector.

Another type of tracks correspond to those originated by "multiple track" reactions like $^{12}C(n,n'3\alpha)$ or $^{16}O(n,n'4\alpha)$. The shape of these tracks is complex; but are recognized by the presence of "prongs" (small tracks). In these processes the α particles forms small tracks, all with a common origen (the point where the reaction occurs). Figure 5.20 shows a micro-photography of a track of this type.

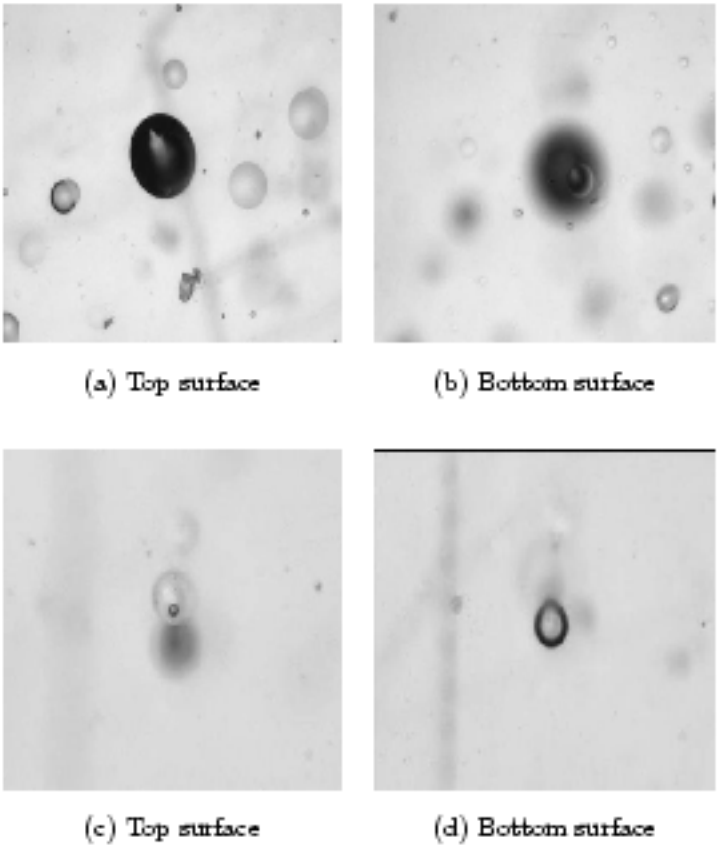

(a) Top surface (b) Bottom surface

(c) Top surface (d) Bottom surface

Figure 5.19: Micro-photographs of recoil tracks found in the uppermost CR39 layer of the SLIM stacks, as seen on both sides of the detector sheets.

5.10.2 Identification of Recoil Ions

In order to identify the type of recoil ions, measurements of the dimensions of the track on the top and bottom surface are made. Using the track's semi-axis and the v_b value of the sheet, the reduced etch rate p for the track on the front and bottom surfaces can be calculated using equation 3.8. Then using the calibration curve plotted in figure 4.8(a) the corresponding restricted energy losses REL for the front REL_{front} and for the bottom REL_{bottom} surfaces are obtained.

Figure 5.21 shows the REL of different ions function of their kinetic energy K; REL_{front} correspond to some K_0 according to the "candidate" ion considered. For each ion with intial energy K_0, the energy loss inside the CR39 is calculated using the Ziegler's SRIM program[3] [84], and the final kinetic energy K is estimated.

[3] www.srim.org

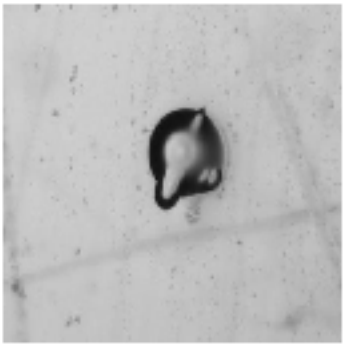

Figure 5.20: Micro-photograph of a neutron induced track produced by a "multiple track" reaction; the complex shape of the track is due to the presence of small α-tracks, generated in the interaction.

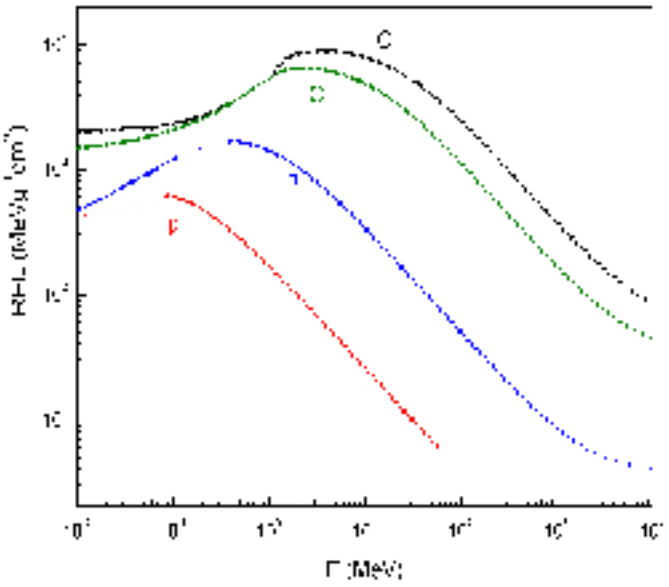

Figure 5.21: Restricted energy losses versus kinetic energy for different ions obtained with the MC simulations. For the low energy regions the curves were evaluated using the SRIM program.

Using figure 5.21 is found which ion have energy losses REL_{front} and REL_{bottom} corresponding to kinetic energies K_0 and K.

For example measurements of the track shown in figure 5.22 yield to $p_{front} = 1.335$ corresponding to $REL_{front} = 454.74\ \mathrm{MeVg^{-1}cm^2}$ and $p_{bottom} = 3.335$ corresponding to $REL_{bottom} = 739.32\ \mathrm{MeVg^{-1}cm^2}$. Comparing the REL values obtained with the functions plotted in figure 5.21, it is found that the energy losses corre-

spond to a carbon ion with an initial energy of K_0 =298 MeV, leaving the sheet with a final energy of K ∼161 MeV. The final K is withing the experimental errors equal to the kinetic energy calculated evaluating the energy losses.

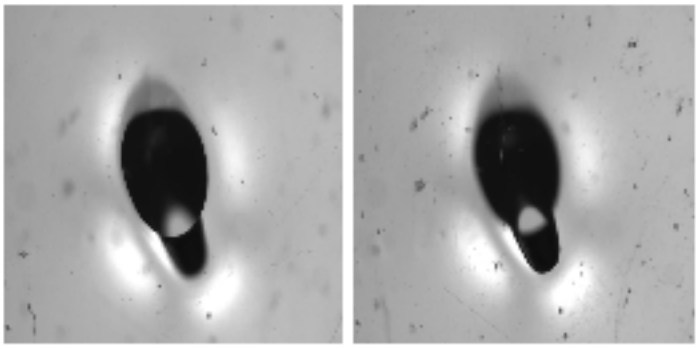

(a) Top surface (b) Bottom surface

Figure 5.22: Micro-photograph of the track on the top and bottom surfaces of the detector sheet. The track correspod to a Carbon recoil measured in the first layer of CR39 of the 4042 SLIM stack.

Chapter 6

The CAKE Experiment

The CAKE (Cosmic Abundances below the Knee Energy) balloon experiment aims to measure the primary cosmic ray charge spectrum on to the top of the Earth's atmosphere by means of sheets of CR39, Makrofol and Lexan nuclear track detectros.

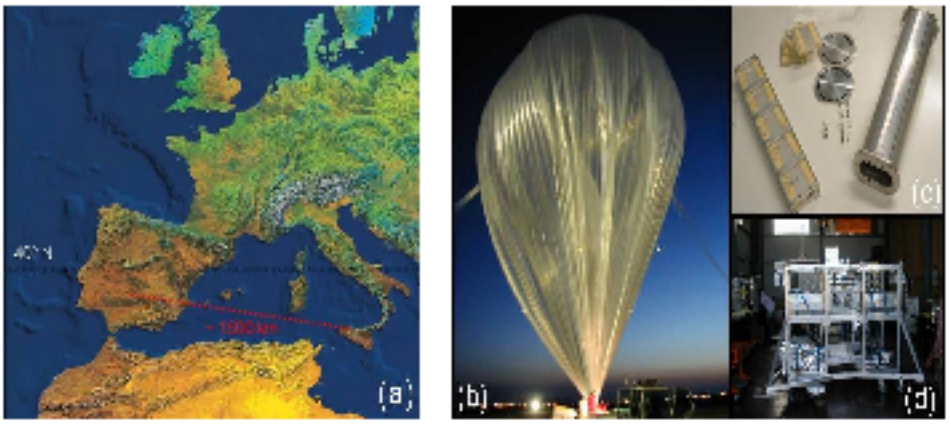

Figure 6.1: (a) Trajectory of the balloon flight, from Sicilly, Italy to the central Spain ($\sim$ 1500 km). The rigidity cut-off at the flight latitude was about 8 GV. (b) The 83.4×10^4 m^3 volume RAVEN balloon. (c) Composition of a cylindric aluminum container: one assembled tray with 5 stacks is shown. (d) The balloon gondola: among the payload, the boxes with the CAKE detectors are visible on the upper sectors surrounding some electronics.

The balloon was launched in July 1999 from the Trapani-Milo base (12.5°E 32.92°N) of ASI (*Agenzia Spaziale Italiana*) and landed in central Spain after 22 hours of flight. The trajectory of the flight is indicated in figure 6.1 (a). The plafond altitude was 37-40 km (3-3.5 gcm^{-2}) for about 20 hours. Along the balloon

trajectory the mean vertical rigidity cut-off was about 8 GV (limiting the minimal energy of the impinging CRs with a cut-off for E<3 GeV/nucleon)[85].

The principal elements of the flight-chain which composed the balloon were: a $83.4 \times 10^4\, m^3$ volume RAVEN balloon (fig. 6.1 (b)), a $24\, m^2$ area Irvin parachute, 20 m long quadrifilar steel wires and 90 m pyro wires connected to a pair of explosive device for cutting the steel wires at the end of the flight, a radio beacon, the COBY-2 payload and the gondola which was not equipped with a pointing system (fig. 6.1 (d)).

CAKE was composed of 80 multi-layer stacks of NTD sheets, each are 11.5 × 11.5 cm^2 for a full detection area of 1 m^2. Each stack had a core of 10 sheets of Makrofol 0.25 mm thick, sandwiched by several layers of CR39, 0.7 mm or 1.4 mm thick. The total thickness of a stack was about 2.3 g/cm^3. The stacks, five by five, were inserted into aluminum cylinders; the cylinders which manteined an internal preassure of 1 Atmosphere all the balloon flight. The cilinders four by four, were inserted into aluminum boxes, with an internal insulating foam coverage (fig. 6.1 (c)). The entire experimental set-up was lodged on the payload of the balloon. The temperature inside the cylinders containing the stacks was never greater than 34°C. Studies performed in a controlled heating room at C.N.R. of Bologna have determined that CR39 keeps constant its sensitivity from -50°C up to 50°C [70]. The thickness of the total amount of Al which was surrounding the stacks, considering the cylinders and boxes, was less than 2.7 g/cm^2 thick.

6.1 Detector Calibration and Limit Angle

The CAKE NTDs were calibrated using 158 A GeV ^{207}Pb ions at CERN SPS (Giacomelli et al., 1997, 1998 [86]), the reduced etch rate p was related to the charge number of the crossing particle Z (see CR39 calibration exposed in section 3.2). The etching conditions used for calibrating the CR39 detectors were 6N NaOH at (70±0.1)°C for 30 hours. Such conditions were used for etching the CAKE stacks which flew on the balloon. The calibration curves are plotted in figure 6.2 (left) for three values of the bulk velocity. Figure 6.2 (right) shows the limit angles obtained for the three v_B values considered in the calibration curves.

6.2 Automatic Scan Session

Ten stacks out of the 80 ones contained some Al or Pb 0.5 mm thick; the overall thickness of each one of such the stacks was about 3.0 and 4.8 g/cm^2 respectively, and represent the 12.5 % of the whole detector. Such "heavy" stacks were intended for fragmentation studies. The results in this thesis concerns only the analysis of those 70 normal stacks assembled with NTDs only. For each one of the 70 stacks,

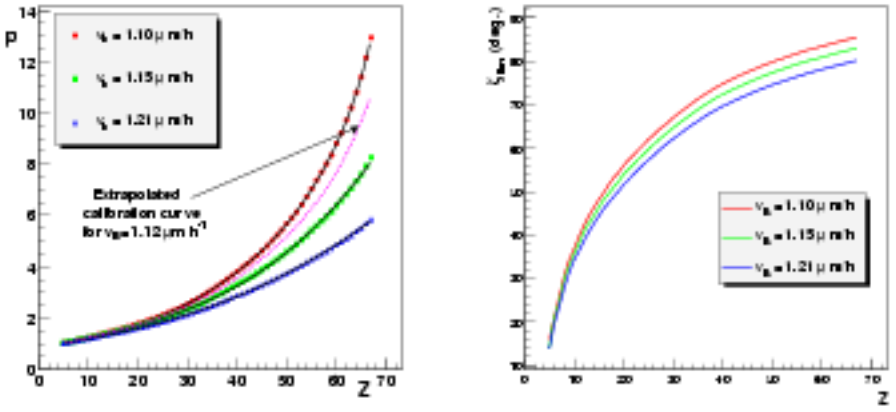

Figure 6.2: *Left:* calibration curves for CR39 sheets etched with 6N NaOH at (70±0.1)°C, for three values of v_B. The dashed line indicates a computed calibration curve for an intermediate v_B, obtained by interpolating p *vs.* v_B data [70]. *Right:* Limit angle (ζ is the zenithal angle) as function of the ions charge, calculated in CR39 for three values of bulk etch velocity.

4 CR39 detector foils were scanned using the SAMAICA system (described in sect. 3.3) with automatic scan sessions. The scanned area of each foil was reduced to 8×8 cm^2 for bypassing the boundary slices of the sheet; the duration of a scan session was about 12 hours. The complete guide for the parametrization of the SAMAICA system can be found in [74] and extensive explanations of the parameters used in the scan of the CAKE detectors are given by [70]. A detailed discussion of some of the parameters that may introduce uncertainties or ambiguities in the automatic scan process are discussed forward in this chapter.

System of reference

The best measure of the dimensions of the track released by a high energy ion is obtained by averaging all the ion tracks along its trajectory through the piled sheets of one stack. In order to scan a region of one sheet, SAMAICA builds an ortogonal (XY) reference frame starting from two points of the foil set by the user called Markers. SAMAICA refers the position of all the tracks to such a reference frame in order to pursue the ion trajectory through piled foils. A correspondence between the markers on all the scanned sheets is required. Detector sheets were aligned inside the stack by means of three aluminum pins passing through three fiducial holes per sheets with a diameter of 3 mm each. The center of two of the fiducial holes were chosen as markers for the frame determination (see figure 6.3,

the fiducial holes used as markers are M1 and M2). The fiducial holes are also used to fix the detector on the microscope XY-stage which was carrying 3 similar pins disposed acording the same design. In resulted that the 2 markers used to define the reference frame had limited systematic error due to the positioning of the foils onto the microscope stage, with a minimum spindle pitch ($< 10\mu$m), and a statistical uncertainly due to the repetition of the movements of $\pm$ 1μm.

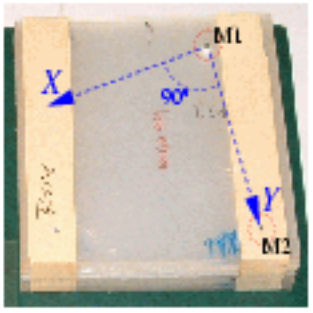

Figure 6.3: The sheet reference frame is determined from two fiducial holes (M1 and M2) which are chosen as markers for SAMAICA.

The position of the measured tracks is thus referred to the frame defined by the fiducial holes, such system of reference is called the *fiducial-frame*. Thus, the relative uncertainty of the track position on two different sheets is strongly reduced.

Central brightness and minimum perimeter parameters

The optical microscope of the SAMAICA system works by reflected light, so that any engraved element on the sheet absorbs the light and appears darker than the rest of the sheet surface. Since the etched pit related to a high energy ion is deeper than any other track or plastic deffects, it higly absorbes the microscope light. Figure 6.4 shows a snapshot of SAMAICA measurement display: because of not correct system parametrization, good and noise tracks are either measured or discarded.

The brightness of a track is a crucial parameter in order to distinguish between signal and noise tracks. The SAMAICA system was developed to measure tracks of ions at accelerator beams, with almost all the particles impinging with the same angle with respect to the detector surface. Such beam characeristics determine small fluctuation of track's brightness, even it still depends on the track dimension. Anyway for accelerator beams, the ion tracks present homogenous brightness through the track base. For this reason the SAMAICA system allows the retrival of the track brightness but only in the central part. Thus during the automatic scan, the on line selection of the measured tracks depends strongly on the settings of the central brightness threshold parameter CB_{th}, unfortunately without any reference to the track ellipticity (ratio between the track major to minor semi axis). When

measuring cosmic ray tracks this is a strong limitation since the impinging direction of the cosmic ions are higly varying, and experimentally we observed that the track central brightness sensibly increases with the track inclination. If a limitant CB_{th} cuts the background tracks off (which are mainly circular with a high brightness) also various good inclined tracks are lost. In this way, the CB_{th} threshold affects the angular acceptance for the measured tracks.

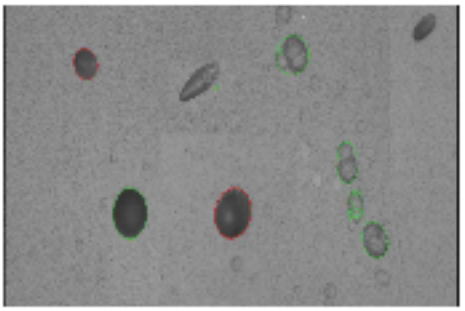

Figure 6.4: Composition of images obtained with the SAMAICA system; darker tracks (low CB ~100 arbitrary units) correspond to good tracks (tracks enclosed by a green and red circles). The gray chain of bubble shaped tracks enclosed by green contours is a source of background tracks (with high $CB \sim 200$ arbitrary units).

The main bias induced by the CB_{th} threshold is in the measurement of small tracks which are formed by light relativistic particles, even though they are not too much inclined. For example beacuse of the limiting angle, Carbon tracks may have a detected zenith angle smaller than 20°, while Iron tracks could reach 58°. Nevertheless, Carbon tracks appears about 1.5 times brighter than the Iron one with the same inclination [70].

The efficiency of the automatic scan depends also on the minimum perimeter of the track. The minimum perimeter threshold P_{min} of the track is another parameter of SAMAICA; given the equation 3.8 which relates the reduced etch rate p to the track axes, a threshold on the minimum perimeter sets a constraint on the minimum detectable p and thus on Z/β.

In order to perform a good countour fit of the track the SAMAICA digital image is tuned using a contrast parameter by varying the light intesity of the microscope (a detailed description of the set up of these parameters can be found in [70]).

For the automatic scan of the CAKE detectors, the CB_{th} parameter was fixed to a value in order to have a minimum bias in the small tracks measurement. This impliesd the introduction of noise which had to be treated off line.

6.2.1 Automatic Scan Efficiency

The automatic scan efficiency ϵ was estimated empirically in [70] by re-measuring the same portion of a sheet first interactively by the operator, changing the parameters involved in the track identification) and then with the automatic scan. It is found than the scan efficiency ranges from $\sim$100% for vertical tracks with perimeter greater than P_{min} and central brightness less than CB_{th} down to even 40% for small tracks (for example the Carbon and Oxygen tracks with diameters below 100 μm) which are inclined beyond $\theta = 20°$. The empirical estimate of ϵ as function the particle charge Z, valid in the range of $0° \leq \theta \leq 60°$ when $P_{min} = 80$ μm, and CB_{th} $\sim$90% of the mean brightness of the field of view is given by equation 6.1; the scanefficiency function of the ion charge is plotted in figure 6.5.

$$\epsilon = 1 - e^{\frac{Z-60}{6}} - 1.3e^{-\frac{Z}{0.9}} \tag{6.1}$$

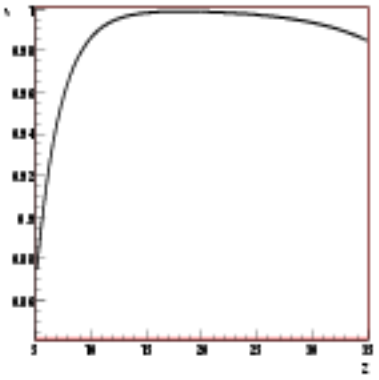

Figure 6.5: Experimewntal estimate of the automatic scan efficiency ϵ as function of the charge of the incident ion [70]: such curve was calculated for the SAMAICA settings: $P_{min} = 80\mu$m and $CB_{th} \sim 90\%$ of the mean brightness of the field of view, in the zenith angle range $0 \leq \theta \leq 60$.

6.3 Neural Network Based Off-line Filter

To reduce the background introduced by the automatic scan, an off line filter was implemented and applied to the raw data. A sample of tracks actually passing through a stack was measured with semi automatic scan runs [70], were the track validation was performed interactively by an operator; such a dataset was denoted as "pure" data. The pure data showed a particular configuration when were represented in the track ellipticity *vs.* track central brigthness plane (called "features" plane). An Arificial Neural Network (ANN) was implemented in order to classify the acquired tracks relying on the features plane.

6.3.1 Multilayer Perceptron Neural Network

An ANN is an algorithm inspired in the way that biological nervous systems process informations. The ANN is composed of a large number of highly interconnected processing elements (called neurons) which work together in order to solve specific problems. An artificial neuron is a device with many inputs and one output. An ANN learns by examples, and it is configured for specific applications, such as data classification, through a learning stage. This process involves adjustments to the connections that exists between the neurons, called synapses (modifying the synaptic matrice which is the array of the connections), as a real biological systems[87]. During the learning stage (training), the network (*i.e.* the array of neurons) is trained to associate outputs with input patterns. In the training mode, is determined a law to establish how a single neuron responds to different input patterns.

Hence, the learning problem amounts to find a synaptic matrix that can "learn" the patterns of a given training set. Any algorithm yielding such a synaptic matrix will be regarded as a *learning rule* [88]. The network identifies the input pattern and tries to output the associated output pattern. The power of neural networks is shown when a pattern that has no output associated with it, is given as an input. In this case, the network gives the output that corresponds to a thought input pattern that is least different from the given pattern. The perceptron is a simple model of a neuron and the multilayer perceptrons (MLP) are networks with at least one hidden layer [90]. The structure of the implemented multi layer perceptron is shown in figure 6.6 (right).

The parameters that are considered to evaluate the trainning and the responce of an ANN are the so-called "classification error"; the classification error is defined as the sum in quadrature, devided by two, of the error on each individual output neuron; the ANN learning method minimizes the total error using the computational methods making loops over all the examples, each loop is called a "training epoch"; the convergence is a property of the method [91].

6.3.2 Neural Network Implementation

The ANN implemented had 4 layers of hidden neurons. For the training of the ANN the "pure data set" was used; once that the ANN was trained we want test it with the "test" set which was composed of all the measured tracks from one automatic scan (*i.e.* valid and background tracks). Each data sets is composed of $\sim$2700 tracks.

Input data to the ANN were chosen recursively from both pure and test sets,

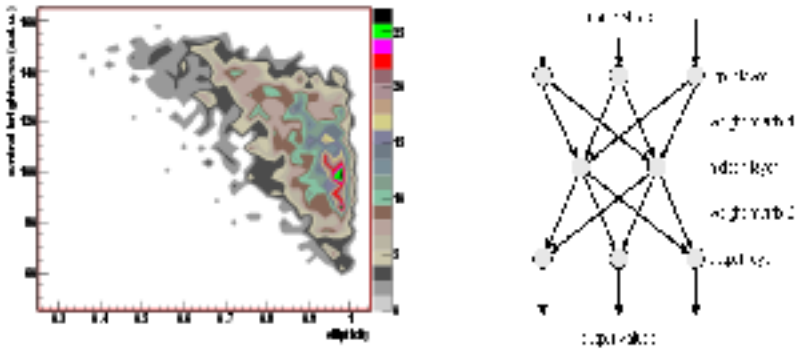

Figure 6.6: *Left:* Features representation of the "pure data" obtained with the interactive scan. The features chosen are the central brightness of the tracks, and the ellipticity. The color scale represents the numerical density. *Right:* Sketch of the multilayer perceptron [89].

then the training and the test process were executed; this loop was repeated untill the training epoch reached the value of 100 iteractions. At each epoch the errors were evaluated and minimazed by adjusting the weights of the ANN outputs. Figure 6.7 (left) shows the relative quadratic errors obtained for the training and for the test stages for each epoch. The plot shows that the errors decreases with the increasing epoch time. It was found that for epoch times greather than 100 the ANN is overtrained.

The output layer of the ANN synthesized the decisional processes of the MLP into an output parameter, called "Label Index" (LI). A value of LI = 0 corresponded to a track recognized as background, while a value of LI = 1 corresponded to a track marked as good one (i.e. perfectly fitting to the pure-data set characteristics). The blue and red-dashed histograms in figure 6.7 (right) show the neural network response as function of the LI parameter on the "test" set. The histogram peaks shows that the quite well the ANN managed to identify the two background and good tracks categories; Nevertheless, the smooth overlapping through all the full range of LI reveals that a sub-set of the analyzed tracks were classified with some uncertainty. Such a sub-set of data corresponded to small bright tracks, sometimes very inclined ones, which could have deceived the ANN as well as the human operator during an interactive scan. It was convenient to fix a LI threshold value, LI_{th} so that only those tracks with LI ¿ LI_{th} were selected.

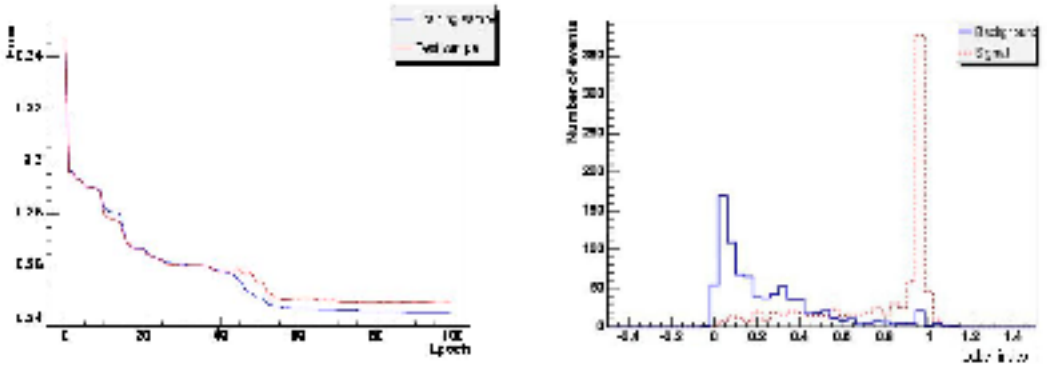

Figure 6.7: *Left:* Errors obtained in the training and in the test processes of the neural network output as a function of the loops over the examples (training epoch). *Right:* Neural network response, showing the label index distribution, the value equal to zero represents background, and the index equal to one correspond to good data. The distributions are overlapped due to miss-classified signal (difficult to evaluate) that contains both data and background.

6.3.3 Filter Efficiency

The filter efficiency is studied using data generated with Monte Carlo (MC) simulations. With the MC simulations implemented for the CAKE experiment (further details are given in section 6.7), track parameters (charge, reduced etch rate, semi axis, polar and zenithal angles) are genereated for the signal and background tracks.

To determinate the filter efficiency ϵ, the MC background tracks are generated with a central brightness (CB) value outside the ranges measured for real tracks. Details about the CB assignement in the MC implementation are given in section 6.7.

The efficiency of the filter ϵ is equal to $\sim$85%; ϵ indicates the amount of data selected from the raw data after the filter application. The value obtained implies that almost 25% of the raw data elimintaed by the filter correspond to background tracks. The filter do not eliminates valid tracks in the selection process.

Figure 6.8 (left) shows the area distribution of the selected (plotted with a red line) and the raw data set (plotted with a black line) corresponding to one sheet only. The plot is made in semi-logarithmic scale to enhace the differences between the distributions. A strong rejection occurs for the smallest tracks (as shown in figure 6.8 left): in fact most of the background due to plastic defects, EOR tracks, and fake tracks present areas less than $\sim$300 μm^2.

Figure 6.8 (right) shows the rejection efficiency calculated for each bin of the area distribution; showing the strong rejection in the first bins and strong fluctuations

the highest bin number due to the small statistical sample.

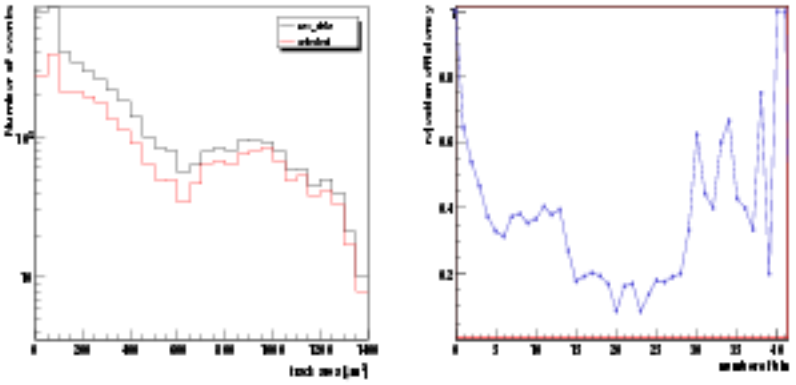

Figure 6.8: *Left:* Tracks area distribution corresponding to one detector foil automatically scanned. The raw data is plotted with a black histogram, an the filtered data is plotted with the red histogram. *Right:* Rejection efficiency (ratio of the number of rejected particles over the total number of particles) calculated for each bin. The fluctuations shown at the higher bins is due to the small statistics.

6.4 Data Overview

As previously explained in section 6.2 236 sheets were scanned (∼70 stacks) with the SAMAICA system. The mean number of measured objects per foil is ∼8500, the number of entries obtained in all the sheets are plotted in figure 6.9 left.

All the scanned foils shared the same experimental conditions during the flight (exposition to CR and background particles) and the etching stages. Seldom not properly correct parametrization of the SAMAICA system yielded a number of measured objects per sheet even greater than two times the reported mean value. Thus, among all the scanned sheets, only those with less than 20000 measured objects were considered for the analysis.

As reported in previous sections, the bulk velocity v_B is an inportant feature of the measured foils: it is stricly linked to the detector calibrations, and it is fundamental to retreive the particles charge number from the measurement of the tracks on the sheets. Due to several factors as small variations of the enviromental conditions during the etching stages, or the differences in the polimeric aggregation of CR39, different v_B resulted among the 236 etched detector foils. As previusly mentioned, a range of 1.10 μm/h $\leq v_B \leq$1.21 μm/h was determinated with the CR39 calibrations. However, a larger range was used for accepting the etched foils; this was called the "acceptance range" and spanned between (0.9÷1.4) μm/h.

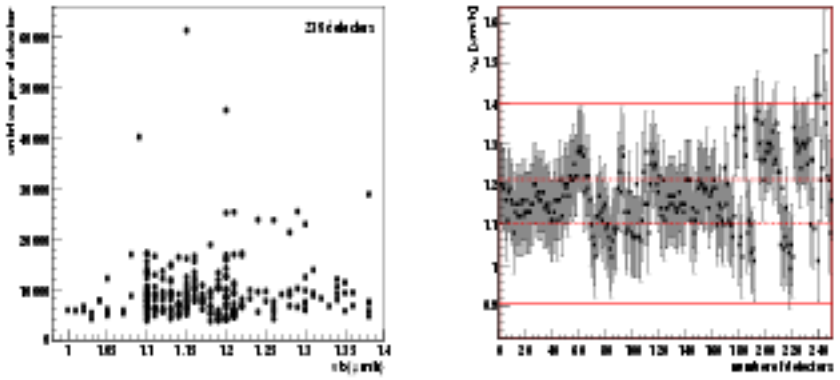

Figure 6.9: *Left:* number of measured objects as a function of the v_B; the mean value of measured objects per sheet is ~8500. *Right:* bulk etching velocity (v_B) of the measured detectors. The dashed lines show the range of v_B used in the calibration of CR39. The "acceptancy range" of v_B for the analysis (plotted with red solid lines) is 0.9÷1.4 μm/h. The errors are due the uncertainty introduced in the thickness measurement.

Figure 6.9 (right) shows the v_B for the 236 analyzed sheets; the solid lines represent the boundary regions of the "acceptance range"; while the dashed lines enclose the calibration range. Both conditions, the "acceptance range" of v_B and the maximum number of measured tracks per sheet (20000) set the *First Level* (F.L.) of selection of the data. These criteria implied wheter the detector foil was to be considered or not in the analysis. From now on the presented analysis is for tracks from the foils that satisfied the F.L. criteria, refeared to "*raw data*"; the total amount of measured objects was 2256540.

Second level of acceptance

The *second level* of acceptance is set by the off line filter applied to the raw data set. The filtered data set is about the 60% of the raw data set; the filtered sample is represented in figure 6.10 (in the "features plane") with red dots, the green dots represent the raw data.

Figure 6.11(a) show the distributions of the ellipticity of the raw and filtered data sets. The raw data distribution shows a bump around *ellipticity*=0.3 indicating tracks with a very sharp elliptic shape. Filtered data, represented with the blue histogram in the same plot (fig. 6.11(a)), show an exponential decrease of the number of tracks with values lower than 0.4.

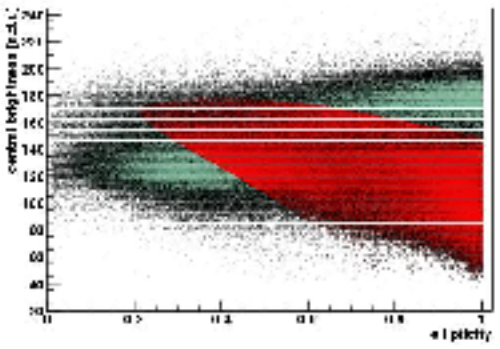

Figure 6.10: Tracks central brightness (measured in arbitrary units a.d.u.) *vs.* track ellipticity. The raw data set is plotted with green dots; the filtered data set is represented with red dots. The filtered data set is ~60% of the raw data.

In figure 6.11(b), the distribution of events from the raw data set as function of the track central brightness shows a peak around 170 a.d.u., which is suppressed by the filter. Such high CB range corresponds to fake tracks, recorded by SAMAICA after a wrong track-contour fit in zone of the foils with an enhanced amount of superficial defects or etched scratches. Indeed, during the automatic measurement, SAMAICA can be deceived by misleading values of the pixel "contrast" and "brightness" parameters along the defetct edges, and it can erroneously merge more contour segments into fake, big and extremely elongated tracks.

The zenithal angle distribution of the data is shown in figure 6.12(a). The zenithal angle ranges from 0 (vertical incidence) up to the limit angle ζ_{lim}.

The polar (azimuthal) angle φ distribution of both data sets is plotted in figure 6.12(b).

Because the gondola was not azimuthally controlled, a flat distribution of events with respect to φ is expected, with no evidence of the east-wast effect due to the terrestrial magnetic field. The figure shows instead an apparent bump around $\varphi = 0$, with a peak-valley discrepancy of about 25%. Such discrepancy on the arrival directions of the CRs is mainly due to the thickness of the Alluminum cylinders which is $\sim$2.7 g cm^{-2} in the barrel and $\sim$8.0 g cm^{-2} at the endcaps. Such differences determined an asymmetry in the experimental transversed by the CRs before arriving to the detectors.

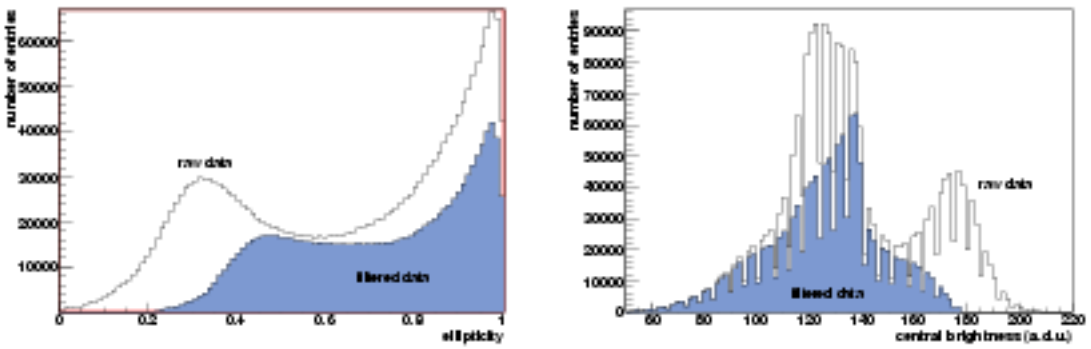

(a) Ellipticity distribution

(b) Track central brightness distribution

Figure 6.11: Distributions of the raw and filtered data sets. The peak around CB=170 *a.d.u.* in (b) corresponds to background tracks which are eliminated by the off-line filter.

6.5 Data Analysis

6.5.1 The Tracking and Selectic Software

To identify tracks of primary CR impinging on the detector, and to eliminate the remaining background in the filtered data, two dedicated software, the "Tracker" and the "Selector", were developed.

Since high energy ions completely cross one stack without a sensible change in their energy, nor in their trajectory. Tracks (one per each foil) which were aligned along the same direction and with the same dimensions, formed the CR signature. A minimum number of 3 crossed foil was the first requirement for the discrimination of signal from background.

The *Tracker* software determines all the possible correlations between tracks from different foils, all belonging to the same stack. Its task is to restrict the number of candidates which should stay along one CR trajectory. Because of the high track density measured on each detector surface, more than one candidate on each foil could be correlated by the Tracker to the same CR trajectory. Thus, the *Selector* software go through a further data manipulation, in order to choose the best fitting tracks (one per foil) to a CR straight line trajectory.

From the geometric characteristics of a track and by knowing the thickness of the traversed material, it is possible to recursively compare the theoretical position of the ion tracks on all the subsequent measured foils.

From the upper foil, the algorithm matches the computed position of the tracked etch-pits to the ones measured on top of the subsequent foil, recording those tracks

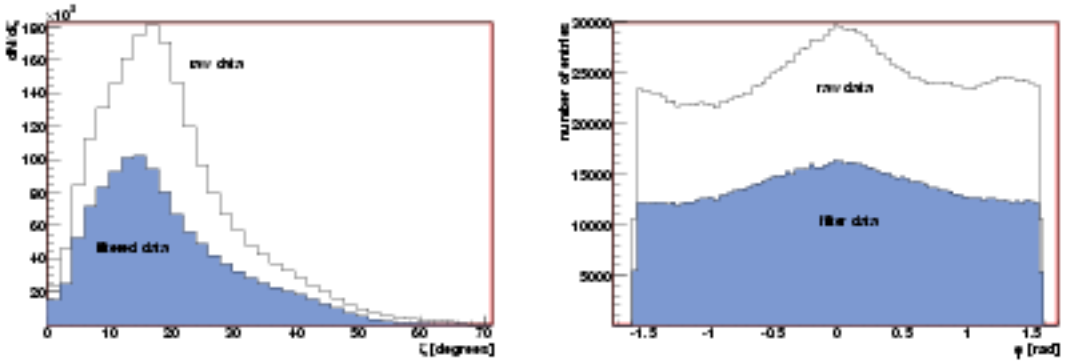

(a) Zenith angle distribution (b) Azimuth angle distribution

Figure 6.12: Angular distributions of the raw and filtered data sets.

which best fit to the computation. Naturally, due to various experimental uncertainties the matching operation is performed by overlapping not a single computed position but a computed extended "confidence area" to the measured tracks.

The determination of the confidence area for the position of the candidate track on the bottom surface is made using geometrical considerations as in the SLIM experiment case (chapter 4). The theoretical distance between one upper track

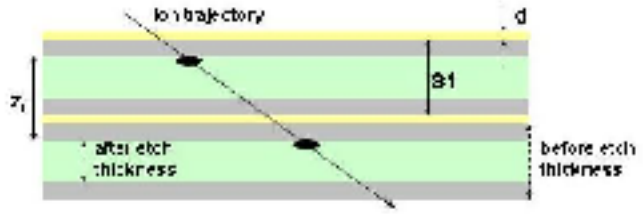

Figure 6.13: Relative distance of two tracks (z_f) between two adjacent sheets after the chemical etching: d is the thickness of the protective lexan sheet, ans $S1$ is the pre-etch thickness of the upper sheet.

and its partner on the subsequent foil , projected on the sheet plane, is evaluated as $r = \frac{z_f}{4\sin(\theta)}$, where θ is the impinging angle, and z_f is the effective layer separation between the two surfaces (see figure 6.13), and it is given by the following relation:

$$z_f = s1 + (v_u - v_d)t + d \tag{6.2}$$

where s1 is the pre-etch thickness of the upper foil, v_u and v_d are the bulk etch velocities of the "upper" and "lower" sheets after an interval of etching time t; d is

the thickness of the protective lexan film that covers each CR39 sheet, with a mean thickness of about 30μm. Because of the uncertainties $\Delta\theta$ and $\Delta\varphi$ (φ is the polar angle) the confidence region is equal to an arc of circumference with its internal and external radius equal to $r \pm \frac{z\Delta\theta}{\sin^2\theta}$, and opening of $2\Delta\varphi$, (see figure 4.11). The uncertainty $\Delta\varphi$ introduced by SAMAICA in the automatic measurement inversely increases with ζ [70]. The θ angle is a function of v_B and the ellipse's semi axis, so its error can be evaluated by propagating the errors in equation (3.10).

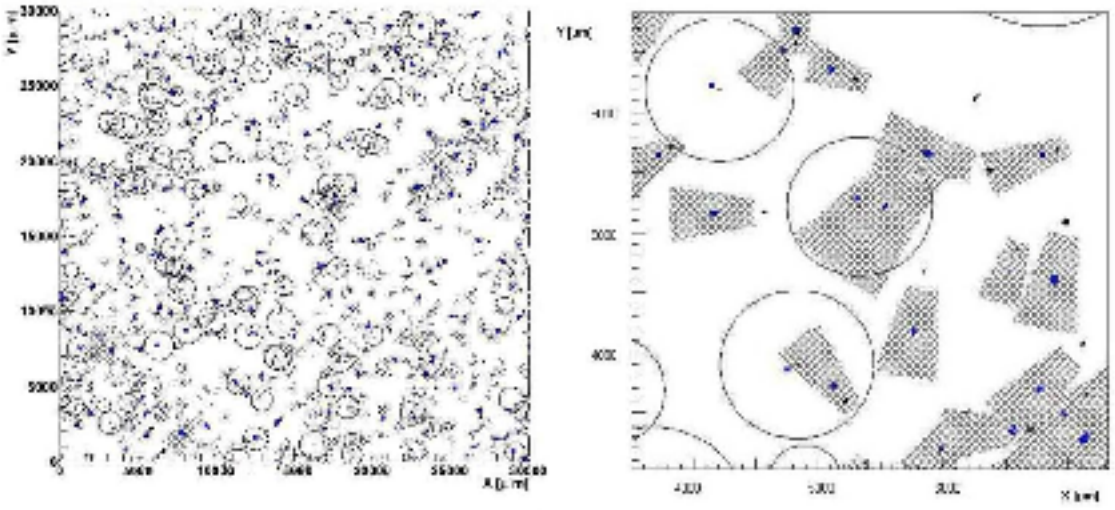

Figure 6.14: *Left:* Scatter plot of the tracks position measured on the "upper" sheet; the black circumferences represent the confidence region; the blue dots represent the candidate tracks measured in the "lower" sheet. ***Right:*** zoom in of the detector surface, showing the tracks on the upper sheet (black dots), and the confidence areas (circular for perpendicular tracks) and arc of circumference for the inclined tracks. Blue dots represent the candidate tracks on the bottom detector surface.

The matching procedure is applied recursively to all the selected foils. Figure 6.14 (left) shows a map of the candidate track positions, and the confidence regions where the partner tracks are searched for. The blue dots represent the candidate tracks measured on the lower sheet. Figure 6.14 (right) is a zoomed region of the figure 6.14 (left); tracks on the upper sheet are represented by black ellipses, and the blue ellipses represnt the tracks measured on the lower layer; the "confidence areas" are also shown.

For quasi-vertical ions, the measured errors on the track axes are greather than the difference between the major and minor axis. In these cases the track is correctly reconstructed by SAMAICA as quasi circular. As already mentioned, such track polar angles suffer of very high uncertaunties. In those cases, the Tracker algotirhm

uses a circular "confidence area" for matching the track positions, as shown in fig. 6.14 (right).

The tracker algorithm produces a set of tracks (one per foil) which should all belong to the same trajectory. Such set is called "event". In order to fine tune the affinity among the tracks of one event, they must pass various other quality checks regarding a limited spread of their dimensions, zenith and polar angle, etc.

The tracker algorithm records all the possible patterns for trajectories of one cosmic rays through the stack, as shown in figure 6.15. One pattern of tracks corresponds to what we has been previously defined as one "event". The Selector algorithm chooses among all the concurrent events the one that best fit to a straigh line trajectory.

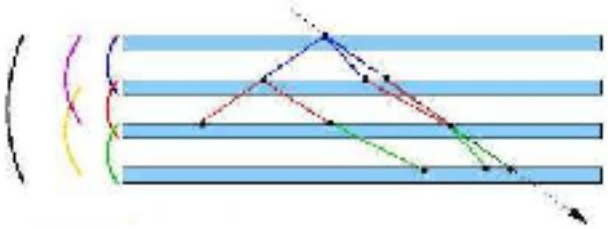

Figure 6.15: Tracking and assembling processes. The dashed line represents the true trajectory of an ion through the stack. The colored lines represents the possible segments reconstructed for two adjacent sheets. Segments with different colors are linked forming a possible trajectory through the required number of sheets. The "Tracker" algorithm records all the possible trajectories, even if they are not real ones. The "Selector" algorith choose the straight line trajectory.

6.6 Results of the Analysis

For each stack, a minimum of 3 foils were scanned with the SAMAICA system. Because of the *first level* of acceptance, 64 stacks contributed with 3 sheets, and 37 with 4 sheets.

The mean v_B values each one of the analyzed stacks are plotted in fig. 6.16, the vertical bars indicates the statistical errors; the calibration range of v_B is indicated with the horizontal lines.

6.6.1 Data Rescaling

Figure 6.17 shows the distribution of the mean etch-rate p, computed with equation (3.8), for all the events which crossed three sheets in a stack. The histograms clearly shows two peaks around p=1.1 and p=1.3 and an outstanding plateau between

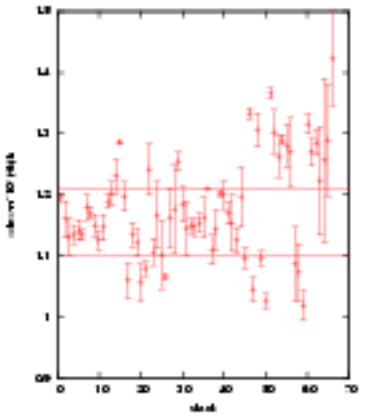

Figure 6.16: Mean v_B values of the analyzed stacks; the horizontal lines indicates the calibration interval of v_B.

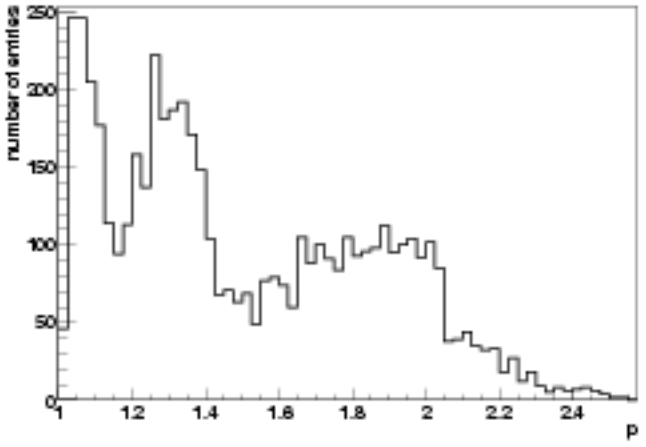

Figure 6.17: Distribution of the computed p for events passing through three CR39 foils.

$1.7 \leq p \leq 2.1$. At a first look, such features seem to reveal the abundances of particular groups of nuclei: in fact, from CR39 calibration exposed in section 6.1, $p < 1.5$ corresponds to the CNO group, while $p \sim 2$ is related to the Fe group. Unfortunately it is not possible to infer any precise estimate of the CR abundances from this plot. In fact, even though each p is strictly connected to the identity of the particle that released the track in the CR39, different bulk velocities v_B for the etched detectors lead to different p, given the same impinging ion. Since the displayed distribution is a superimposition of events measured on several sheets with widely spread values of v_B, any precise feature of CR composition is lost.

Thus, an important step of the data analysis consisted of producing a global

charge spectrum, correctly merging data from all the scanned sheets. The major difficulties lied on getting a proper conversion from the ion track p to the relative ion charge number Z, taking into account of all the various v_B of all the scanned foils.

Apart from the three accurate calibration sets (called *standard*), which were experimentally determined only for three values of v_B=(1.10 ÷ 1.15 ÷ 1.21) μm h^{-1}, the sets of non standard v_B were obtained by means of simple extrapolations. In many cases, by using such indirect calibration sets, the simple conversion from p to Z conversion yielded a distorted charge spectrum. The most evident bias consisted of a contraction as well as an expansion of some of the spectrum features, as the relative distances between the CNO or Fe peaks. Such peaks represent the signature of the CR abundances spectrum. For example, a distorted reconstruction assign to the Fe group a mean charge number Z equal to 24 instead of 26, see figure 6.18 (top left). On the contrary, by selecting data measured only on sheets with standard v_B the measured charge spectrum correctly matched the spectrum features reported in litterature, see figure 6.18 bottom.

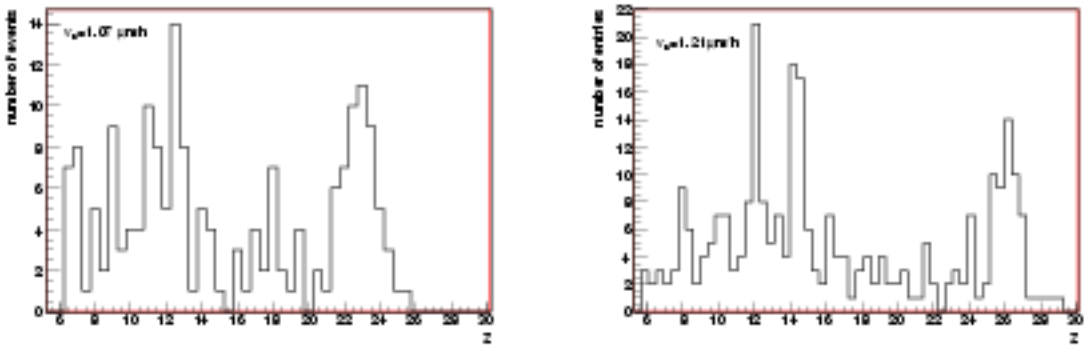

Figure 6.18: Charge distributions obtained for single stacks with different v_B values. The bin width is 0.5 times the unit electric charge. The upper left figure is a mis-recostructed Z distribution. The bias introduced on the conversion from p to Z is due to the non "standard" calibration sets. The mean v_B of each stack is indicated in the figure. The charge distribution plotted on the right is correctly reconstructed, having v_b =1.21 μm/h.

In order to benefit from the largest statistics, a rescaling of the position of the most prominent peaks was performed for the distorted charge spectrum, in order to fit the expected positions.

6.6.2 Final Z Distribution

Figure 6.19 shows the final reconstructed charge distributions, obtained for tracks linked through three CR39 sheets. The bin with is 0.5 times the unit electric charge (e). It is possible to distinguish some elements, *i.e.* the even charge elements which are indicated in the figure.

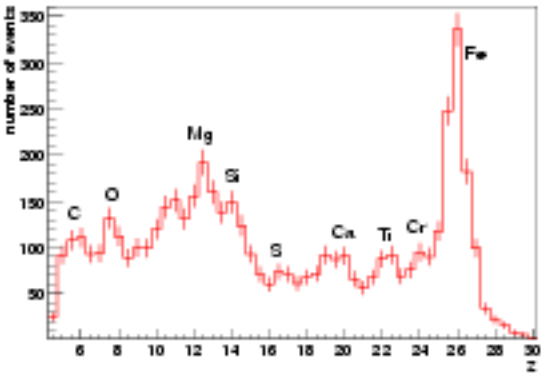

Figure 6.19: Final charge spectrum obtained for the CAKE data ($5 \geq Z \leq 31$); the bin width of the distribution is 0.5e, and vertical bars represent statistical errors. The histogram represent tracks linked through three sheets. Even charge elements are distinguish in the distribution.

The number of heavy ions ($Z \geq 26$) as a function of their charge are plotted in logarithmic scale in figure 6.19; the vertical bars represent the statistical errors.

Figure 6.20 shows the scatter plots of the track axes plotted with a color scale. Green and pink regions show the most dense cluster of events, they correspond to Mg (with track axes of about 40 μm) and to the Fe group (with track axes of about 60 μm). The superimposed lines define the theoretical boundaries for event groups taking into account a v_B range of ($1.1 \div 1.3$ μm/h).

6.7 Monte Carlo for the CAKE Experiment

Expected Number of Events

The number of ions with the same charge Z arriving with a zenithal angle ζ to the detector per unit of time t, over a surface S, with a solid angle Ω, and energy E is

$$\frac{\mathrm{d}n}{\mathrm{d}t\mathrm{d}S\mathrm{d}\Omega\mathrm{d}E} = \Phi \cos\zeta e^{-\frac{z}{\lambda}} \tag{6.3}$$

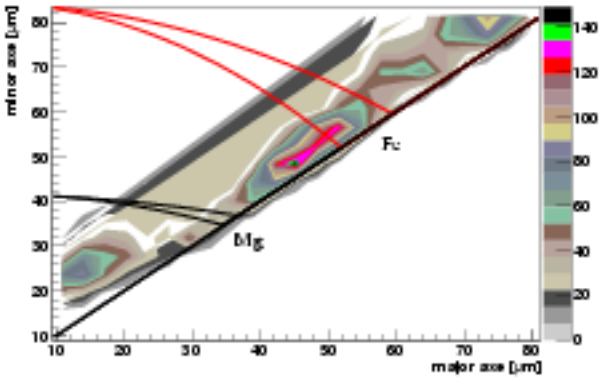

Figure 6.20: Scatter plot of the tracks minor and major axis, the numeric density is plotted with color scale. The red and black lines represent the theoretical predictions of the track axis function of the zenithal angle ζ and p, for the indicated elements. The elements indicated are defined by their charge, therefore their p for a fixed v_B value. The range of ζ is $\zeta_{lim} \div 90°$ (normal incidence).

where Φ is the differential primary CR flux, l is the particle effective path length, and λ is the relative attenuation length. Assuming that the flux is isotropic on the detector we set $d\Omega = -d\cos\zeta d\varphi$. The path length can be expressed as function of the atmospheric depth $X_v = l\cos\zeta$. Replacing these terms in eqn. (6.3) we get

$$\frac{dn}{dtdSdE} = \Phi\Psi \tag{6.4}$$

where Ψ is the angular acceptance

$$\Psi = -2\pi \int_0^{\zeta_{lim}} \cos\zeta e^{\frac{X_v}{\lambda\cos\zeta}} d\cos\zeta \tag{6.5}$$

The angular acceptance of CAKE was evaluated by [70] calculating the atmospheric depth X_v at the flight altitude 38-40 km, and the attenuation length λ in CR39 as a function of the arriving particle mass number. The results obtained for the angular acceptance as a function of the ions charge is shown in figure 6.21 (left). Φ is the differential flux given by Biermann et al. [93]

$$\Phi = \Phi_0 \left(\frac{K}{TeV}\right)^{-\gamma} [m^{-2}s^{-1}sr^{-1}TeV^{-1}] \tag{6.6}$$

where γ and Φ_0 depend on the carge Z of the ions. By replacing eqs. (6.5) and (6.6) in (6.4), and integrating over the surface A and live time T, the total number of ions of a given charge Z impinging on the detector is

$$N = AT\Psi\Phi_0 \frac{10^{3(\gamma-1)}}{\gamma - 1} \left(\frac{K_{min}}{GeV}\right) \tag{6.7}$$

where K_{min} is the minimum kinetic energy necessary to overcome the geomagnetic cut-off R (calculated using eq. 1.6), $K_{min} = -m_0 + \sqrt{m_0^2 + (ZeR)^2}$, with m_0 and Ze the particle mass and electrostatic charge, respectively.

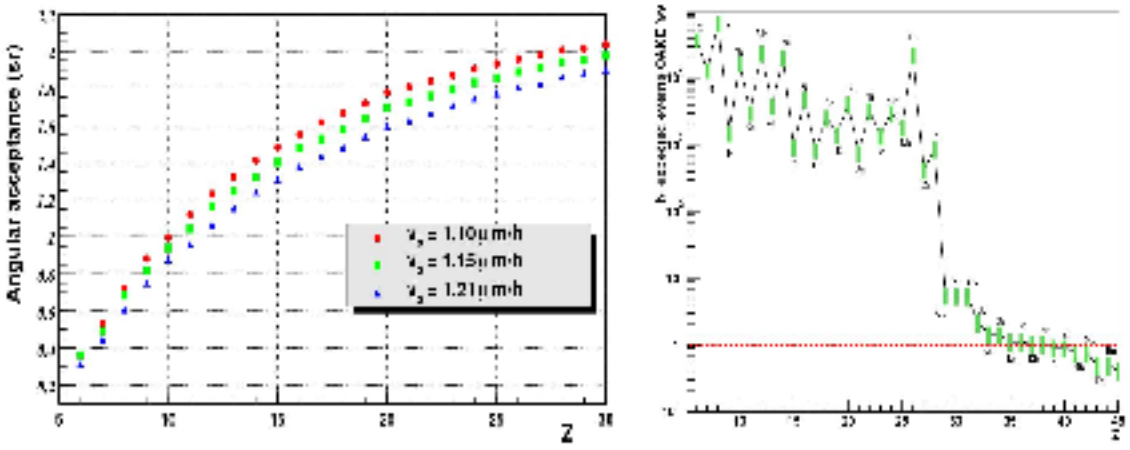

Figure 6.21: *Left:* CAKE angular acceptance for a single sheet as function of the ion charge. *Right:* CAKE expected number of events for each element. The green belts bound the expectations according to an atmospheric depth $2.5 \leq X_v \leq 3.5$ $g\ cm^{-2}$ and a magnetic rigidity cut-off $7 \leq R \leq 9$ GV [70].

The expected number of events at the detector, assuming an effective area of 1 m^2 and a live time of 20 hours is shown in fig. 6.21 (right); the green belt for each bin indicates the fluctuation of the number of events calculated for different flight conditions; the lower bound is calculated for an atmospheric depth $X_v = 3.5\ gr\ cm^{-2}$, and a rigidity cut-off $R = 9\ GV$, the upper bound is calculated for $X_V = 2.5\ gr\ cm^{-2}$ and $R = 7\ GV$. The dashed line indicates the detectable limit.

MOKA generator

MOKA (MOnte carlo for the caKe expected Abundances) is a dedicated software that simulates the CR events over the CAKE detectors. It gives the possibility to generate a "virtual" stack formed by various sheets of CR39. The program weights the statistical frequency of each ion with the expected distribution in figure 6.21 (right). The impinging zenith angle is generated according to a flat distribution versus $\cos^2\zeta$ with $1 \leq \zeta_g \leq \zeta_{lim}(p_g)$, where the limit angle is a function of the generated reduced etch rate value p_g. Each generated charge Z_g is weighted by the CAKE angular acceptance fig. 6.21 (left). The relative p_g has an uncertainty $\sigma_p(Z_g)$ which depends on the detector response showed in figure 6.2, thus a Gaussian p.d.f centered in p_g with width σ_p determinate a Gaussian spread for the generated Z_g. The major and minor semi axis of the track are generated according to 3.8; then

MOKA generates the acimuthal angle $0 \leq \varphi \leq 2\pi$, and the track coordinates over the detector sheet according to a flat distribution.

Central brightness

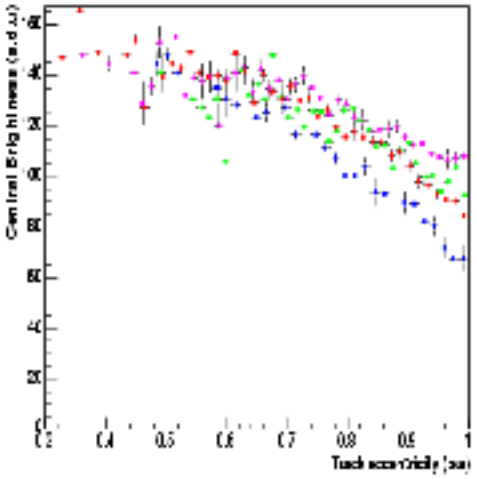

Figure 6.22: Main values of the "good" tracks central brightness as a function of their eccentricity; tracks are classified by their area, and different area intervals are represented with different colors: blue dots $(1700 \leq A \leq 3000)\ \mu m^2$, red dots $(800 \leq A < 1700)\ \mu m^2$, magenta dots $(550 \leq A < 800)\ \mu m^2$, and green dots $(150 \leq A < 550)\ \mu m^2$.

Based on the data obtained with interactive measurements, the central brightness (CB) of real tracks is related to their ellipticity, and to their area. Figure 6.22 shows the mean values of the tracks CB for small ranges of the track ellipticity; the vertical bars are the statistical errors. The plotted data is subdivided into four groups according to track areas: blue dots $(1700 \leq A \leq 3000)\ \mu m^2$, red dots $(800 \leq A < 1700)\ \mu m^2$, magenta dots $(550 \leq A < 800)\ \mu m^2$, and green dots $(150 \leq A < 550)\ \mu m^2$.

Once that the track semi axes are randomly generated, the area is determined and for the corresponding ellipticity value, the CB is generated. MOKA generates the central brightness according to a Gaussian p.d.f. for small ranges of the tracks ellipticity. For a given ellipticity range, the gaussian distribution is centerd around a mean value of CB experimentally measured. The p.d.f σ is an input parameter set by the user.

For the simulated background tracks the CB can be fixed to arbitrary values or randomly values chosen in the tails of the gaussian p.d.f.

6.8 Comparison of Data Reconstructed to Monte Carlo Predictions

Figures 6.23 shows the comparison of the charge distributions between the MC results (red histogram) and the reconstructed data (black markers). The MC is generated for a rigidity cut-off equal to 8 GV, and the range of the charges sampled is from $5 \leq Z \leq 31$; the MC distribution is normalized to the data entries for $Z = 26$. The bin width of the distributions is $0.5e$. The experimental data with statistical errors (black points) comes from ions passing through three detector layers.

The plot represented in figure 6.23 (left) shows the charge spectrum in the range $Z = 10 \div 30$. For $Z > 16$ there is good agreement between data and expectations. Figure 6.23 (right) shows the relative ratio (ratio between the relative difference of the number of generated events with the reconstructed events over the number of reconstructed events), calculated for each bin (again the bin width is $0.5e$); the blue line indicates a relative difference equal to zero (*i.e.* the perfect agreement between data and MC). For the interval $Z > 16$ the radio is $\sim$0.

In the range $10 < Z \leq 16$, both distributions have the same shape. The relative ratio for this charge range, plotted in fig. 6.23 (right) is $MC/Data \sim 1$

The agreement between the MC predictions and the experimental data is apparently worse for low ion charges ($Z < 17$); This effect could be determined by some scanning inefficiencies both of the SAMAICA system and of the off-line filter which are particularly selective with small tracks. Indeed, the estimated SAMAICA scan efficiency ϵ_s (see figure 6.5) strongly decreases with the charge Z of the ions, and the impinging angle.

Since the data acquisition was set up to measure at least all the Neon ($Z = 10$) tracks, only not much inclined Oxygen tracks are recorded [70]. For example the ϵ of the C ($Z = 6$) is $\sim$ 10% lower than the value of the Fe ($Z = 26$), and ϵ of $Z = 16$ is $\sim$2% higher than the values obtained for $Z = 10$.

Figure 6.24 shows the comparison of the number of trans iron events ($Z > 26$) plotted with black dots with the MC expectations, plotted with a red histogram; the vertical bars indicates the statistical errors of the reconstructed data. The bin width of the distribution is 0.5e.

The expected CR abundances predicted by the MC simulations depends on quantities such as the geomagnetic rigidity cut-off (R_{th}) and the atmospheric depth (X_f), whose values could vary during the balloon flight. Figure 6.25 shows the predicted abundance ranges (the red vertical band) for each CR impinging on the CAKE detector with charge $16 \leq Z \leq 31$. The band lower limit is computed by setting $R_{th} = 9$ GV and $X_f = 3.5$ g cm^{-2}, while the upper limit follows after setting

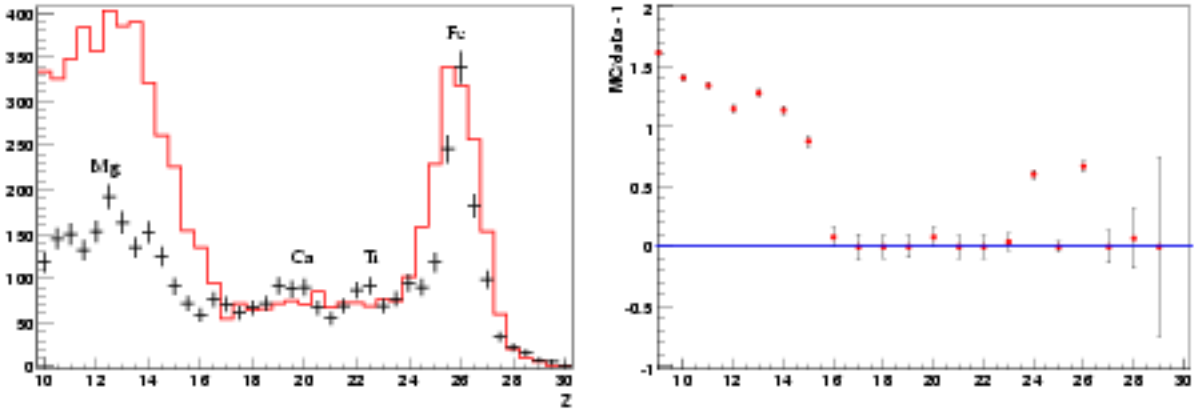

Figure 6.23: *Left:* Comparison of the reconstructed data (black dots) and MC expectations (red histogram). The errors of the data are statistical; the range of the ions charge is $\mathcal{Z} = 5 \div 30$. The bin width is 0.5 times the unit electric charge. The MC distribution is normalized to the experimental values corresponding to Fe ($\mathcal{Z} = 26$); some even charge elements are indicated. ***Right:*** Ratio between the MC expected number of events and the reconstructed events, calculated using a bin width equal to 0.5 times the unit electric charge. The errors indicated with bars are statistical; the blue line indicates a ratio difference equal to zero. The ratio was calculated for the MC distribution normalized to the number of entries of $\mathcal{Z} = 26$ of the reconstructed distributions.

$R_{th} = 7$ GV and $X_f = 2.5$ g cm^{-2}. Such maximum and minimum values for R_{th} and X_f respectively correspond to maximum and minimum estimates, computed for the CAKE trajectory, according to the altitudes and latitudes reached by the balloon during the flight.

The measured abundances are superimposed as black dots, with error bars due to statistics only. The data-MC agreement is sufficiently good, if considering that, in MOKA (MC generator of CAKE), any nuclei fragmentation was not implemented, neither in air nor in the CAKE experimental hardware setup. This could explain the prominent abundance of the simultated Fe group with respect to measured data. Since the Fe peak cannot receive any relevant contribution from the fragmentation of trans-iron nuclei, it is expected to be suppressed of a 5-10%. However, only the Fe fragmentation does not fully explain the different ratios between the Fe and the sub-iron abundances in data and in MC, respectively. A further the explaination of such a problem could reside in the fact that simulations do not consider eventual environmental effects, which could affect the detection efficiency of the CR39 sheets (*e.g.* due to some pressure or temperature instabilities, which could not be efficiently

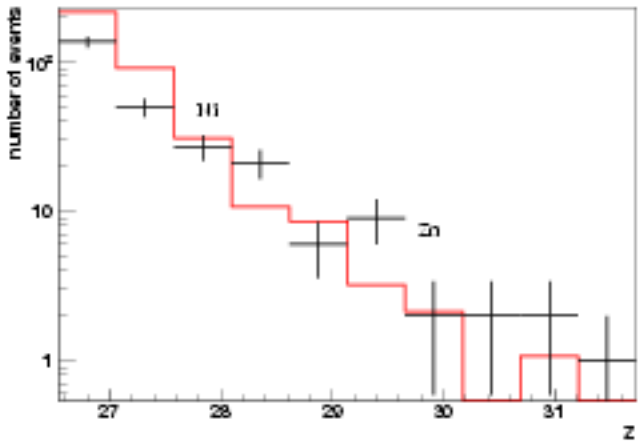

Figure 6.24: Comparison between reconstructed data (black dots) and MC data (red histogram) of the trans iron elements ($Z > 26$); vertical lines indicates statistical errors. Elements with even charges are indicated. MC data is normalized to the experimental iron entries.

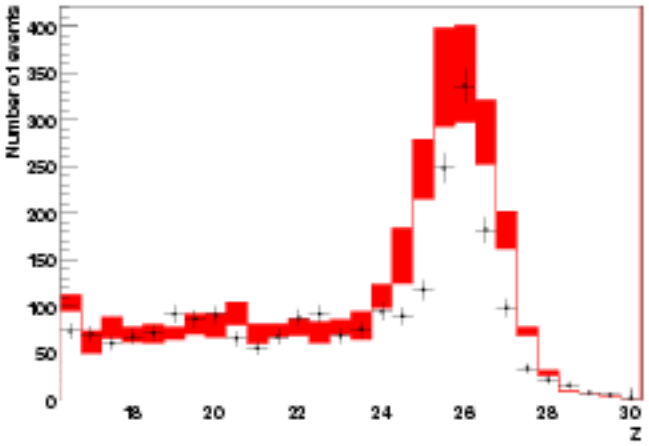

Figure 6.25: Comparison between the reconstructed data (black dots) with statistical errors and the MC predictions. The red band represent the MC boundaries of the expected number of events between the limit cases: the lower bound is calculated considering an atmospheric depth of 3.5 gcm^{-2} and a rigidity cut-off of 9 GV, and the upper bound considering an atmospheric depth of 2.5 gcm^{-2} and a rigidity cut-off equal to 7 GV.

monitored during the flight).

6.9 Comparison with Other Experiments

Figure 6.26 shows the fluxes of elements with $Z \geq 10$ relative to the flux of ^{56}Fe ions obtained with CAKE (red dots). Fluxes are evaluated with equation 6.3, using the exposure conditions of live time, detection area and the detector angular acceptance of each element plotted in figure 6.21 (left). This time, the CAKE relative abundances were corrected according to a rough estimation of the iron nuclei fragmentation in the allumiun cylinders which contained the detector stacks.

In the same figure are plotted (with black triangles) the relative fluxes at the top of the atmosphere obtained by Bhattacharya et al. [94] using CR39 and nuclear emulsions with a balloon-borne experiment, which flew for about 32 hours at an atmospheric depth of 9.8 g cm^{-2} with a minimum cut-off energy $E_{th} \geq 4$ GeV/nucleon for ^{56}Fe nuclei. On the same plot, the results obtained by Grieder et al. [95], with energies above 5 GeV/nucleon for ^{56}Fe nuclei, are superimposed with blue dots.

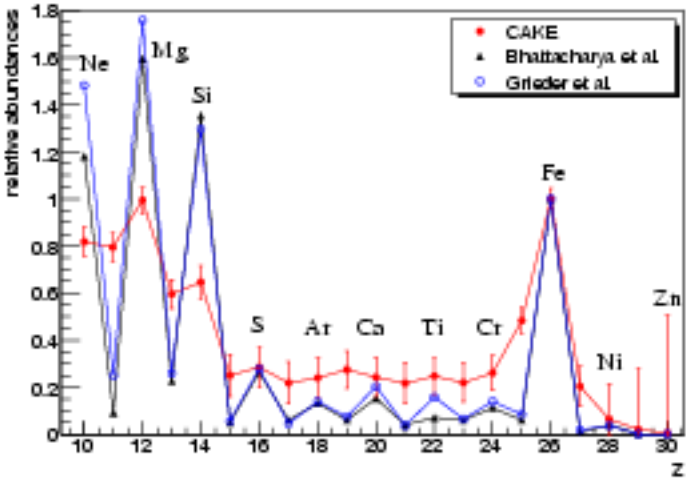

Figure 6.26: Comparison between the relative flux obtained with CAKE (red dots with statistical errors) and other experimental results: Bhattacharya et al. (black triangles) and Grieder et al. (empty blue dots). See text for details.

Conclusion

In this thesis two different aspects of the research field where Astrophysics and Particle physics merge have been explored with the application of the Nuclear Track detectors (NTD). The main scope of the SLIM experiment was the search for exotic heavy particles - Intermediate mass magnetic monopoles, nuclearites and Q-balls - in the cosmic radiation. The experiment locate at high altitude has allowed to extend significantly the parameter space (mass, beta) explored by establishing upper limits (90% CL) in absence of candidates which are among the best if not the only one for all three kind of particles.

A preliminary study of the background induced by cosmic neutron in CR39 was made using Monte Carlo simulations. With the simulation were identified the main processes of secondary production inside CR39. Charged secondary particles are detected by CR39 if their REL is above the detection threshold. It was found that protons are the most abundand specie; by taking into account the CR39 threshold, the detected abundance is about the 51%, the second more abundant detected element is ^{12}C with the 14%, followed by ^{16}O with the 9%, and α-particles contributing with the 2% of the overall background tracks. The other 24% is composed by the contributions of another species of secondaries.

The CAKE experiment was built as a prototype for examining the possibilities of using large area NTDs in space and/or on board of stratospheric balloons in order to determine the elemental abundance of cosmic nuclei with charge number $Z \leq 30$. The data collected during a short balloon flight of CR39 modules for $1.7 m^2 sr$ have been used for studying the charge distribution in the range $5 \leq Z \leq 30$, where significant statistics was available. Automatic procedures for track measuringand algorithms for increasing efficiency in background rejection were implemented. In particular an Artificial Neural Network (ANN) was developed to make an off-line selection of raw data; the efficiency of the ANN was about 85%.

Whitin the charge range of interest even charged elements can be distinghished; the Fe as well as the CNO groups can be clearly identified. Some events likely corresponding to trans-iron elements were measured. The relative abundances were

compared with the results obtained with other experiments, and a discrete agreement was found.

The theoretical expectation of the number of events over the CAKE detector were computed with a Monte Carlo generator that simulates the main features of the NTDs. Experimental results were compared to the Monte Carlo expectations, showing good agreement for nuclei with charge $Z \geq 10$.

Bibliography

[1] G. Giacomelli, Introduzione alla fisica delle particelle elementari, Universita' di Bologna

[2] Astrophysics of Cosmic Rays, V.S. Berezinsnii, S.V. Bulanov, V.A. Dogiel, V.L. Ginzburg and V.S. Ptuskin, North-Holland, Elvesier Science Publishers B.V., 1990.

[3] Genesis and Propagation of Cosmic Rays, Maurice M. Shapiro and John P. Wefel, NATO ASI Series C: Mathemathical and Physical Sciences Vol. 220.

[4] Cosmic Rays: The Second Knee and Beyond, Douglas R. Bergman, John W. Belz, arXiv:astro-ph/0704.3721v1 27 Apr. 2007.

[5] Thomas K. Gaisser, Cosmic Ray and Particle Physics, Cambridge Univ. Press 1990.

[6] Origin of Cosmic Radiation, Thomas K. Gaisser, arXiv:astro-ph/0011524v1 28 Nov. 2000.

[7] (CRIS) The Cosmic Ray Isotope Spectormeter for the Advanced Composition Explorer, www.srl.caltech.edu/ACE/CRIS_SIS/cris.html.

[8] (KASCADE) R. Glastetter et al., Proc. 26th Int. Cosmic Ray Conf. (Salt Lake City) vol. 1 (1999)222.

[9] R. Engel, T.K. Gaisser, P. Lipari & T. Stanev,Proc. 26th Int. Cosmic Ray Conf. (Salt Lake City) vol. 1 (1999)415.

[10] N.N. Kalmykov, S. Ostapchenko & A.I. Pavlov,Nucl. Phys. B (Proc. Suppl.)52B.

[11] A.D. Erlykin, M. Lipski, & A.W. Wolfendale,Astoparticle Physics 8 (1998)283.

[12] A cura di Paul Davies, La Nuova Fisica, Nuova ediz. italiana a cura di Pietro Galeotti. Astrofisica, Malcom S. Longair, editore Bollati Boringhieri (2004).

[13] Interpreting the Cosmic Ray Composition, L.O'C Drury, J.P. Meyer, D.C. Ellison, astro-phy/9905008 (1999).

[14] Supernovae and Nucleosythesis, David Arnett, Princeton Univ. Press, 1996.

[15] Stellar Structure, Lawrence H. Aller and Dean B. McLaughlin, The Univ. of Chicago Press, 1965.

[16] Cosmic Rays, I.V. Dorman, Nauka, Moscow, 1981.

[17] R. Silberberg et al., Cosmic-Ray Souces and Source Composition, The Astrophysical Journal 549 (2001)320-324.

[18] M.A. Shea and D.F. Smart, Vertical cutoff rigidities for cosmic ray stations since 1955. Proceedings of ICRC 2001: 4063 ©Copernicus Gesellchaft 2001.

[19] T.W.B. Kibble, J. Physics. A 9, (1976)1387, Phys. Rep. 67, (1980)183.

[20] G. t'Hooft, Nucl. Phys. Rev. 74 (1974)276.

[21] A. Polyakov, JETP Letters 20 (1974)194.

[22] Shibaji Banerjee et al., Can Cosmic strangelets reach the earth?, hep-ex/0006286v1 (2000).

[23] Ewa Gladysz-Dziadús, Are Centauro exotic signals of the QGP?. arXiv:hep-ph0111163v1 (2001).

[24] P.B. Price et al., Phys. Rev. D18 (1978)1382.

[25] O. Miyamura, Proc. 24th ICRC Rome 1, (1995)890.

[26] Kimball A. Milton, et al., Theoretical and Experimentasl Status of Magnetic Monopoles, hep-ph/0111062v1 (2001).

[27] The MACRO collab., Final results of magnetic monopole searches with the MACRO experiment, hep-ex/0207020v2 (2002).

[28] S. Balestra et al., Search for Nuclearites above sea level and underwater, DFUB 2005-5 SLIM 2005/1.

[29] AMS experiment http://hepwww.physics.yale.edu/yalearns.
Ricerca di Strangelets nei Raggi Cosmici Rivelati dall'Esperimento Spaziale AMS-01, Tesi di Laurea Dafne Baldassari, Fac. di Scienze Matematiche Fisiche e Naturali, Univ. di Bologna, Italy, 2004.

[30] P.A.M. Dirac, Proc. R. Soc. London 133(1931)60; Phys. Rev. 74(1948)817.

[31] A. De Rujula, Nucl. Phys. B435(1995)257. G. Abbiendi et al., Eur. Phys J, C45(2006)1.

[32] G.'t Hooft, Nucl. Phys. B29(1974)276. A.M. Polyakov, JETP Lett. 20(1974)194. N.S. Craigie et al., Theory and Detection of MMs in Gauge Theories, World Scientific, Singapore (1986).

[33] A.K. Guth, Phys. Rev. D 23, (1981)347.

[34] D. Bakari et al., Magnetic monopoles, nuclearites, Q-balls: a qualitative picture, hep-ex/0004019v1 (2000).

[35] E. Medinaceli et al., arXiv:hep-ex/0702050v2 (2005).

[36] S. Ahlen et al., Phys. Rev. Lett. 72(1994)608. M. Ambrosio et al., Astrop. Phys. 6(1997)113; Nucl. Instr. Meth. A486(2002)663; Astrop. Phys. 4(1995)33; Astrop. Phys. 18(2002)27.

[37] M. Ambrosio et al., Eur. Phys. J. C25(2002)511; Phys. Lett. B406(1997)249; Phys. Rev. Lett. 72(1994)608; Astropart. Phys. 18(2002)27.

[38] H. Huguet and P. Peter, hep-ph/9901370 (1999).

[39] G. Giacomelli and L. Patrizii, Magnetic Monopole Searches, hep-ex/0302011v2 (2003).

[40] The Slim collab., Search for "Light" Magnetic Monopoles, hep-ex/003028v1 (2000).

[41] J. Lindhard and M. Scharff, Energy dissipation of ions in the KeV region, Phys. Rev. 124 (1961)28.

[42] S.P. Ahlen and K. Kinoshita, Calculation of the stopping-power of very low velocity magnetic monopoles, Phys. Rev. 26D (1982)2347.

[43] G. Giacomelli and L. Patrizii, Magnetic Monopoles, hep-ex/0002032v1 (2000).

[44] A. De Rujula and S. Glashow, Nature 31(1984)272.

[45] V. Popa, Penetrability of Nuclearites in the atmosphere and their detectability, Internal Note, SLIM April/2004.

[46] Edward Farhi and L. Jaffe, Strange Matter, Phys. Rev D30, (1984)2379.

[47] E. Witten, Phys. Rev. D30(1984)272.

[48] M.Yu.Khlopov et al., astro-ph/0603187.

[49] M. Kasuya et al., Phys. Rev. D47 (1993)2153; A. Olinto, The physics of strange matter, Proceedings of Relativistic Aspects of Nuclear Physics, Rio de Janeiro, Brazil (1991)187.

[50] S. Balestra et al., Search for nuclearites with the SLIM detector, hep-ex/0601019v1 (2006).

[51] H. Heiselberg, Phys. Rev. D 48 (1993)1418.

[52] J. Madsen, Phys. Rev. Lett. 87 (2001)17203.

[53] M. Kasuya, T. Saito and M. Yasue, Phys. Rev. D 47 (1993)2153.

[54] V. Choutko (AMS collab.) 28th ICRC (2003)OGI, 1765.
T. Saito et al., Phys. Rev. Lett. 65 (1990)2094.
M. Ichimura et al., Il Nuovo Cimento A106 (1993)843.
P.B. Price et al., Phys. Rev. D18 (1978)1382.

[55] J.F. Ziegler et al., The Stopping and Range of Ions un Solids, Pergamon Press, New York, 1985 (edit.2003).

[56] G. Wilk and Z. Wlodarcyzk, Heavy Ion Phys. 4 (1996)395.
M. Rybczyńsky et al., Strangelets at Chacaltaya, hep-ex/0009164v1 (2002).

[57] S. Banerjee et al., Phys. Rev. Lett. 85 (2000)1384.

[58] Z. Sahnoun, Nuclearites and Strangelets in SLIM, private comunication (2006); Internal Note SLIM 2006/1.

[59] S. Coleman, Nucl. Phys. B262(1985)293. A. Kusenko and A. Shaposhnikov, Phys. Lett. B418(1998)46.

[60] A. Kusenko, Phys. Lett. B 405, 108 (1997).

[61] T.A. Ioannidou et al., Energy-Charge Dependence for Q-balls, hep-th/0302013v1 (2003).

[62] A. Kusenko and M. Shaposhnikov, Phys. Lett. B417 (1998)99. A. Kusenko et al., Phys. Rev. Lett. 80 (1998)3185.

[63] D. Bakari, et al., Energy Losses of Q-balls, hep-ex/0003003v1 (2000).

[64] E. N. Parker, Astrophys. J. 160 (1970)383.

[65] M.S. Turner, E.N. Parker, and T.J. Bogdan, Phys. Rev. D26 (1982)1296.

[66] F. Adams et al., Phys. Rev. Lett. 70 (1993)2511.

[67] S. Balestra et al., Magnetic Monopole Search at high altitude with the SLIM experiment, arXiv:0801.4913v1 [hep-ex] (2008).

[68] Solid State Nuclear Track Detection, S.A. Durrani, R.K. Bull, International Series in Natural Philosophy, Volume 111. Pergamon Press. 1987.

[69] S. Cecchini et al., Calibration of the Intercast CR39, Nucl. Tracks Radiat. Meas. 22 (1993)555.

[70] Tommaso Chiarusi, Measurements of the primary cosmic ray composition with the CAKE experiment, Ph.D thesis, Universitá di Bologna (2003).

[71] Energy loss in matter by heavy particles, Don Groom, PDG-93-06, 1993.

[72] Techniques for Nuclear and Particle Physics Experiments, William R. Leo, © Springer-Verlag Berlin Heidelberg 1987.

[73] R.M. Sternheimer, M.J. Berger, S.M. Seltzer, Data and Nucl. Data Tables 30, 262(1984).

[74] SAMAICA V2.2.X, Reference Manual, ELBEK-Bildanalyse GmbH.

[75] Neutron spectrometry at high mountain observatories, A. Zanini et al., Journal of Atmosph. and Solar-Terrestrial Physics 67 (2005) 755-762.

[76] The Slim collab., Search for "Light" Magnetic Monopoles, hep-ex/0003028v1 (2000).

[77] T. Shibata, Prog. Theor. Phys. 57 (1977)882.

[78] Geant4 Reference Manual, Users Guides Documentation, http://geant4.web.cern.ch

[79] Nuclear Instruments and Methods in Physics Research A 506(2003)250-333. IEE Transactions on Nuclear Science 53 N.1(2006)270-278.

[80] Tommaso Chiarusi et al., Simulation of acoustic waves produced by a proton beam into a water basin, NEMO internal note.

[81] Cosmic ray studies on the ISS using SSNTD, BRADOS projects, 2001-2003, J.K. Pálfalvi et al., Radiation Measurements 40 (2005) 428-432.

[82] Track formation in CR-39 detector exposed to D-T neutrons, K. Oda, et al., Nuclear Instr. and Meth. in Physics Research B35 (1988) 50-56.

[83] Neutron-induced complex reaction analysis with 3D nuclear track simulation, L.Sajó-Bohus et al., Rad. Measurements 40 (2005)442-447.

[84] . F. Ziegler, et al., "The Stopping and Range of Ions in Solids". Pergamon Press, New York, 1985 (new edition in 2003).

[85] D.F. Smart and M.A. Shea, Proc. 25th ICRC (Durban, 1997) Conf. Papers 2, 401.

[86] G. Giacomelli et al., New results from the exposures of the CR39 track detector. Radiat. Meas. 28, 217-220 (1997)
G. Giacomelli et al., Extended calibrations of CR39 nuclear track detector with 158 AGeV Pb 207 ions. Nucl. Instrum. Meth. A 411, 41-46 (1998).

[87] Neural Networks, Christos Stergiou and Dimitros Siganos
http://www.doc.ic.ac.uk/ nd/surprise_96/journal/vol4/cs11/report.html.

[88] Neural Networks and Qualitative Physics, Jean-Pierre Aubin, Cambridge Univ. Press 1996.

[89] TMultiLayerPerceptron, http://root.cern.ch

[90] Introduction to Pattern Analyse, Ricardo Gutierrez Osuna, Wright State University. http://courses.cs.tamu.edu/rgutier/ceg499_s02/l1.pdf..

[91] Convergence property of the Fletcher-Reeves conjugate method with errors, C. Y. Wang and M. X. Li. Journal of industrial and management optimation, vol 2, May 2005.

[92] J.T. Link et al., Measurements of the Ultra-Heavy Galactic Cosmic-Ray Abundances between Z=30 and Z=40 with the TIGER Instrument, Universal Academy Press, Inc. pp.1-4 (2003). The 28th International Cosmic Ray Conference.

[93] Wiebel-Sooth, B. Biermann, P.L. Meyer, H. A& A 330, 339-389-398, 1998; astro-ph/9509253.

[94] D.P. Bhattacharya et al., Estimation of Elemental Abundances of Heavy Cosmic-Ray Primaries at the Top of the Atmosphere Using Plastic Emulsion Chamber and the Derived Source Spectrum from the Steady-State Leaky Box Model, Il Nuove Cimento, Vol. 18, N.2 (1995)161-175.

[95] P.K.F. Grieder, Cosmic Rays at Earth: Researche's Reference Manual and Data Book (Elsevier, New York) (2001).

Appendix A

SLIM MC, Physics List

Physical processes activated in the simulation of the interaction of neutrons with CR39. Individual channels are indicated for each one of the process.

Electromagnetic processes:
G4MultipleScattering(), G4GammaConversion(),
G4ComptonScattering(), G4PhotoElectricEffect(),
G4eIonisation(), G4eBremsstrahlung(),
G4eplusAnnihilation(), G4MuBremsstrahlung(),
G4MuPairProduction(), G4MuIonisation(),
G4hIonisation()

Hadron **P**hysics:
G4NeutronInelasticProcess(), G4LENeutronInelastic,
G4HENeutronInelastic(), G4NeutronHPInelastic,(0 - 20 MeV)
G4HadronElastic(), G4UHadronElasticProcess();
G4NeutronHPElastic()

Ion **P**hysics:(ICRU)
G4LEDeuteronInelastic(), G4DeuteronInelasticProcess(),
G4LETritonInelastic(), G4TritonInelasticProcess(),
G4LEAlphaInelastic(), G4AlphaInelasticProcess()

Capture:
G4HadronCaptureProcess(), G4LCapture(),
G4NeutronHPCapture(), G4NeutronCaptureAtRest()

Decay:(Ivanchenko)
G4Decay()

Low energy physics:
G4HadronFissionProcess(), G4LFission()
G4NeutronHPFission() (0 - 20 MeV), G4NeutronHPorLFission()

Appendix B

Cross Sections

The figure show the total cross sections (σ) of n with H, C and O as a function of the energy. The data is taken from the *Evaluated Nuclear Data Files*, electronic libraries from the Korea Atomic Energy Research Institute 2000; the data plotted is from the electronic library ENDF-VI [1]. The plot show σ in the range 0.05 to 60 barn *vs.* the neutrons energy in the range 0.1 to 20 MeV, H cross sections are plotted with a red line (data from the library 1-H-1 LANL Eval. Oct.89, Hale, Dodder, Siciliano, Wilson); for C the σ is plotted with a green line (library: 6-C-0 ORNL Eval. Aug.89, C.Y. Fu, E.J. Axton and F.G. Perey); total cross sections for O are plotted with a blue line (8-O-16 LANL Eval. Jan.90, G. Hale, Z. Chen, P. Young). The figure shows that the mean total σ of H with neutrons at low energies (~ 0.1 - 1 MeV), is higher than the σ of C and O (not considering the fine structure showing bumps); at energies in the range $\sim$ 2 - 10 MeV the σ values of H, C and O are overlapped; and for energies greater than $\sim$ 10 MeV the σ of C and O are higher than H ones.

[1] ENDF-VI summary documentation http://atom.kaeri.re.kr/cgi-bin/endfplot.pl

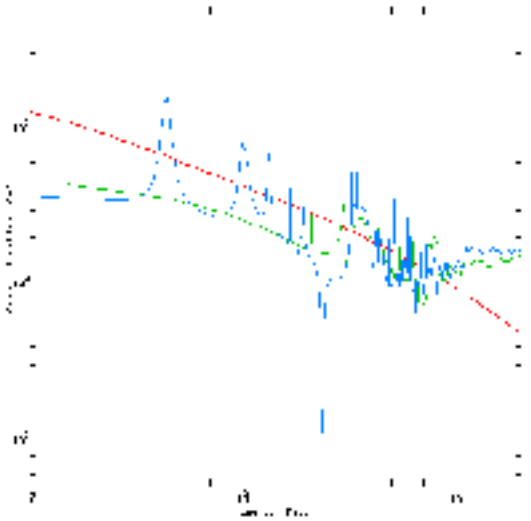

Figure B.1: Total cross sections of n-H (red line), n-O (blue line), and n-C (green line) in the energy range 0.05 - 60 MeV. Data form the ENDF-VI libraries of "Evaluated Nuclear Data Files" from the Korea Atomic Energy Research Institute 2000.